**ACDIV-2017-02**
February 2017

# LONGITUDINAL AND TRANSVERSE BEAM DIAGNOSTICS USING SYNCHROTRON RADIATION AT ALBA

L. Torino

## Abstract

Synchrotron Light Sources are usually user-oriented facilities, for this reason it is necessary to ensure a high reliability of the machine, for which a constant and on-line monitoring of the particle beam is mandatory. The synchrotron radiation produced by the beam can be used to develop non-invasive diagnostics tools to perform measurements of both longitudinal and transverse electrons distribution. In this talk, techniques used and developed at ALBA Synchrotron Light Source in the last years and their applications will be presented. The setup of Time Correlated Single Photon Counting for filling pattern measurements, using both visible light and x-rays, together with its applications in the development of new machines operation modes will be presented.

Moreover the commissioning of the Synchrotron Radiation Interferometry (SRI) and its basic application to measure the horizontal and vertical dimension of the beam will be introduced, together with further developments aided to improve the standard SRI resolution and to open new possibilities such as measurements at low current or bunch by bunch.

Accelerator Division
Alba Synchrotron Light Source
c/ de la Llum, 2-26
08290 Cerdanyola del Valles, Spain

LAURA TORINO

# LONGITUDINAL AND TRANSVERSE BEAM DIAGNOSTICS USING SYNCHROTRON RADIATION AT ALBA

# LONGITUDINAL AND TRANSVERSE BEAM DIAGNOSTICS USING SYNCHROTRON RADIATION AT ALBA

RELATORI:

Prof. Franco Cervelli
Dr. Ubaldo Iriso Áriz

CANDIDATO:

Laura Torino

Tesi di Dottorato

Dipartimento di Fisica
Facoltà di Scienze Matematiche Fisiche e Naturali
Università di Pisa

WHAT do you see now?
...
Try this.
Just a goblet on a table.
Oh I see! Try this lens!
Just an open space — I see nothing in particular.
Well, now!
Pine trees, a lake, a summer sky.
That's better. And now?
A book.
Read a page for me.
I can't. My eyes are carried beyond the page.
Try this lens.
Depths of air.
Excellent! And now?
Light, just light, making everything below it a toy world.
Very well, we'll make the glasses accordingly.

*– EDGAR LEE MASTER, Dippold the Optician, The Spoon River Anthology*

# ACKNOWLEDGMENTS

I always like to remember that accelerators are huge, complex machines. This is mainly to specify that the work I have done at ALBA would not have been possible without the support and the help of all the ALBA staff. Starting from the mechanical workshop people, without whom the accelerator and the beamlines would not even be there, passing through the engineering and the computing divisions which design the components and control all the equipments, up to the experimental division without whom the machine would not have a real scope, and the administration assistants, who handle all the bureaucracy and make the work easier.

In my case, the accelerator division deserves special mention: without the linac group, we would not have any electrons to accelerate, and without the insertion device, the RF, and the beam dynamic groups, who knows where these electrons would be! Well, probably the beam diagnostic people could tell... Finally, I cannot forget the operators, i.e. the ones that can really *drive* the machine and solve (almost) all the problems.

Not to be forgotten is also the accelerator community, and in particular the one devoted to the synchrotron light sources diagnostics. The exchange of ideas and the support we lend one another has really made me feel part of a selected family. I also want to thank oPAC people, for making me appreciate and exploit the importance and the necessity of networking in the field.

Going back to ALBA —now being more particular—, first of all I want to thank Dr. U. Iriso, for guiding me, when needed, but mainly for trusting me and giving me the freedom to develop my own projects as part of the staff, from the very beginning.

I also want to thank the accelerator division in general, and F. Pérez and M. Pont in particular, for their patience and for always finding a spot to perform my experiments whenever it was possible... I am sure nobody will ever forget my Parasitic PSAs!

As is evident in the thesis, my work has been very transversal, and for this reason I have had to deal with all the ALBA divisions. From the experiment division a special thanks goes to J. Nicolás for his indispensable advice about optics and optical components. I also want to thank P. Pedreira and I. Šics from the metrology group for the support with the vibration measurements. Many thanks also to J. Juanhuix and the beamline staff of XALOC for letting me some beam time.

From the computing division I owe a lot to S. Blanch, for his invaluable work with the PicoHarp device server and for always being ready to solve my software problems. I also want to thank M. RodrÃguez for the help with the cluster for the SRW simulations.

From the electronic group, special thanks to O. Matilla for the inspiring discussions, and to A. Camps and B. Molas for solving my electronic trouble.

From the engineering division, many thanks to M. Llonch and J. Ladrera from the alignment group for the help with the Xanadu upgrade and the vibration measure-

ments, and to G. Peña for the photon counting mechanical setup.
I also want to thank my office mates for sharing with me the joy and the pains, especially in this last period. In particular I really owe a lot to M. Carlà for the stimulating discussions about (but not only) science.

Finally, outside ALBA, I think that my way into the world of particle acceleration would not have been started without my other supervisor, F. Cervelli, who first introduced me to the field and has accompanied me until now. I really owe him a lot.

Y llega el momento de hablar español; otra cosa que he aprendido en el doctorado (más o meno). Quiero dar las gracias a todas las personas que me han acompañado en este camino, empezando por la gente que he conocido a ALBA. Gracias a los de ALBAR's, por los *afterwork* y las tardes pasadas en la fantástica Cerdanyola del Vallés y en otros lugares. Gracias a los Pescadillas por el café de despues de comer y las conversaciones que iban siempre más allá (de qué, no se sabe). Gracias a las Cerdis por las bodas, los viajes y las risas.

Y fuera del trabajo, tengo que darle las gracias a mi compañero de piso, porque "Lo mejor de mi piso es con quien lo comparto". Gracias a V&C, catalanes y italianos porque sin vosotros no me habría sentido como en casa. Y gracias a las Ola k Ase, aunque la tradición de los jueves por la tarde siga sin estar bien establecida. Gracias a vosotros puedo decir que he aprovechado al máximo esta heromosa ciudad que es Barcelona. Mejor dicho: *merci a tothom*.

Finalmente passo alla mia lingua, che invece un po' ho dimenticato. È il momento di ringraziare i fisici (e non), pisani (e non), sparsi per il mondo (e non), in particolare quelli dei capodanni in giro per l'Europa (e non). È bello sapere che anche a distanza, dopo tanto tempo, c'è sempre qualcuno su cui contare e che sa come farti sorridere.

Ultima ma senza dubbio prima in importanza, voglio ringraziare la mia famiglia. Loro hanno fatto di me quello che sono, pur sempre lasciandomi libera di fare le mie scelte. Loro mi hanno insegnato che la via giusta é quella che va *in direzione ostinata e contraria.*

# CONTENTS

# INTRODUCTION

> Quis custodiet ipsos custodes?
>
> Juvenal

ALBA is a third generation Synchrotron Light Source (SLS) located in Barcelona (Spain), which was commissioned in 2011 [1]. SLS are high energy electron accelerators whose design is optimized to provide brilliant X-ray fluxes for a scientific (and industrial) user community.

Being a user-oriented facility, it is important to ensure a high reliability of the machine, for which a constant and on-line monitoring of the particle beam is mandatory. This task is carried out using the "Beam Diagnostics" components, which continuously characterize the particle beam. These diagnostics systems shall be precise, reliable and non-invasive in order to avoid any interference with the machine operation. Whenever possible, redundant diagnostics components are desirable to provide beam availabilities close to 100%.

The objective of this PhD thesis the development of improved and alternative longitudinal and transverse beam diagnostics systems using synchrotron light.

In the longitudinal plane, Filling Pattern (FP) measurements show how the beam charge is distributed along the machine RF-buckets. In 2012, the only FP measurements system at ALBA used the analysis of the beam electromagnetic signal produced by a Fast Current Transformer, whose dynamic range is less than $10^2$ [2]. One of the objectives of this thesis is to develop an alternative FP measurement system to improve the dynamic range for future applications.

To this aim, the adopted technique is the Time Correlated Single Photon Counting (TCSPC) [3], which is explained in Chapter 2. TCSPC can be done using the visible part of the synchrotron radiation spectrum (Chapter 2), or the X-ray part (Chapter 3), for which different photon detectors are used. The thesis shows the characterization of these detectors and the design of their optimized experimental stations. Their performances are compared in Chapter 4, which also shows the integration of final FP measurements in the machine control system and how this integration allows, for instance, the implementation of the Single Bunch Bucket Selection operation mode to inject a given amount of current in a specific RF-bucket.

During the ALBA commissioning in 2011, the transverse beam size was measured using an X-ray pinhole [4]. In order to provide ALBA with an alternative transverse beam size monitor, it was decided to use the already existing diagnostics beamline "Xanadu" to perform beam size measurements through the Synchrotron Radiation

Interferometry (SRI) [5]. This technique consists on a Young-like interferometry that measures the light spatial degree of coherence, from which the beam size is finally inferred.

The SRI theory is presented in Chapter 5, which also shows the required beamline upgrade to fulfill the stringent conditions of the optical instrumentation. Feasibility studies are presented in Chapter 6 using the simulation code "Synchrotron Radiation Workshop" [6], together with experimental beam size measurements.

However, SRI only provides a projected beam size. Chapter 7 shows a novel method to obtain the full transverse beam profile using a rotating mask, which allows to infer the geometrical beam ellipse semi-axes and tilt using SRI, for the first time in accelerators. The same method can also be applied to improve the standard SRI resolution and measure ultra-low beam sizes. Furthermore, the thesis presents how to use a mathematical matching algorithm to overcome the limitations arisen from low Signal-to-Noise ratio SRI images. Finally, first bunch-by-bunch size measurements in SLS using a Fast Gated Camera are shown: these offer a new tool to diagnose the internal dynamics of different beam instabilities.

# 1

# ALBA SYNCHROTRON LIGHT SOURCE

## 1.1 SYCHROTNRON LIGHT SOURCES

Nowadays many fields of science such as material science, chemistry, and biology do not settle anymore for common microscope to study the behavior of the nature.

More and more intense photon flux is needed to study processes that cannot be observed otherwise. Some specific studies such as chirality or magnetic property of materials can only be performed using polarized radiation. Others need specific time distribution of the photon intensity to perform pump and probe experiments.

These requests contributed to the development of facilities devoted to the production of a specific kind of radiation: the Synchrotron Light Sources (SLS), which are electron accelerators specifically developed to produce synchrotron radiation [7, 8].

Synchrotron radiation is named after its discovery at a synchrotron of the General Electric in 1947. With this name one refers to the radiation produced by a relativistic charged particle when accelerated transversally. The production of radiation provokes a loss in the particle beam energy. For this reason synchrotron radiation was seen initially as an annoying effect produced in the bending magnets of the high energy electron machines.

Later synchrotron radiation started to be used parasitically in accelerators devoted to particle physics, to perform material science experiments. These accelerators are referred to as the *first generation* of SLS.

Due to a strong increase on the demand, a *second generation* of light sources arose. Specific accelerators were designed to be fully dedicated to these purposes, with an optimized lattice to improve the radiation quality. The first storage ring of this kind was the 240 MeV Tantalus I, USA [9].

The *third generation* of light sources is the one in operation nowadays. These machines are characterized by very small emittance in order to increase the brilliance of the photon beam. Moreover the lattice design is studied to be compact such to leave space for several straight sections in which the insertion devices would sit.

Insertion devices are divided into *undulators* and *wigglers*, two specific magnetic structures studied to produce more intense and coherent flux of synchrotron radiation with higher energies or more monochromatic flux [10]. The produced synchrotron radiation is extracted, focused and guided to the experimental station called *beamlines*, through the so called *front-end*. Each beamline has specific requirements in terms of energy and flux, both depending on the lattice and the insertion devices.

The machine design also allows to operate in *Top-Up* mode so to refill the beam and maintain a constant current (and, consequently, a stable flux of photons).

A so called *third-plus generation* of light sources are currently being built and will be soon operational. These machines use a Multi-Bend Achromat lattice in order to reduce further the emittance, paying the price of lattice flexibility. An example of these machines is MAX IV in Sweden [11].

Finally the *fourth generation* of light sources are the Free Electron Lasers (FEL). These machines are linear accelerators equipped with undulators. While SLS can be equipped with tens of beamlines working in parallel, FELs can generate light for one or two beamlines working at the same time. The great advantage of FELs is their capability to provide extremely short, coherent, and intense photon pulses, very valuable for temporal resolved experiments.

Today more than 40 SLS are operating around the world producing synchrotron radiation either for scientific experiments of for industrial applications.

In SLS, beam particles are required to maintain a constant energy and specific longitudinal and transverse characteristics to provide photon beams for experiments.

## 1.2 ALBA SYNCHROTRON LIGHT SOURCE

ALBA [1, 12] is a 3 GeV electron machine, located in Cerdanyola del Vallés, near Barcelona, Spain, and is operative since 2011. Nowadays 8 beamlines are open to external users, one is under construction and 6 other have been approved.

ALBA is designed to have small emittance (4.6 nm rad), a 500 MHz pulsed electron beam, and maximum stored current of 250 mA, in order to produce bright beam of synchrotron radiation. During standard operation the machine is now operating in Top-Up mode with the stored current of 130 mA.

An overview on Beam Dynamics and Synchrotron Radiation theory is summarized in Appendix A.

The ALBA facility comprehends an Injection System, composed by a Linac and a full-energy Booster, a Storage Ring, and the Beamlines that receive light from bending magnets or dedicated Insertion Devices. The main characteristics of the accelerator are reported in Tab. 1.1, and a technical drawing of the facility is shown in Fig. 1.1.

The linac is the pre-injector operating both in single and in multi-bunch mode, providing a maximum charge of 4 nC. Operating in multi-bunch mode the maximum length of the delivered bunch train is 1000 ns, while for the single-bunch mode only 1 ns long pulses with 0.25 nC charge is delivered. In both cases the highest energy achievable is 125 MeV. ALBA Linac is routinely operational at 110 MeV in multi-bunch mode, and the nominal frequency rate of the injector is 3.125 Hz [1].

The Booster is the last part of ALBA injector [14]: its function is to increase particle energy from the injection value (110 MeV), up to the extraction one (3 GeV), when bunches are injected in the Storage Ring. The main peculiarity of the ALBA Booster is the low emittance (10 nm rad) which allows to reach a high transmission efficiency from the booster to the storage ring.

Finally, the ALBA Storage Ring is optimized to produce synchrotron radiation with a critical energy around 8.5 keV [15, 16]. The Storage Ring has a 4-fold symmetry with

| ***Linac*** | | |
|---|---|---|
| Extraction energy, $E_{El}$ | 110 | MeV |
| Emittance ($x$ and $y$), $\varepsilon_l$ | 150 | nm rad |
| Energy spread (rms), $\frac{\Delta E_l}{E_l}$ | 0.20% | |

| ***Booster*** | | |
|---|---|---|
| Circumference,$C_b$ | 249.6 | m |
| Injection energy, $E_{Ib}$ | 110 | MeV |
| Extraction energy, $E_{Eb}$ | 3.0 | GeV |
| Emittance at 3 GeV ($x$ and $y$), $\varepsilon_b$ | 9 | nm rad |
| Energy spread at 3 GeV (rms), $\frac{\Delta E_b}{E_b}$ | 0.10% | |
| Betatron tune, $Q_x$ | 12.42 | |
| Betatron tune, $Q_y$ | 7.38 | |
| Maximum horizontal $\beta$-function, $\beta_{bx}$ | 11.2 | m |
| Maximum vertical $\beta$-function, $\beta_{by}$ | 11.7 | m |
| Maximum dispersion, $D_{bx}$ | 0.47 | m |
| RF frequency, $\omega_{RF}$ | 500 | MHz |
| Repetition rate | 3.125 | Hz |

| ***Storage Ring*** | | |
|---|---|---|
| Circumference, $C_{SR}$ | 268.8 | m |
| Maximum current, $I$ | 250 | mA |
| Energy, $E$ | 3 | GeV |
| Emittance ($x$ and $y$), $\varepsilon$ | 4.6 | nm rad |
| Energy spread, $\frac{\Delta E}{E}$ | 0.105% | |
| Betatron tune, $Q_x$ | 18.15 | |
| Betatron tune, $Q_y$ | 8.37 | |
| Maximum horizontal $\beta$-function, $\beta_x$ | 17.89 | m |
| Maximum vertical $\beta$-function, $\beta_y$ | 24.93 | m |
| Maximum dispersion, $D_x$ | 0.247 | m |
| Minimum Bunch Length | 16 | ps |

Table 1.1: Main characteristics of the ALBA accelerator facility [1, 13].

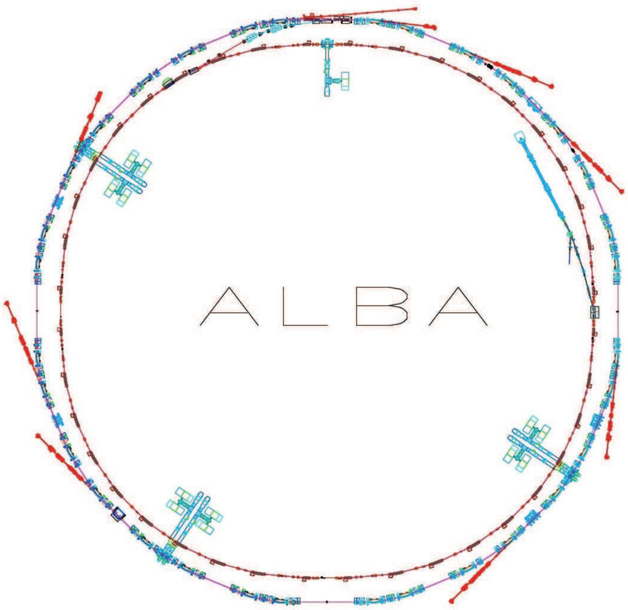

Figure 1.1: ALBA accelerator machine: The Linac is in the interior of the machine. The Booster is the inner ring; its accelerating cavity is located on the top of the drawing. Just before the booster cavity the Booster-To-Storage Ring transfer line is present connecting the interior and the exterior ring. The Storage Ring is the exterior ring with six RF cavities distributed among three short straight sections. In the drawing beamlines are represented as tangential straight.

24 straight sections: 4 long (8 m), 12 medium (4.2 m) and 8 short (2.6 m). In principle, all straight sections are designed to locate an Insertion Device. Nevertheless, some of them have to be used to operate the machine: three short sections are used to locate RF cavities, two for diagnostics, and one long straight section is used to accommodate the Booster-to-Storage injection system composed by four kickers and a septum.

The RF system [17] consists of six normal conducting RF cavities and can provide up to 3.6 MV of accelerating voltage to provide up to 540 kW power to the electron beam.

As in other SLS, the main requirements for the ALBA lattice are:

- compactness, in order to have large number of straight sections of different length to accommodate the Insertion Devices,
- low emittance, both horizontal and vertical ($\varepsilon_x$, $\varepsilon_y$), to obtain a high photon beam brilliance ($\mathcal{B} \propto \frac{1}{\varepsilon_x \varepsilon_y}$).

To accomplish these requirements the lattice chosen for the ALBA storage ring is a “detuned” Double Band Achromatic (DBA) [18]. It consists of a sequence of focusing and defocusing elements (quadrupoles and sextupoles), and a combined-function bending magnet, arranged as shown in Fig. 1.2.

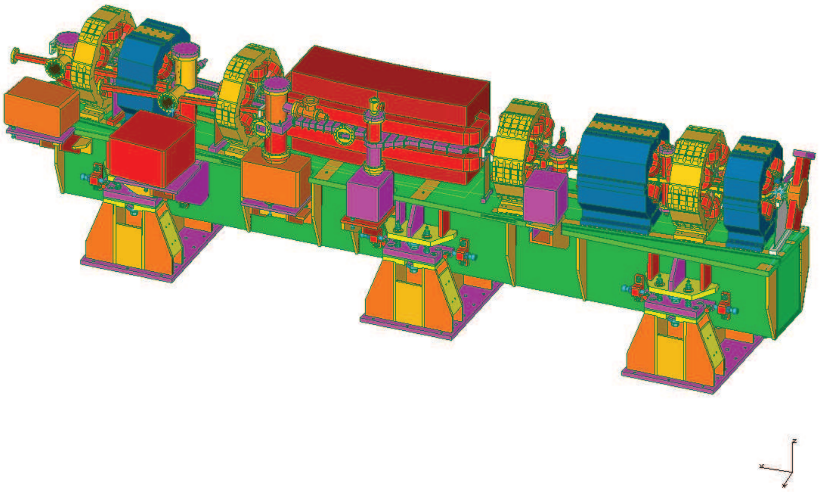

Figure 1.2: Technical drawing of the girder containing the unit cell. The bending magnet is in red, quadrupoles are in blue and sextupoles in yellow.

The Twiss parameters of one of the ALBA quadrant are shown in Fig. 1.3. The label "M" marks the medium straight sections, designed with low $(\beta_x, \beta_y)$ to accomodate the insertion devices.

## 1.3 BEAM DIAGNOSTICS AT ALBA

On-line beam monitoring is the key point to provide reliable machine operation [19]. The particle beam is characterized by measuring its current, its transverse and longitudinal distributions, and its transverse position inside the vacuum chamber along the machine. The beam diagnostics components of the ALBA storage ring are listed in Table 1.2 [20, 21].

| | |
|---|---|
| Transverse Position | 123 BPMs |
| Beam Losses | 128 BLMs |
| Beam Current | 1 DCCT |
| Longitudinal Beam | 1 FCT<br>1 Streak Camera |
| Transverse Beam | 7 FSs<br>1 X-rays pinhole |

Table 1.2: Collection of the diagnostic equipment of the ALBA storage ring.

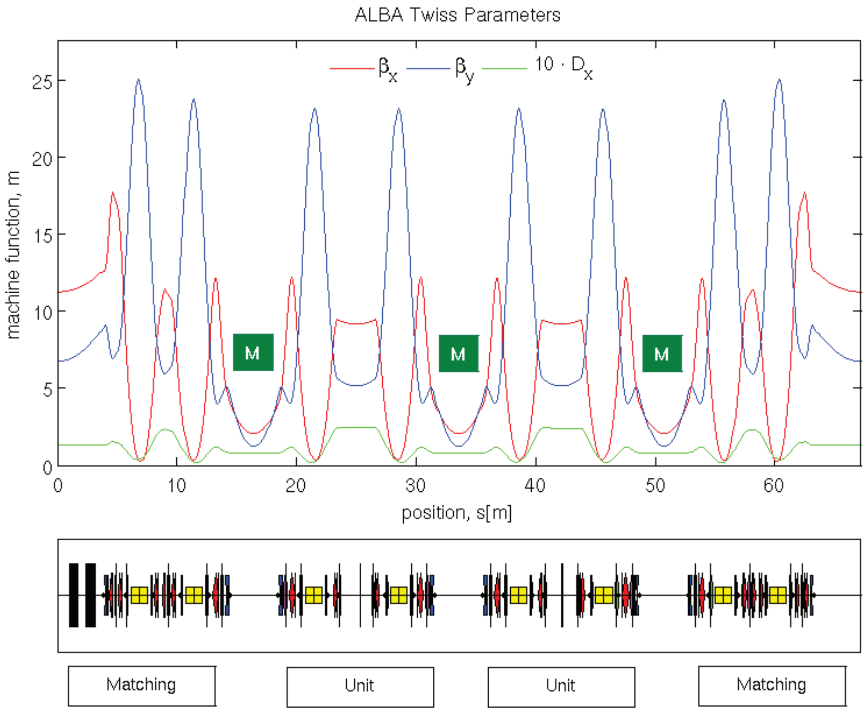

Figure 1.3: Detuned DBA lattice of one quadrant of the ALBA Storage Ring, showing the magnet arrangements (bottom plot), the β functions and the dispersion in two unit cells and two matching cells.

123 Beam Position Monitors (BPMs) are used for orbit control and interlock system [22]. Their output is used as an input for the orbit feedback, which keeps the electron beam orbit within 0.3 µm range [23, 24]. BPMs also trigger the Transverse Multi Bunch System used to reduce the beam instability effects [25].

128 Beam Loss Monitors (BLMs) monitor the beam losses around the storage ring [26] in real time. They provide information about unwanted excitations, bad behavior of the magnets, and possible misalignments of vacuum chamber sections.

The beam current is continuously monitored by a DC-Current Transformer (DCCT), while the filling pattern is controlled on-line by a Fast Current Transformer (FCT) [2]. The bunch length can be measured by a Streak Camera located in Xanadu [27], which is the ALBA visible light diagnostics beamline.

The transverse shape can be qualitatively monitored in a destructive way using Fluorescence Screens (FSs). 7 of them are installed around the ALBA storage ring and were quite useful during the commissioning [21]. Nowadays the beam size is constantly monitored with an X-ray pinhole [28].

## 1.4 OBJECTIVE OF FILLING PATTERN MEASUREMENTS

The Filling Pattern (FP) is the bunch distribution scheme along the machine (see Appendix A.2). Different accelerators provide different FP according to machine stability requirements and to the experimental needs. The FP is constantly monitored to evaluate the performance of the injection system and check possible beam instabilities.

Some SLS use the so called "Hybrid" FP. This special scheme consists of a single train occupying about 2/3 of the machine plus a filled single RF-bucket placed far from the train. This FP is used for "time resolved" beamline experiments. The single bunch is used to excite the sample and the radiation coming from the trains is used to perform the measurements (pump and probe). Other machines prefer Full FP where all the RF-buckets are filled.

A sketch of the Hybrid and Full FP are presented in Fig. 1.4, together with the FP used at ALBA during standard operations. The amount of current distributed among the bunches corresponds to the total stored current of 100 mA.

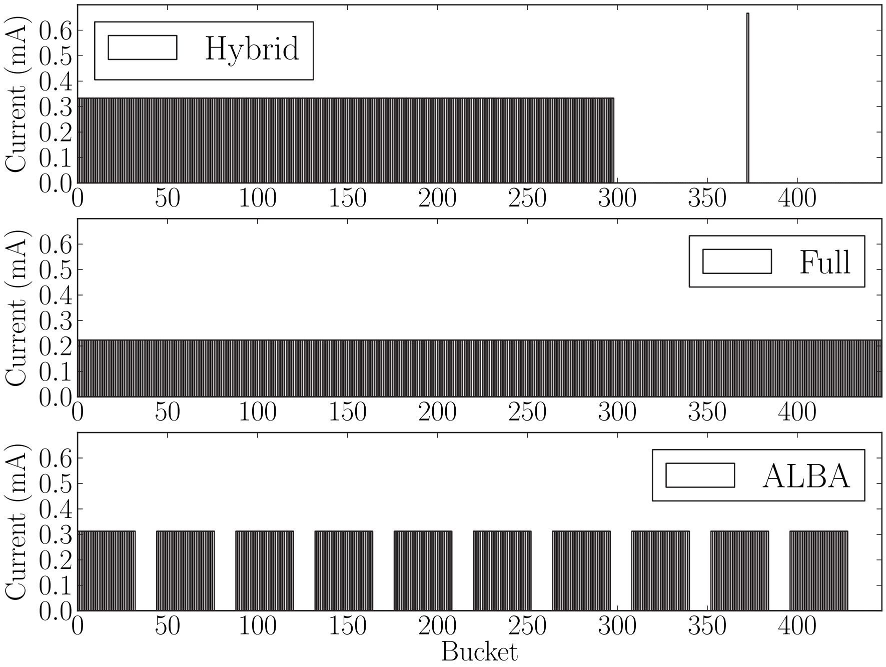

Figure 1.4: Different FP scenarios available at ALBA when filled with 100 mA. Hybrid FP at the top, Full FP at the center, and standard ALBA FP at the bottom, called "10-Trains".

One of the objective of the FP measurements is to provide the input for selective Top-Up injections. During standard Top-Up mode, the bunches are refilled regularly to keep a constant beam current in the machine. This is very important for beamlines operations since it keeps constant the X-rays flux, and, as a consequence, the heat load on the beamline optical components, avoiding drifts in energy and focal position. As an upgrade of this operation mode, the selective Top-Up foresees the selective refilling of emptier bunches in order to equalize the bunch currents and improve the machine stability.

When operating in Hybrid mode, FP measurements must also control the *Bunch Purity*, which is the ratio between the number of particles in the isolated single bunch (i. e. at RF-bucket 370 in the upper plot of Fig. 1.4), and the number of particles in the neighboring RF-buckets (i.e. RF-buckets 369 and 371 in the upper plot of Fig. 1.4). For time resolved experiments the electrons located in undesired RF-buckets might spoil the measurements. Usually, the signal to noise ratio required by these experiments is better than $10^5$, so the diagnostic setup must have the dynamic ranges around $10^6$.

### 1.4.1 *Filling Pattern Measurements at ALBA*

The usual FP at ALBA (bottom plot of Fig. 1.4) is composed by 10 trains of 32 bunches each, distributed among the 448 available RF-buckets, $\simeq 2\,\mathrm{ns}$ long each. Between two consecutive trains a gap of 12 empty RF-buckets is present. In order to break the symmetry and to allow the identification of the so called "RF-bucket 0", the last gap is composed by 24 empty RF-buckets. This configuration was chosen to fulfill machine stability requirements: the gaps among the trains reduce the instability effects related with the so-called ion-cloud effect.

With the development of new experimental stations the demand for FP can change (for example for time resolved experiments). In recent years, a Single Bunch Bucket Selection (SBBS) injection has been developed. This technique allows to inject a well-defined amount of current in a given position of the beam to shape the FP as desired. The same injection method can also be used to perform the selective Top-Up.

Before these developments, the FP was monitored using a Fast Current Transformer (FCT) together with an on-line data treatment [29, 2]. Figure 1.5 presents the raw data from the FCT directly connected to the scope (top), and the result after the data treatment (bottom). The FCT and the related on-line data analysis provides a dynamic range around $10^2$ which is not enough for bunch purity measurements, although it can be used for selective Top-Up operation. Moreover, the data analysis does not get rid of a significant amount of "spurious" bunches in the gaps, produced by the FCT electronics noise.

To guarantee the continuous operation of the machine in selective Top-Up mode, ALBA was looking for an alternative FP measurements to ensure redundancy. Moreover a system with better performance to measure the bunch purity with the required dynamic range was needed: for these purposes the Time Correlated Single Photon Counting was developed at ALBA, as described in Chapters 2 and 3.

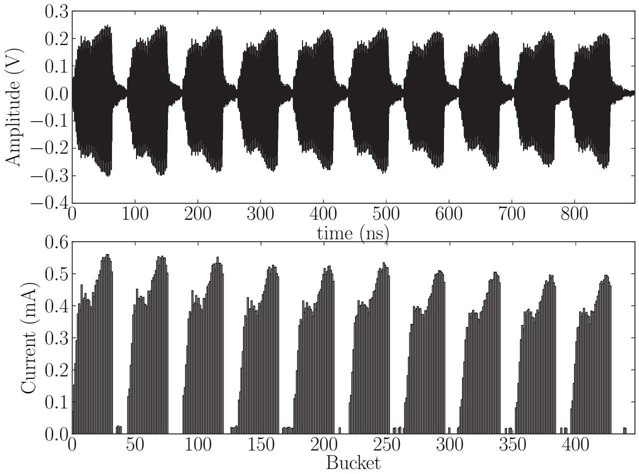

Figure 1.5: 10 Trains FP measured by the FCT during routine operation. Note the presence of "spurious" bunches between the trains.

## 1.5 OBJECTIVE FOR BEAM SIZE MEASUREMENTS

Measurement and control of the particle beam emittance is the key ingredient to characterize the performance of any accelerator. Since the emittance itself is not a direct measurable parameter, most accelerators monitor its surrogate: the transverse beam size. The particle beam emittance is then inferred from the knowledge of the machine optical parameters [30], provided by computer codes, such as the Linear Optics from Closed Orbits (LOCO) code [31, 32].

SLS have developed a variety of techniques to measure the transverse beam size based on synchrotron radiation [33], due to its non-destructive nature.

As usual for third generation SLS, at ALBA it is not possible to measure the beam size using direct imaging of visible radiation because of diffraction limitation. Considering light with a wavelength $\lambda$ traveling through a medium with refractive index $n$ and converging to a spot with angle $\theta$, the minimum diameter of the Airy disk at the focal point is given by:

$$d = \frac{\lambda}{2n\sin\theta}. \tag{1.1}$$

At ALBA the visible light ($\lambda = 540\,\text{nm}$) is traveling in air ($n = 1$) with a divergence of $\theta = 2\,\text{mrad}$. Therefore, the minimum measurable Airy disk diameter is $d \simeq 140\,\mu\text{m}$: much larger than the beam size ($\simeq 50\mu\text{m}$).

In SLS this problem is usually solved following two different methods:

- Using X-rays, i. e. decreasing the numerator in Eq. 1.1 by several orders of magnitude;

- Using visible light: this exploits the spatial degree of coherence of light using interferometry or polarization methods, allowing to infer the beam size.

At ALBA the workhorse for transverse beam size measurements is the X-ray pinhole[34]. A secondary approach to perform the same measurement was needed to ensure the redundancy, and improve the reliability of the machine. Moreover, using a different technique, some improvements on the measurements could be achieved. In order to measure lower beam sizes, the particular requests were to improve the pinhole resolution and to allow the possibility to measure the single bunch size along the FP, mainly to better understand the beam instabilities.

### 1.5.1 *Limitations of the X-Ray Pinhole at ALBA*

Perhaps, the most common emittance monitor in SLS is the X-ray pinhole camera due to its simplicity and reliability [35].

With the X-ray pinhole, a magnified image of the beam is obtained and its horizontal and vertical dimensions can be measured. The working principle is identical to the classical visible-light pinhole camera used by astronomers to measure the diameter of stars. The natural divergence of light, produced by an object and passing through a small entrance (the pinhole), is projected on a screen, as shown in Fig. 1.6.

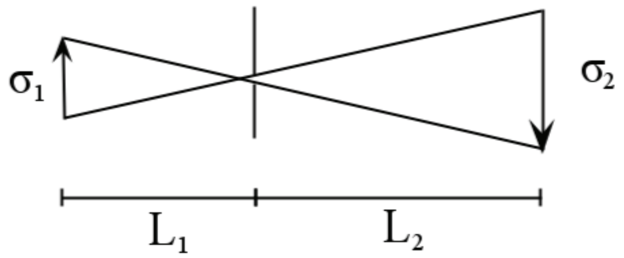

Figure 1.6: Sketch of the working principle of a pinhole camera.

The image on the screen is magnified by the ratio $\frac{L_2}{L_1}$, where $L_1$ is the distance of the source from the pinhole, and $L_2$ is distance from the pinhole to the screen. If $\sigma_1$ is the source size, the size projected at the screen is:

$$\sigma_2 = \frac{L_2}{L_1}\sigma_1. \tag{1.2}$$

At ALBA, the hard X-rays are used, which are selected by an aluminum extraction window and a copper filter (photon energy $\gtrsim 45\,\text{keV}$). A tungsten $10\,\mu\text{m}\times 10\,\mu\text{m}$ grid, located at roughly 6 m from the radiation source, acts as a pinhole camera, and produces a magnified image on a YAG screen located 13.6 m downstream. The screen (YAG:Ce) converts the X-rays into visible light, which is finally imaged through a lens system on a CCD. A schematic of the set-up is presented in Fig. 1.7.

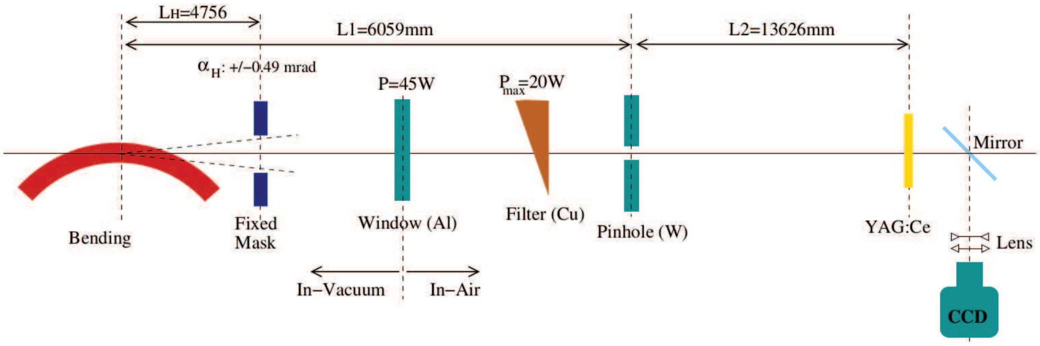

Figure 1.7: Schematic of the X-ray pinhole layout (distances not to scale).

By fitting the image and taking into account the magnification, the horizontal and vertical beam sizes are inferred. Finally, knowing the machine optics at the pinhole source point, the emittance can be calculated. A typical image from the X-ray pinhole is presented in Fig. 1.8, showing the horizontal and vertical beam sizes ($\sigma_x$ and $\sigma_x$), as well the beam tilt angle and emittance ($\epsilon_x$ and $\epsilon_y$).

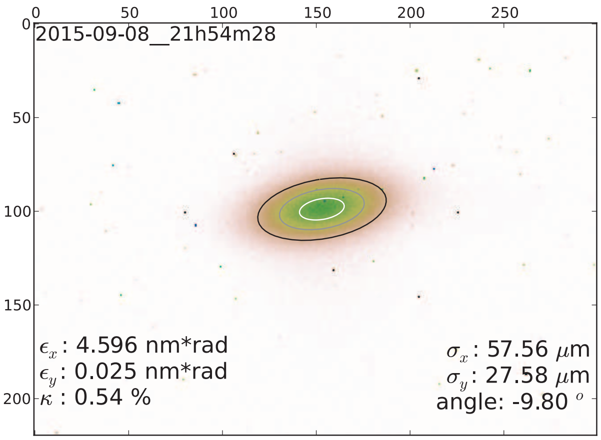

Figure 1.8: Beam image obtained with the X-rays pinhole, showing results from the data analysis.

Currently, with this technique at ALBA, the beam size measurements are limited to a minimum $\sigma \simeq 7\,\mu\text{m}$ due to diffraction and blurring effects [4]. Moreover, the time resolution of the measurement is strongly limited by the decay time of the phosphor screen (70 ns), which makes impossible to obtain the beam size of single bunches in the filling pattern. This problem, related with the conversion of X-rays, can be solved by directly looking at visible light, and using interferometric techniques, that involve the measurement of the spatial degree of coherence.

### 1.5.2 *Visible Light Techniques*

At ALBA direct beam imaging using visible light was not considered because of the diffraction limit. In this range, the beam size can be inferred from the light degree of coherence [36], which is defined as the normalized correlation of electric fields. The degree of coherence is usually measured at SLS by means of two techniques:

- the $\pi$ Polarization Method ($\pi$PM);
- the Synchrotron Radiation Interferometry (SRI).

The $\pi$PM was developed at the Swiss Light Source [37], and exploits the $\pi$-polarization intensity distribution of the synchrotron radiation to measure the vertical beam size. The visible (or UV) light coming from the beam is extracted by a full mirror, transported through the beamline to a polarizer selecting the $\pi$-polarization, and imaged through a lens on a CCD.

The vertical distribution of the $\pi$-polarization has two lobes, symmetric with respect to the orbit plane (see Appendix A.4, Fig. A.4(b)). Figure 1.9 shows the simulated $\pi$-polarization distribution of the synchrotron radiation intensity generated by a single electron passing through the ALBA bending magnet at the focal point of a focusing lens, calculated using the ALBA parameters.

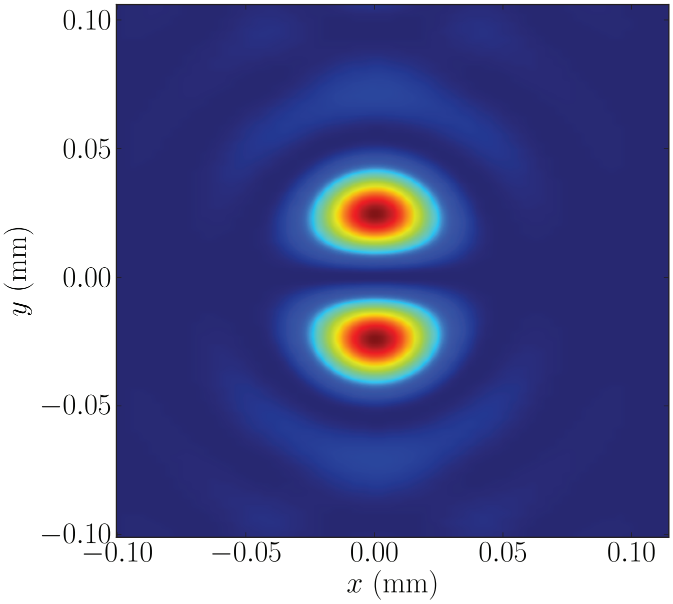

Figure 1.9: $\pi$-polarization of a single electron at the ALBA diagnostics beamline (Xanadu).

If the radiation was produced by a single electron, the valley between the lobes goes to zero; if the source is a distributed electron beam, the valley starts to increase. The larger is the beam size the higher is the valley level, as shown in Fig. 1.10.

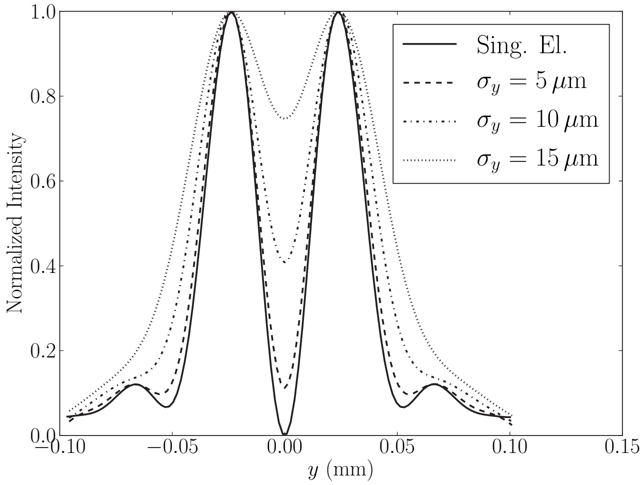

Figure 1.10: Vertical axis projections of the π-polarization of synchrotron radiation for different beam sizes.

This technique allows to measure very low beam sizes, but needs very high quality of the optical components and an extremely stable beamline. Moreover a full opening angle of the radiation has to be collected to image the two lobes. All these characteristics would require a major upgrade of the ALBA diagnostics beamline, in particular the extraction mirror. As will be explained later, ALBA diagnostics beamline is equipped with a so-called "half-mirror", which selects only the upper lobe of the radiation.

On the contrary, SRI can also be performed using the half mirror, and the requirements for flatness and stability of the optical path are less strict. The technique consists in measuring the spacial degree of coherence of the synchrotron radiation using a Young-like interferometer. Also, in this case, the working principle is the same as the one used in astronomy with the Michelson stellar interferometer to measure the diameter of a star [38]. For beam size measurements, this method was used for the first time at KEK, Japan [39].

# 2

# TIME CORRELATED SINGLE PHOTON COUNTING AT ALBA USING VISIBLE LIGHT

Time Correlated Single Photon Counting (TCSPC) using synchrotron radiation is a well established technique to measure the accelerator Filling Pattern (FP). Machines like ANKA (Germany) [40] or TLS (Taiwan Light Source, Taiwan) [41] use the visible part of the radiation, while others, such as Soleil [42] (France) or Diamond (UK) [3], use X-rays. The detector choice depends on the requirements from each machines (and the budget).

At ALBA, for selective Top-Up refilling, a dynamic range of $10^2$ is sufficient. This can be achieved performing TCSPC using visible light.

## 2.1 TIME CORRELATED SINGLE PHOTON COUNTING

The TCSPC technique allows on-line and non-destructive FP measurements using the synchrotron radiation and can provide dynamic range higher than $10^6$ [3, 43, 44].

The number of photons produced by the beam passing through a bending magnet is directly proportional to the number of electrons in the beam [10]. Therefore, the FP can be obtained by measuring the temporal distribution of the synchrotron radiation.

A scheme of the measurement set-up is presented in Fig. 2.1. The synchrotron radiation is produced by a bending magnet, the photon flux is attenuated down to less than one photon per revolution period,[1] and it is detected by a photon detector. The signal is then collected and analyzed by a Time to Digital Converter (TDC), where the machine revolution frequency and the output of the photon detector are respectively the start and the stop of the measurement respectively. The TDC measures the time difference between these two signals for several turns. The resulting time distribution of photons corresponds to an image of the time distribution of the electron bunches.

The TDC chosen for FP measurements is the PicoHarp300, by PicoQuant [45, 46]. This device has two independent but synchronized entries: *Channel 0* is used for the machine trigger input and *Channel 1* to collect the signal from the photon detector. Both channels accept negative pulses down to -1 V and both offer the possibility to set two thresholds, called respectively "Zero Crossing" and "Level". Both signals from the machine and from the PMT must be larger than the selected threshold. The threshold limits can be settled independently for the two channels.

The PicoHarp300 has a maximum counting frequency of few MHz. The collected data are distributed in a histogram with a maximum of 65536 bins, whose width can vary within 4 and 512 ps, according to the required resolution.

---

[1] The limitation of one photon per revolution period depends from TDC characteristics.

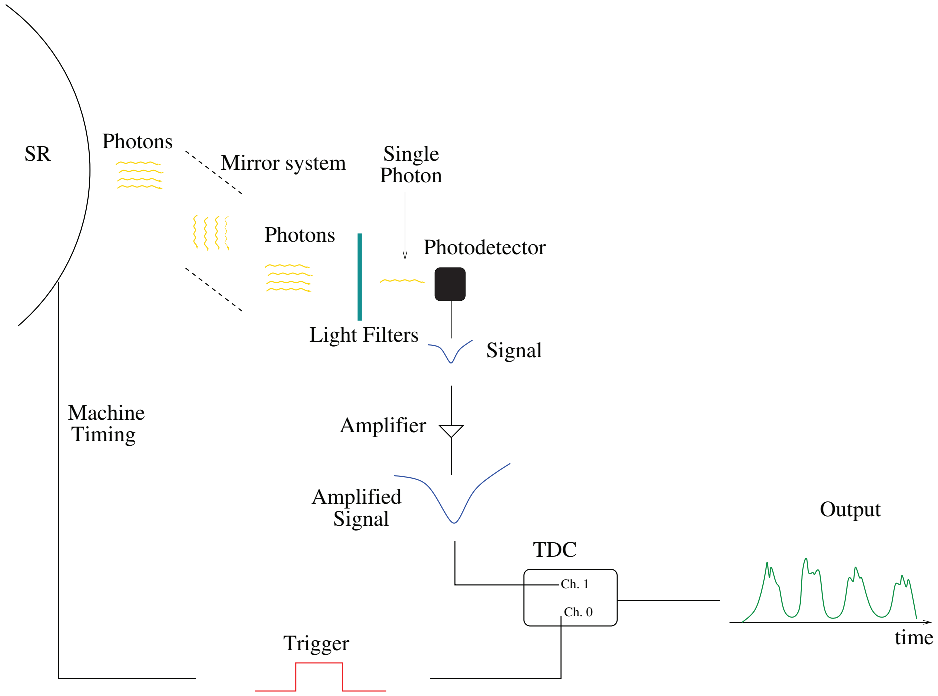

Figure 2.1: Time Correlated Single Photon Counting: the light is produced in a bending magnet, reduced to a flux of one photon per turn by light filters and then detected by a photon-detector. The detector signal provides the stop to the TDC, which triggered by the machine timing.

ALBA RF-bucket is $\simeq 2\,\mathrm{ns}$, corresponding to the $\simeq 500\,\mathrm{MHz}$ RF-frequency. Because the machine revolution time is 896 ns, the optimum bin width is 16 ps. This is the resolution routinely used during the machine operations.

A very stringent limitation of the PicoHarp300 is that the counting rate has to be lower than one per trigger cycle. This is due to the dead time of the detectors and the readout electronics, which is around few ns. During this time no event can be read and processed and this effect would be evident on the measured temporal distribution. The system would register the first photon but not the following ones, leading to an over-representation of the early photons. This effect is called pile-up [47] and has to be taken into consideration for the development and the setup of the TCSPC.

Depending on the characteristics of the radiation and the required dynamic range, typical photon detectors used in TCSPC measurements are photomultipliers (PMTs) or Avalanche Photodiodes (APDs). PMTs are mostly used to measure visible radiation, while APDs are preferred for X-rays.

In this Chapter the setup and the performances of the TCSPC using PMTs to measure visible light are presented, while the development of the same technique using an APD to detect X-rays is the topic of Chapter 3.

Two Hamamatsu devices were chosen for preliminary tests: the H10721-210 [48] and the R4124 [49]. Their main parameters are presented in Table 2.1. While the R4124 requires a current amplifier (HCA-40M-100K-C by FEMTO [50]) to convert the output into voltage signal, the H10721-210 already provides a proper output voltage for the PicoHarp300.

| | H10721-210 | R4124 |
|---|---|---|
| Photocathode Material | Ultra Bialkali | Bialkali |
| Spectral Response | 230-700 nm | 300-650 nm |
| Dark Current | 10 nA | 1-15 nA |
| Rise Time | 0.57 ns | 1.1 ns |
| Input Voltage | 5 V | 1 kV |

Table 2.1: Manufacturer specifications of the PMTs [48, 49].

Figure 2.2 shows typical signals coming from each of the two devices. The PMT H10721-210 (solid line) provides a signal with a FWHM of less than 1 ns and a rise time of 0.57 ns. The PMT R4124 (dashed line) has a wider pulse ($\simeq 4$ times wider) and a larger rise time (1.1 ns), which is anyway shorter than the ALBA RF-bucket length. Both PMTs have a rise time fulfilling the Picoharp300 requirement (shorter than 2 ns).

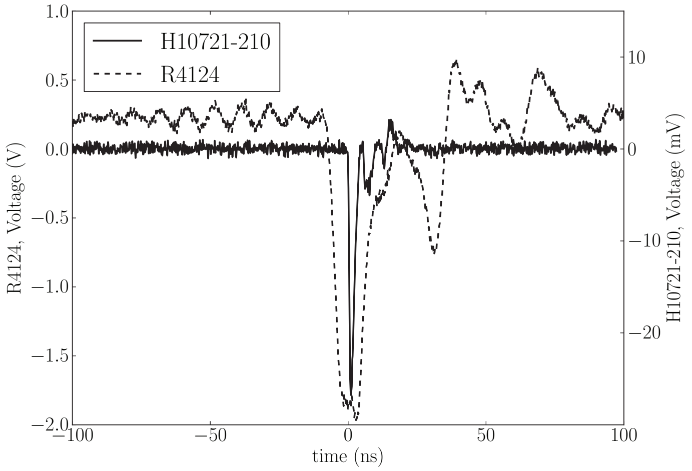

Figure 2.2: Pulse from the PMT H10721-210 (solid line) and R4124 (dashed line).

### 2.2.1 *Transit Time Spread Measurements*

The main photon detector characteristics for TCSPC is the Transit Time Spread (TTS), which corresponds to the FWHM of the transit time fluctuation between the arrival time of the photon on the photocatode and the signal generation, i.e. the time jitter of the output pulse. This parameter depends on the dynode structure and the applied voltage. To fulfill TCSPC requirements it must be shorter than a RF-bucket.

To properly measure the device TTS (expected to be $\gtrsim 100\,\mathrm{ps}$), a light pulse shorter than the TTS itself is required. This is the case of the synchrotron light produced by a single electron bunch at ALBA, whose length is normally 20 ps. In this condition, the FWHM of the distribution (obtained using the TCSPC to measure the light pulse) provides the TTS. The results are depicted in Fig. 2.3, corresponding to the TCSPC distributions produced by the H10721-210 (solid line) and the R4124 (dashed line). PMT H10721-210 shows an excellent performance: TTS is less than 100 ps, enough to distinguish different bunches.

On the other hand, for PMT R4124, the TTS is larger than 2 ns, and, therefore, two consecutive RF-buckets cannot be distinguished; moreover, some after pulses are present at $\simeq 455$ and $\simeq 475\,\mathrm{ns}$.

As a result, the PMT H10721-210 was chosen for the TCSPC measurements.

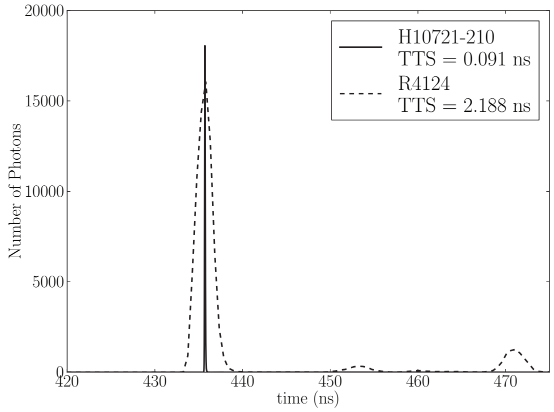

Figure 2.3: TTS measurements of PMT H10721-210 (solid line) and R4124 (dashed line).

## 2.3 THE FRONT-END SETUP (FE01)

The location chosen to host the TCSPC setup is the Front-End 01 (FE01) which provides light Xanadu, to the ALBA diagnostics beamline. A 3D model of FE01 is shown in Fig. 2.4. Here the synchrotron radiation is produced by a bending magnet, and selected by a photon shutter located 1.684 m from the source point, with an aperture of $\pm 1.84\,\mathrm{mrad}$ in the horizontal plane and $\pm 3.2\,\mathrm{mrad}$ in the vertical.

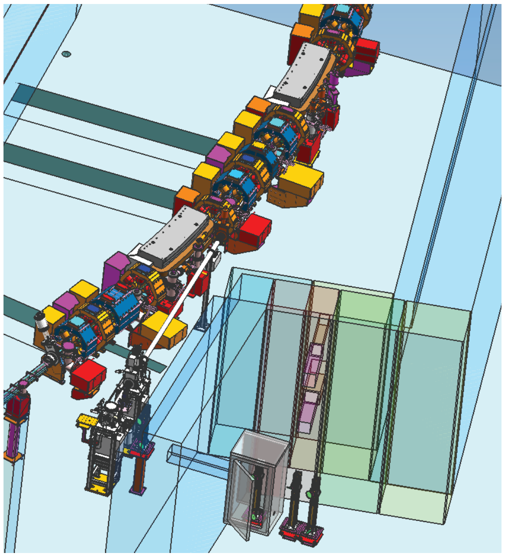

Figure 2.4: 3D model of FE01 and the optical path bringing the visible synchrotron radiation to Xanadu.

An in-vacuum mirror is located at 8.635 m from the source point. The mirror is designed to select only the upper lobe of the synchrotron radiation distribution. According to Eq. A.16 (Appendix A), describing the power distribution of the synchrotron radiation as a function of the emission angle and the photon energy (see Fig. A.4), X-rays are concentrated in narrow cone close to the orbit plane. Placing the mirror few mm higher with respect to the orbit plane allows the selection of the low energy radiation only. This allows to avoid problems related to the exposure of the mirror to X-rays (like overheating or contaminations).

A schematic of the light path is presented in Fig. 2.5. The in-vacuum mirror is oriented at 45° with respect to the radiation direction and an extraction window is located at 90° to allow the extraction of the light. To drive the beam towards the beamline, two other mirrors are located inside the tunnel and a hole is drilled in the shielding wall up to the diagnostics beamline. Finally, 5 mirrors bring the light to the optical table, where it can be manipulated and analyzed.

The layout of the endpoint of FE01 is shown in Fig. 2.6, where the synchrotron radiation is drawn as a yellow fan in the front view (Fig. 2.6(a)) and a yellow arrow in the top view (Fig. 2.6(b)). The extraction mirror is shown as a light-blue rectangle. The orange parallelepiped is the copper absorber used to stop the X-rays. Even if the absorber is not polished, it is still able to reflect visible light. Moreover it is oriented with an angle of 45° and can guide the light towards a detector (represented as a black box in Fig. 2.6(b)) through a secondary extraction window made of silica.

Since the Xanadu extraction mirror only reflects the upper lobe of the radiation fan, one can always use the lower lobe, reflected by the absorber, with no interference with beamline operation.

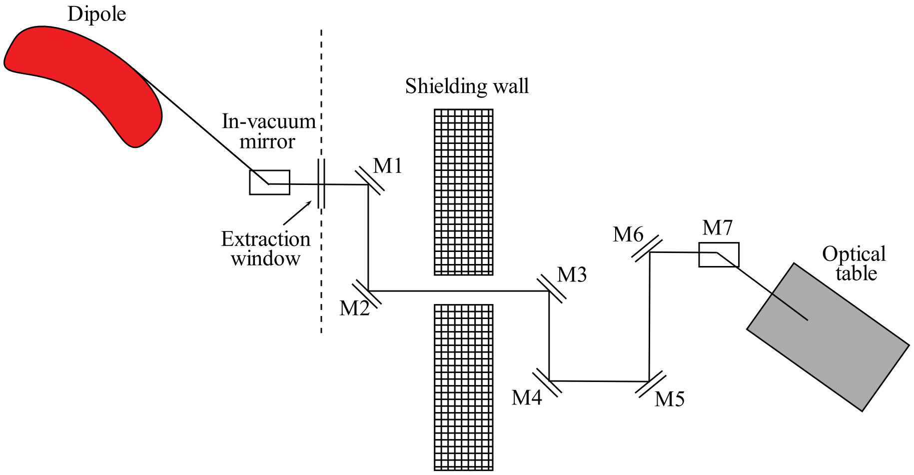

Figure 2.5: Synchrotron light path from the source to the optical table.

The fact that the reflectivity of the unpolished absorber is not maximum does not affect the result, since the light must be attenuated in any case to have the proper flux rate for the TCSPC: less than one photon per turn.

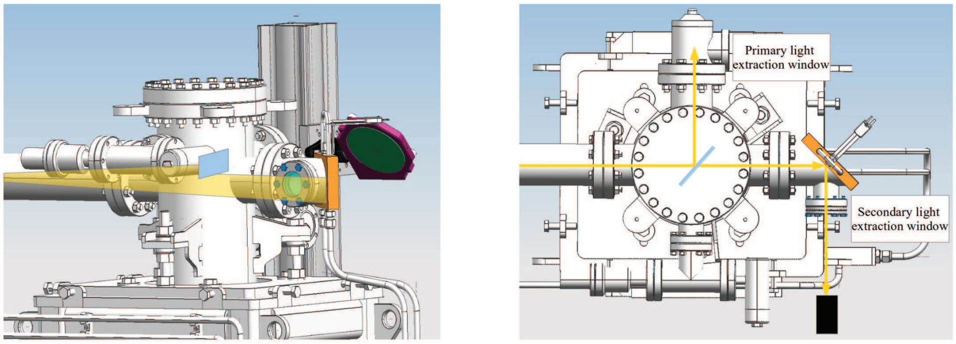

(a) *Front view.* (b) *Top view, the black box represent the PMT.*

Figure 2.6: Layout of FE01 endpoint and representation of the light path.

### 2.3.1 *TCSPC Station*

In order to avoid contamination from the visible ambient light in the tunnel, a black box was designed to host the TCSPC setup. The box is directly connected to the secondary extraction window of FE01.

The PMT is enclosed in a small box in order to make the cabling easier (see Fig. 2.7(a)). On the front part of the box a lens tube is assembled, containing a Neutral-Density

(ND) filter $10^5$ [51] and a 633 nm band pass filter [52] in order to shield the radiation and decrease the flux to less than one photon per turn. In front of the PMT box, a motor allows to place a gradual ND filter [53] (from 1 to $10^5$) to keep photon flux lower than one photon per turn when the current in the storage ring increases. Lead sheets are located around the PMT to reduce the noise produced by particle losses and provide radiation protection for the PMT.

Figure 2.7 shows two pictures of the setup. In the first the container is open to show all the components, while in the second the box is closed.

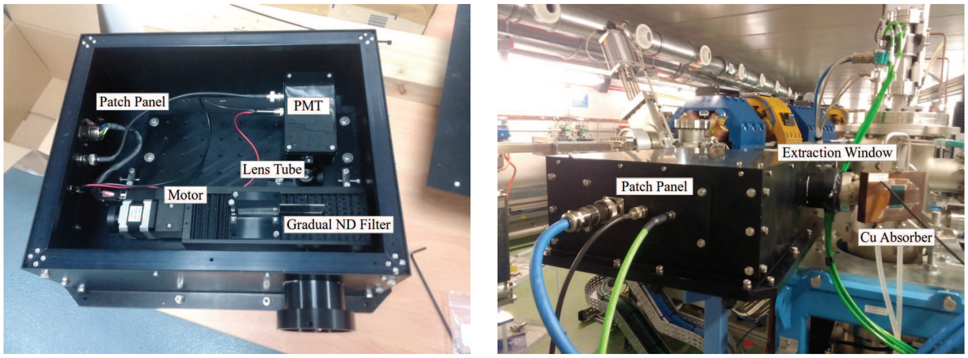

(a) *Container open: the PMT is inside the small black box, the c-mount lens tube is attached to the PMT box, and the motor holding the gradual ND filter is in front of it.*

(b) *Container assembled: the box is hermetically closed to avoid ambient light. Cables are connected to the patch panel and the box is directly connected to the extraction window. The Cu absorber used as a mirror is also visible.*

Figure 2.7: Final setup for TCSPC using visible light.

The PMT power supply and the required electronics to properly control the motor are located outside the tunnel. The PMT output signal is connected to the Picoharp300 (located in Xanadu), which acquires the data and sends them to the ALBA control system.

## 2.4 FILLING PATTERN MEASUREMENTS

### 2.4.1 *Single Bunch Measurements*

A single bunch of 5 mA was injected into RF-bucket 6 ($\simeq$ 12 ns late with respect to the RF signal) as shown in Fig, 2.8. The response of the PMT shows a sharp peak, with a maximum of roughly $6 \times 10^4$ counts per bin, centered around the selected RF-bucket (dashed vertical lines in Fig. 2.8). The PMT signal decays by almost three orders of magnitude in the 2 ns delimiting the RF-bucket length, which defines a dynamic range of $10^3$. The noise level far from the bunch is about 5 counts per bin, leading to a more general dynamic range of $10^4$.

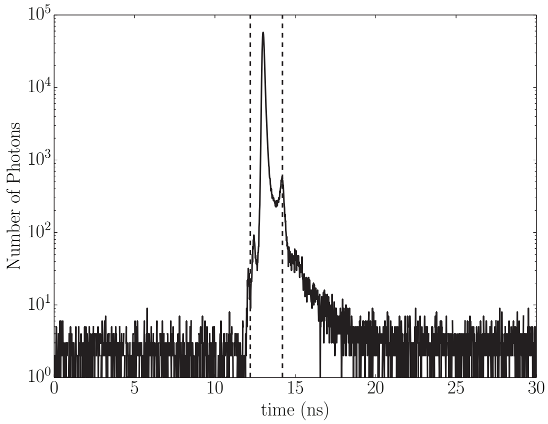

Figure 2.8: TCSPC to measure a single bunch of 5 mA using the PMT. Data were acquired for 15 s. The horizontal dashed lines represent the RF-bucket length.

### 2.4.2 *Filling Pattern Measurements*

TCSPC using visible synchrotron radiation is nowadays used routinely at ALBA for FP monitoring during machine operation, where 130 mA of current are distributed among the 10-train FP (last plot of Fig. 1.4). The integration time used to perform TCSPC is 10 s, with bin width of 16 ps for the Picoharp300.

Typical raw data is presented in Fig. 2.9. In the top plot, where the horizontal scale is machine period, all the ten trains of the ALBA FP are presented. The bottom plot is the zoom of the first train of the FP. The peaks have a modulation of 2 ns corresponding to the 32 bunches of the train: the number of photons counted each 2 ns is proportional to the amount of current per bunch. Note that not all bunches corresponds to the same amount of current due to the instability of the injection system: the goal of the selective Top-Up is to equalize the charge on these bunches using the Top-Up injection.

### 2.4.3 *Data Analysis*

Data treatment consists of performing the integration over the horizontal bins in steps of 2 ns (time length of a RF-bucket). The final histogram describing the 448 RF-buckets is normalized and scaled by the DCCT current.

To get rid of the noise in the gaps a cut of the 1% with respect to the maximum current per RF-bucket is applied, and all the RF-buckets with a current below this threshold are considered empty. Figure 2.10 presents the final FP and a zoom into the first train: no “spurious” bunches are present in the gaps, in contrast to results obtained with the other technique used at ALBA, the Fast Current Transformer (see Fig. 1.5).

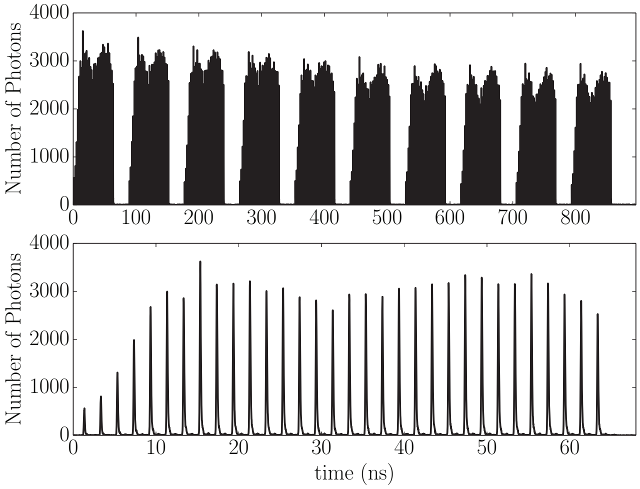

Figure 2.9: Results form TCSPC using visible light. The top plot is the whole beam while the bottom plot is a zoom on the first train.

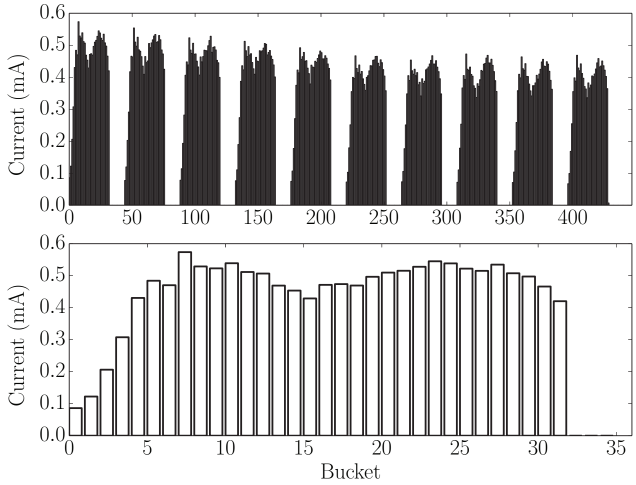

Figure 2.10: Results form TCSPC data analysis. In the first plot the full FP, while the bottom plot shows a zoom of the first train of 32 bunches.

# 3

# TIME CORRELATED SINGLE PHOTON COUNTING AT ALBA USING X-RAYS

In view of (possible) future time resolved experiments at ALBA, bunch purity measurements with a dynamic range of $\simeq 10^6$ will be needed. To this aim, the Time Correlated Single Photon Counting (TCSPC) technique using an Avalanche Photo-Diode to detect X-rays was tested. These devices are designed for studies using light in the range of [200, 1100] nm but, depending on their technical characteristics, might also be used to detect single soft X-rays, which are able to generate a pulse with a high signal-to-noise ratio.

## 3.1 AVALANCHE PHOTO-DIODE

Based on the experience in other machines like Diamond (UK) and Soleil (France) [3, 42], the device chosen to perform TCSPC using X-rays is the APD module C5658 by Hamamatsu [54]. The silicon detector included in the module is the Hamamatsu Si APD S12023-02 [55], with an effective area of 0.2 mm in diameter. The ancestor of this model was used to perform TCSPC for the first time using X-rays at the KEK Photon Factory positron storage ring (see [56, 57]). The sensor is characterized by a 9 µm depletion layer where a sufficiently high reverse bias-voltage is applied. The thickness of the layer allows absorption of the X-rays in the sensitive zone and generation of the related signal.

The full APD integrated module also contains a bias power supply and a low noise amplifier. The gain of the module is set to 50, and the detection limit is up to 1 GHz. In order to guarantee a stable operation of the APD, a thermosensor and a temperature-compensated bias power supply are also present in the integrated module. Figure 3.1 shows the electronic schematic of the APD.

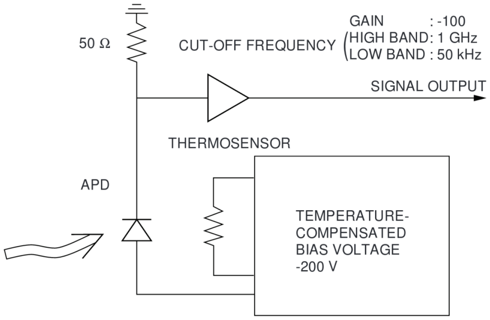

Figure 3.1: Schematic of the APD C5658 integrated module.

This kind of detector is designed to detect light in the range from 200 to 1100 nm; however, since the APD will be used for X-ray detection, the original borosilicate window was removed to avoid the absorption of most of the photons at the foreseen energy. Main specifications of the module and the silicon detector are listed in Table 3.1.

| APD Module C5658, Si APD S12023-05 Sensor | |
|---|---|
| Photocathode Material | Silicon |
| Spectral Response | 200-1100 nm |
| Gain ($\lambda = 800\,\mathrm{nm}$) | 50 |
| Noise Level (Dark State) | 16 nW |

Table 3.1: Manufacturer specification of the APD and the related sensor [54].

The 16 nW "Noise Level", considering the 1 GHz detection limit, corresponds to the signal given by a single photon with an energy of 100 eV. For this reason, if one photon with an energy in the order of 1 eV, impinges on the device, the produced signal is hidden by the noise. The APD C5658 is not designed to perform photon counting in this mode, but more energetic photons, such as X-rays with an energy in the order of few keV, can be detected individually and generate a clear signal. The real advantage of using X-rays is that no other sources beside the beam are present close to the detector, and the background coming from the visible light is negligible.

## 3.2 FEASIBILITY STUDIES

Feasibility studies were carried out both to understand if the efficiency of the APD was sufficient to perform TCPSC, and to choose the best location for the device.

Following experiments at other machines [56, 3, 42], FP can be measured using secondary X-rays produced from the collision between the synchrotron radiation and metal (copper). When copper is bombarded with hard X-rays, some electron transitions to the innermost K-shell from an L-shell are exited and soft X-rays (about 8 keV) are emitted. Figure 3.2 shows position of the peaks for this kind of transition in copper. The so-called $K_\alpha$ and $K_\beta$ transitions are very fast (in order of 10 ps) so they can be used to indirectly detect the photons arrival [8]. Moreover, the fluorescence yield is about 50% for copper, as shown in the rightmost plot in Fig. 3.2. This means that roughly half of the X-rays that are absorbed will produce the transition and generate softer X-rays.

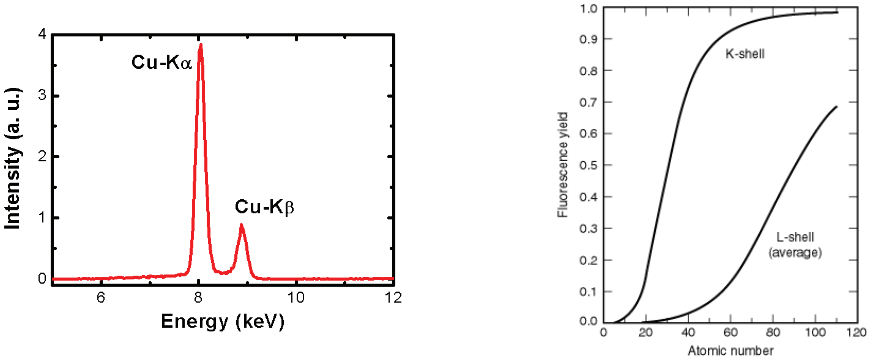

Figure 3.2: Intensity of the $K_\alpha$ and $K_\beta$ transition of copper and fluorescence yield for metals [8]. The atomic number of copper is 29.

### 3.2.1 *Estimation of Detectable Photons at FE01*

To verify the feasibility of TCSPC, one needs to estimate the number of $K_\alpha$ photons impinging on the sensitive part of the APD.

This estimation was done simulating the generation of synchrotron radiation and its interaction with matter, by means of “X-ray Oriented Programs” (XOP) [58], an open source software developed at the European Synchrotron Radiation Facility (ESRF), to perform calculations of the generation of synchrotron radiation by different sources, and its interaction with matter.

The simulated spectrum of synchrotron radiation produced by ALBA bending magnets and selected by the photon shutter of FE01 (Sec. 2.3) is shown in Fig. 3.3, for a beam current of 130 mA, i.e. the typical current during normal operation at ALBA. Integrating over all energies, the total flux of photons per second is expected to be:

$$N_{Ph} \simeq 4 \times 10^{17}\,\frac{\mathrm{ph}}{\mathrm{s}} \tag{3.1}$$

with peak energy at $\simeq 12\,\mathrm{keV}$.

The total cross-section of copper for photons with energies between 1 eV and 100 keV is shown in Fig. 3.4. The sharp peak around 8 keV corresponds to the $K_\alpha$-transition.

Placing the APD in same position of the PMT (Fig. 2.6), the $K_\alpha$ photons reaching the APD are:

$$N_{APD} = \mathcal{T} \times \Delta\Omega \times N_{K_\alpha}, \tag{3.2}$$

where $\mathcal{T}$ is the transmission through the 3 mm silica window, $\Delta\Omega$ is the solid angle covered by the APD sensor, and $N_{K_\alpha}$ corresponds to the total number of $K_\alpha$ photons generated by the synchrotron radiation hitting the Cu absorber (see Fig. 2.6(b)).

$N_{K_\alpha}$ is inferred from:

$$N_{K_\alpha} = F_{K_\alpha} \int_0^{x_R} dx \int_{E_{K_\alpha}}^{\infty} N_{Ph} dE. \tag{3.3}$$

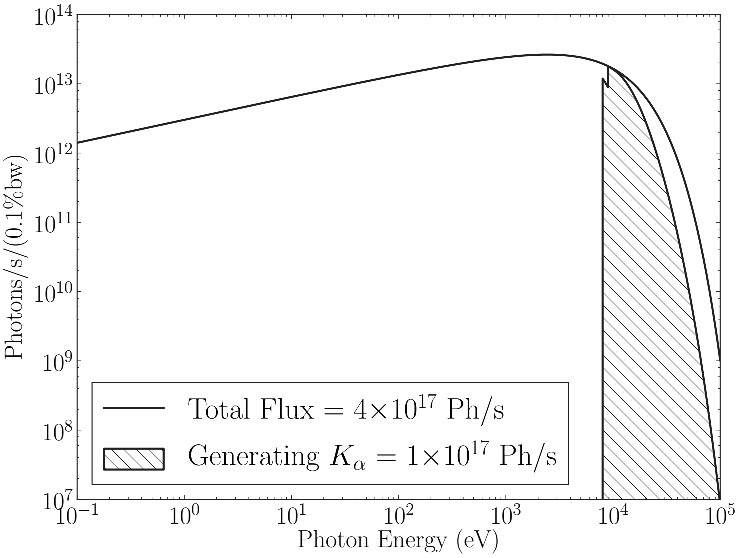

Figure 3.3: Synchrotron radiation spectrum generated from one of the ALBA bending magnets. The dashed area represents the photons able to produce $K_\alpha$-transition within 20 µm from the Cu surface.

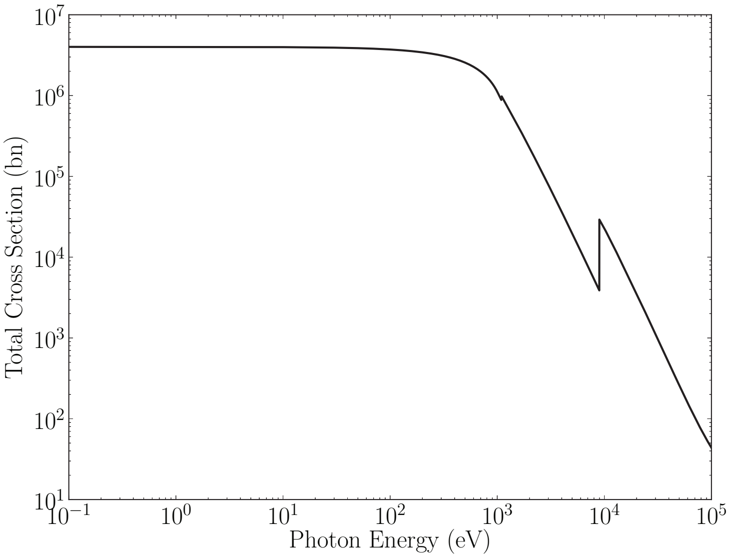

Figure 3.4: Total cross section of photons in Cu. The sharp peak around 8 keV corresponds to the $K_\alpha$-transition.

This accounts for the synchrotron radiation photons ($N_{Ph}$) hitting the Cu absorber with an energy larger than the typical $K_\alpha$ energy ($E_{K_\alpha}$), and absorbed in the first $X_R = 20\,\mu m$: a length corresponding to the attenuation length of $K_\alpha$ photons in copper, scaled by the factor $F_{K_\alpha}$, which is the fluorescence yield of the $K_\alpha$ transition in the material.

Assuming a fluorescence yield of $F_{K_\alpha} = 0.5$ (see the rightmost plot in Fig. 3.2), and taking into account the photons with $E > E_{K_\alpha}$, one obtains:

$$N_{K_\alpha} = 1 \times 10^{17}\,\text{ph/s}. \tag{3.4}$$

If the APD is located at $R = 200\,\text{mm}$ from the copper absorber, and taking into account the radius of the sensor $r = 0.1\,\text{mm}$, the solid angle covered by the detector is:

$$\Delta\Omega = \frac{\pi r^2}{4\pi R^2} = 6 \times 10^{-8}\,\text{srad}. \tag{3.5}$$

From Eq. 3.4 and Eq. 3.5, and considering the transmission of $\mathcal{T} = 2 \times 10^{-5}$ (see Fig. 3.5), according to Eq. 3.2 the flux of $K_\alpha$ photons impinging on the APD is:

$$N_{APD}^{FE01} = 1.2 \times 10^5\,\text{ph/s}. \tag{3.6}$$

Since the required photon flux for TCSPC is $< 1$ ph/turn (or, equivalently, for ALBA $\simeq 10^6$ ph/s), $N_{APD}^{FE01}$ is quite low. APD efficiency for X-rays is not considered in this calculation, but, its effect can only reduce $N_{APD}^{FE01}$.

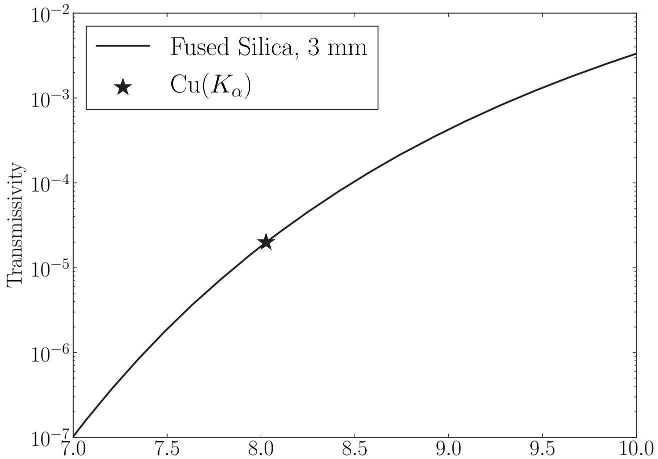

Figure 3.5: Transmission curve for Si with respect to the photon energy [59]. The marker shows the position of energy corresponding to $K_\alpha$.

### *Estimation of Detectable Photons at FE34*

Another possible solution is to place the APD at the X-ray pinhole frontend FE34 and look at the copper filter used for X-ray attenuation, as presented in Sec. 1.5. Here, the bending magnet generating the synchrotron radiation has the same characteristics as the one providing light to FE01. The X-rays are extracted through a 1 mm aluminum window, selecting photons with an energy larger than 1 keV.[1] A copper filter with a minimum thickness of 0.1 mm selects X-rays with an energy larger than 30 keV to perform pinhole imaging.

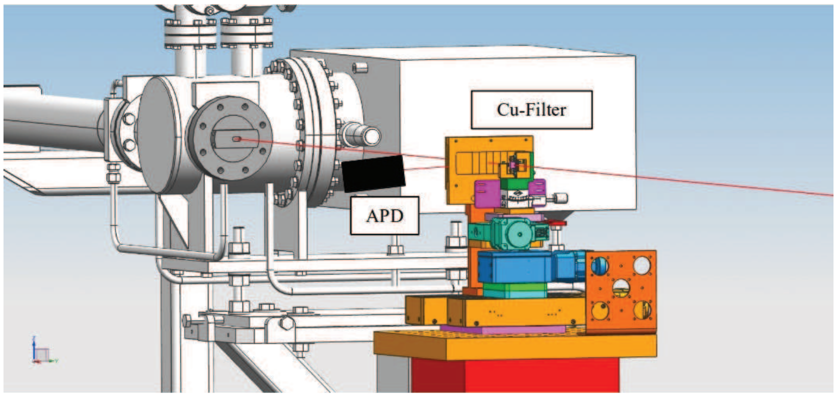

Figure 3.6: FE34: the X-rays (red line) are extracted through the aluminum window and filtered by a copper absorber (orange parallelepiped). The red line outgoing from the filter represents a part of the $K_\alpha$ transition reaching the APD (black rectangle).

The filter can be used as source of $K_\alpha$ photons (similar to the absorber in FE01). The thickness of copper is not a problem since only X-rays absorbed in the first $X_R = 20\,\mu\text{m}$ of Cu provide suitable $K_\alpha$ photons. For this reason, all estimations for the $K_\alpha$ photons at FE01 are still valid in this location. On the other hand, the APD must be located closer to the copper filter $\simeq 100\,\text{mm}$) and covers a larger solid angle. No fused silica window is used in this case, so the estimated flux on the APD sensor is:

$$N^{FE34}_{APD} = \Delta\Omega^{FE34} \times N_{K_\alpha} = 2.4 \times 10^{10} \text{ph/s}, \tag{3.7}$$

i.e. $\simeq 5$ orders of magnitude larger with respect to the estimation at the FE01 location.

In order to finally assess the proper location, the photon flux arriving at the candidate location ($N^{FE01}_{APD}$ and $N^{FE34}_{APD}$) need to account for the APD efficiency in the X-ray regime. The manufacturer does not provide this parameter: for this reason a characterization using one of the ALBA soft X-rays beamline (XALOC) was performed.

---

[1] Note that 1 keV$< E_{K_\alpha}$, thus results presented in Eq. 3.3 are unchanged.

The idea is to generate X-rays at the $K_\alpha$ energy ( $\simeq 8$ keV) and compare the number of detected photons to the number of photons reaching the detector. This is performed at the XALOC beamline [60], which is mainly dedicated to macromolecular crystallography.

The photon source is a 2 m-long pure-permanent-magnet in-vacuum undulator (IVU21) with a minimum gap of 5.7 mm. The photon beam produced in the undulator is extracted through a 400 µm diamond window that cuts most of the photons with energy lower than 5 keV.

The final photon energy is selected by a monochromator and the beam is focused by a pair of mirrors, each focusing in either vertical or horizontal directions.

The photon beam size at the focal point is 52 µm in horizontal and 5.5 µm in the vertical direction. The beam can be defocused without losing the centroid position. The design photon flux is around $10^{12}$ ph/s at 400 mA. The end station, where experiments are performed, is equipped with positioning tables to locate the samples at the desired position.

### 3.3.1 *Experimental Setup*

A sketch of the experimental setup is presented in Fig. 3.7. The APD was mounted on the positioning tables in the hutch, which moves transversally and longitudinally. In front of the APD, a calibrated Transmissive Photo-Diode (TPD) DDS1 [61] was mounted to measure the photon flux by means of an electrometer.[2]

The final alignment between the X-ray beam and the detectors was found by maximizing the two signals. A picture of the APD and the TPD mounted on the positioning table is presented in Fig. 3.8.

Figure 3.9 shows the current read at different relative position between the APD-TPD system and the X-ray beam, in the horizontal and vertical direction respectively. The TPD, with a detector diameter of 5 mm, is much larger with respect to the APD (0.2 mm diameter): for this reason the APD is the key element for the alignment process.

After the alignment, the APD was connected to the oscilloscope to monitor the shape of the output pulse. The beamline flux was reduced by means of filters up to when a single pulse of stable amplitude appeared on the oscilloscope screen. Pulses of 6,7,8, and 9 keV were observed (as shown in Fig. 3.10). The shape of the signal was clean, with a high signal-to-noise, ratio and its amplitude increased with the photon energy.

### 3.3.2 *Efficiency Results*

To measure the APD efficiency (and in general, to perform TCSPC), the APD output had to be connected to the Picoharp300. Because the APD has a positive output, its

---

[2] The TPD DDS1 was developed by the ALBA electronic devision, in collaboration with ALIBAVA.

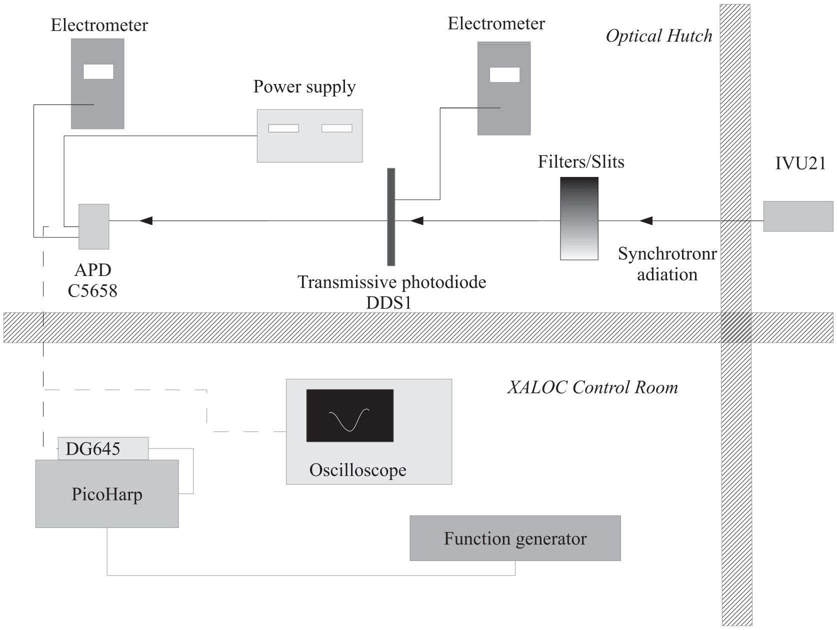

Figure 3.7: Experimental setup for the APD efficiency measurements.

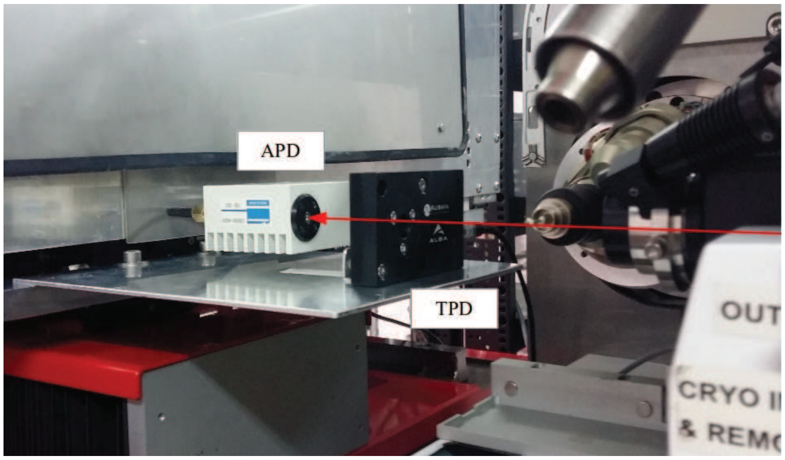

Figure 3.8: APD and TPD mounted on the positioning table. The red arrow represent the X-rays fan.

signal had to be inverted since the Picoharp300 only accepts negative pulses with amplitudes in the range [-1, 0] V. This was done using the DG645 Delay Generator: the details of this inversion system are presented in Appendix B.

The beamline was tuned to produce photons at 8 keV and the APD inverted signals were sent to the Picoharp300 and accumulated during 100 s.

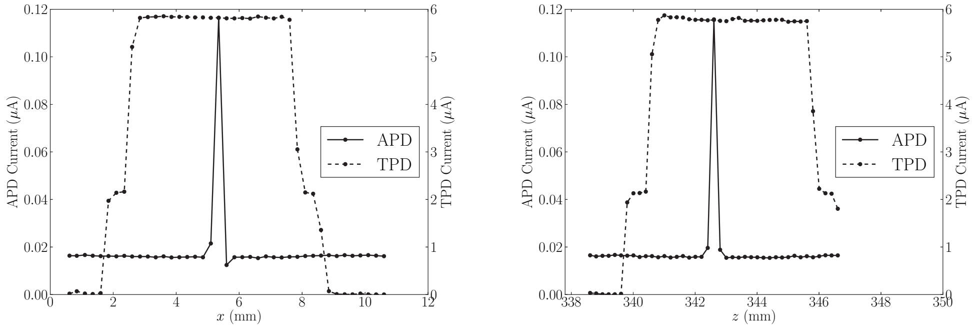

(a) *Horizontal*.

(b) *Vertical*.

Figure 3.9: Horizontal and vertical scan of the APD-TPD system.

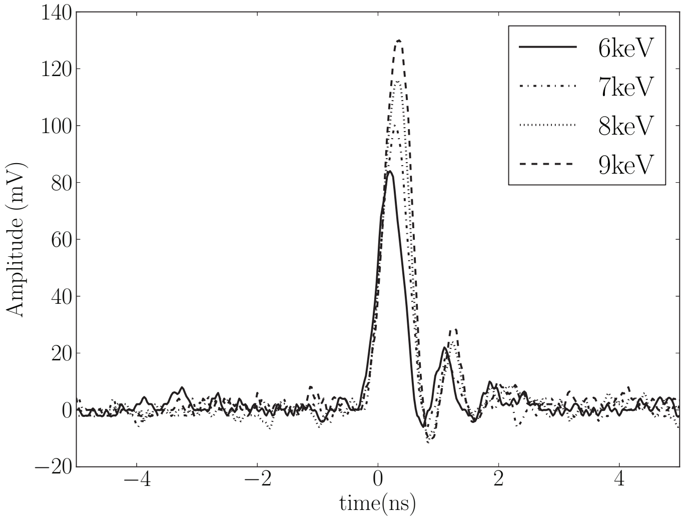

Figure 3.10: Pulses produced by a single photon at different photon energies.

The current reading by the TPD was $I_{TPD} = 2.54\,\text{nA}$, the TPD transmittance for 8 keV photons was $T_{TPD} = 0.98$ (provided by the manufacturer), and, using the provided responsivity curve shown in Fig. 3.11, the impinging photon flux was:

$$\Phi_{TPD}\left[\frac{\text{ph}}{\text{s}}\right] = \frac{I_{TPD}[\text{A}]}{R_{TPD}\left[\frac{\text{A}}{\text{W}}\right] \times E[\text{eV}] \times 1.6002 \times 10^{-19}} \times T_{TPD} \tag{3.8}$$

$$\Phi_{TPD} = 7 \times 10^{7}\,\frac{\text{ph}}{\text{s}}.$$

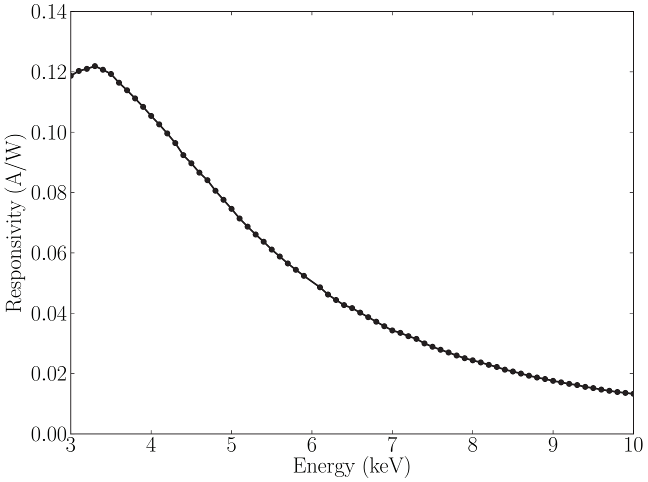

Figure 3.11: TPD Responsivity: measured points and interpolated curve.

On the other hand, the number of photons counted by the APD in 100 seconds was:

$$N_{\text{APD}} = 7 \times 10^4 \,\text{ph}, \tag{3.9}$$

leading to a measured flux of

$$\Phi_{\text{APD}} = 7 \times 10^2 \,\frac{\text{ph}}{\text{s}}. \tag{3.10}$$

The efficiency of the device at 8 keV was finally calculated as:

$$\mathrm{Eff}_{\text{APD}} = \frac{\Phi_{\text{APD}}}{\Phi_{\text{TPD}}} \simeq 1 \times 10^{-5}. \tag{3.11}$$

## 3.4 FINAL SETUP AND RESULTS

According to Sec. 3.2, if the APD is located at FE34, the expected flux of photons that can reach the APD is $2.4 \times 10^{10}$ ph/s (Eq. 3.7). Taking into account the obtained efficiency, the APD should detect:

$$n_{\text{exp}}^{\text{FE34}} = 2.4 \times 10^5 \,\frac{\text{ph}}{\text{s}}, \tag{3.12}$$

which is an acceptable value when performing photon counting, since it corresponds to less than one photon per turn.

On the other hand, it is not possible to place the APD at the PMT location since it would provide $10^5$ less photons per second, leading to a detection frequency of $n_{\text{exp}}^{\text{FE01}} = 0.1$ ph/s: too low to perform reliable FP measurements.

### 3.4.1 *Experimental Setup*

The APD is mounted on a shelf installed in the pinhole filter holder. The APD is located at roughly 100 mm and 45° with respect to the direction of the incoming radiation, in order to avoid the X-ray fan pass directly through the APD (and not to interfere with the pinhole operation). A picture of the set-up at FE34 is presented in Fig. 3.12.

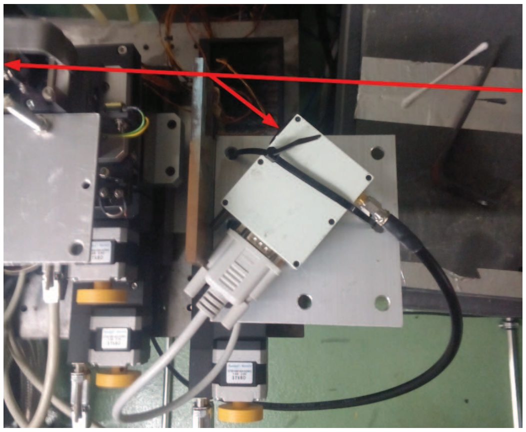

Figure 3.12: APD setup at FE34. The detector is located at roughly 100 mm and with an angle of 45° with respect to the filter. The long red arrow represents the X-ray fan, while the short one represents the $K_\alpha$ photons reaching the APD.

During normal machine operation with a stored current of 130 mA, the APD counting rate is

$$n_{meas} \simeq 4 \times 10^4 \, \frac{\mathrm{ph}}{\mathrm{s}}, \tag{3.13}$$

enough to perform photon counting, but almost one order of magnitude lower than the expected one (Eq. 3.12). This discrepancy might depend on the alignment and the orientation of the detector with respect to the filter which was performed manually: if the APD is located 10 mm away with respect to the designed 100 mm, the flux impinging on the detector is reduced by 20%. Moreover, if the sensor is not parallel to the source, the absorption of the X-rays in silicon might be decreased.

### 3.4.2 *Results: Single Bunch Measurements*

Single bunch measurements using the APD were performed. Data were acquired for 200 s and a bunch of 3.5 mA was placed at RF-bucket 3. Results are presented in Fig. 3.13. Also in this case the vertical dashed lines delimit the RF-bucket length.

In the APD case the detected signal decays by two orders of magnitude within the RF-bucket length, leading to an estimated dynamic range of $10^2$. On the other hand, no noise surrounds the main bunch, leading to a dynamic range better than $10^4$

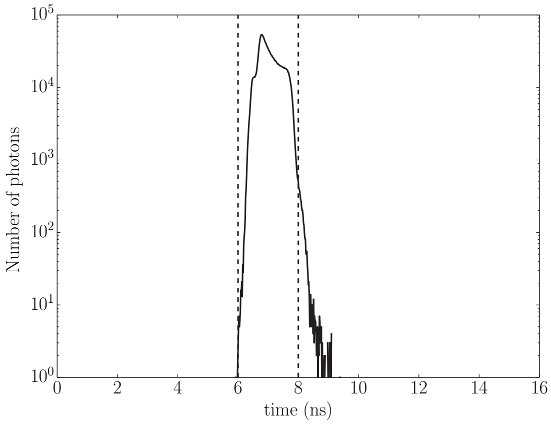

Figure 3.13: TCSPC to measure a single bunch of 3.5 mA. Vertical dashed lines represent the RF-bucket length.

when considering the farther RF-buckets and promises results for future bunch purity measurements.

From the same measurement the Transit Time Spread (TTS) was inferred (as in Sec. 2.2.1). The FWHM of the TTS distribution (Fig. 3.13) is:

$$\text{TTS}_{\text{APD}} = 0.47\,\text{ns}, \tag{3.14}$$

which is actually shorter than the length of a RF-bucket, although the shape of the signal is not optimal for this application. The width of the distribution is slightly larger than 2 ns with the consequence that, when performing TCSPC for FP measurements, the number of photons per RF-bucket is not exactly proportional to the corresponding number of electrons, and the information from consecutive RF-buckets is mixed.

### 3.4.3 *Results: Filling Pattern Measurements*

The consequence of wide TTS distribution is evident when measuring the machine FP (see Fig. 3.14). Data were acquired during a normal operation day for 100 s. The machine was operating in Top-Up with a stored current of 130 mA. As for the PMT (see Fig. 2.9), the bin width of the Picoharp300 was set to 16 ps.

The large tail at the end of each train is due to response of the APD to the single bunch (see Fig. 3.13) and generates problems when extracting the FP by means of the data analysis. The FP measured with the APD is presented in Fig. 3.15: many spurious bunches are present between trains due to the noise in the gaps. This can be better seen in the zoom of the first train (bottom plot in Fig. 3.15). While RF-buckets 32-44 are empty, the measurement done with the APD shows them filled.

It is clear that the APD is not able to clearly distinguish different bunches. Moreover, a peculiar modulation of the train and of the noise in the gap is present: the central trains

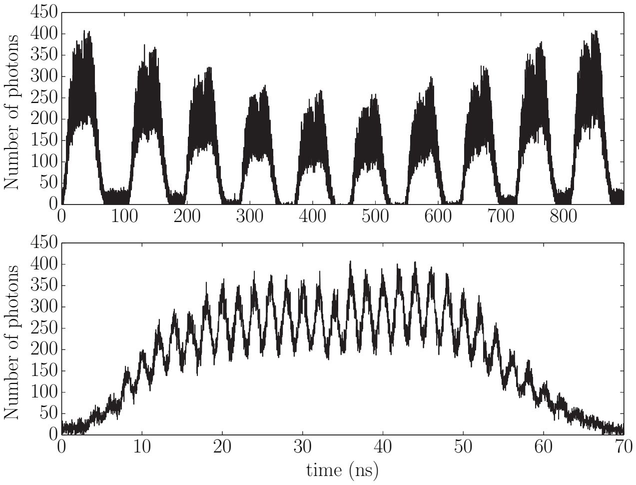

Figure 3.14: Results from TCSPC using X-rays after 100 s of acquisition. The top plot is the whole beam, while the bottom plot is a zoom on the first train.

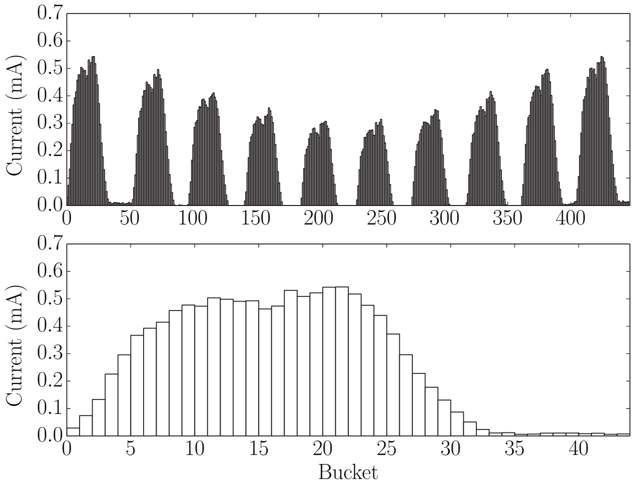

Figure 3.15: Results from the TCSPC data analysis applied to the APD measurements. In the top plot the full FP is shown, while the bottom plot represents a zoom of the first train.

look less filled with respect to the "lateral" ones. This effect is not fully understood, but may be related with the response of the APD when detecting X-rays at high repetition rate.

It is important to mention that, in order to obtain more flux on the detector, the APD module was sent back to the manufacturer to change the sensor for one with a larger diameter (0.5 mm). The manufacturer reported a problem in the cooling circuit of the APD which could also be the cause of this behavior.

# 4

# TCSPC: RESULTS AND APPLICATIONS

Both the Photomultiplier (PMT) H10721-210 and the Avalanche Photo-Diode (APD) C5658 by Hamamatsu were tested as photon detectors for the ALBA Time Correlated Photon Counting (TCSPC) setup. The devices have different characteristics and are suitable for different applications during the machine operation.

Setting-up the TCSPC gave the possibility to proceed with the implementation and commissioning of several operation techniques which needs a precise, continuous and on-line Filling Pattern (FP) monitoring.

## 4.1 COMPARISON BETWEEN PHOTOMULTIPLIER AND AVALANCHE PHOTO-DIODE

Table 4.1 compares the most relevant characteristics of both detectors, and its related performance for TCSPC measurements. Next, related pros and cons for each detector are discussed.

| | PMT H10721-210 | APD C5658 |
|---|---|---|
| Photocathode Material | Ultra-Bi-alkali | Silicon |
| Radiation used | Visible light (630 nm) | X-Rays (8 keV) |
| Radiation Shielding | Yes | No |
| Pulse Width | $\simeq$2 ns | $\simeq$1 ns |
| Conversion System | No | Yes |
| Transit Time Spread | 0.091 ns | 0.47 ns |
| Counts/sec @ 130 mA | $\simeq 5 \times 10^5$ | $\simeq 4 \times 10^4$ |
| Dynamic Range Closer Buckets | $\simeq 10^3$ | $\simeq 10^2$ |
| Dynamic Range Further Buckets | $\simeq 10^4$ | $> 10^4$ |

Table 4.1: Comparison between the PMT and APD, and TCSPC performances using one of the two detectors.

As extendedly explained in Chap. 2 and Chap. 3 the two detectors are used for different kind of radiations. PMT is used to detect visible light, while the APD is used to detect X-rays. In the first case the quantum efficiency is high and the radiation needs to be shielded to perform single photon counting. The APD is used to detect X-rays, despite to its design purpose. The Efficiency of the device, which was directly measured in-house (Sec. 3.3), is low (around $10^{-5}$) but it is still enough for TCSPC measurements. On the other hand the use of X-rays instead of visible light brings an evident advantage regarding the random noise level. In the first case one must be very careful that light not coming from the synchrotron radiation beam reaches the detector: this is quite difficult since the light in the tunnel is always on. On the contrary, when using the APD to detect X-rays, the signal is very well defined and depends on the energy of the detected photons: the highest is the energy, the highest is the photon pulse, as shown in Fig. 3.10. Visible light photons or even the standard ambient light does not provide a signal comparable with the one generated by X-rays. This high signal to noise ratio contributes to the achievement of a high dynamic range, at least when measuring a single bunch, and makes the device the most suitable for future bunch purity measurements.

However the PMT has a better Transit Time Spread (TTS) with respect to the APD, and the results when measuring the FP are more reliable.

Since the priority at ALBA is currently to properly measure the FP, the system using the PMT was chosen to routinely monitor the beam from the Control Room. It offers a reliable and fast measurement of the FP, with a dynamic range in the order of $10^3$, which is a factor 10 better than the previous ALBA measurement system: the Fast Current Transformer [2], which has been left as a back-up tool in case of failure of the TCSPC.

## 4.2 SINGLE BUNCH BUCKET SELECTION

The Single Bunch Bucket Selection (SBBS) operation mode allows to inject a given amount of current in a selected RF-bucket of the storage ring, which permits in turn to construct many different FP.

The first step for SBBS is to define the specific pattern. Next an algorithm compares in real time the current in each RF-bucket, read by the TCSPC, with the expected one defined by the FP. The RF-buckets are sorted so that the ones needing more current are filled as first, and the injector system automatically sets-up to fill each RF-bucket up to its corresponding current [62]. The filling finishes when the target beam current in the storage ring is reached.

### 4.2.1 *Not Standard Filling Pattern*

To verify that different FPs could be generated during the SBBS operation mode a special “ALBA” FP was tested: the FP was shaped such to spell the word “ALBA”, as presented in Fig. 4.1.

The time evolution of the SBBS injection of the “ALBA” FP is present in Fig. 4.2. Note that the filling procedure starts from the RF-buckets that are supposed to reach the highest current.

An artistic view of the consecutive FP measurements during the “ALBA” FP injection was chosen as image of the ALBA t-shirt for the 2016 Open Day (Fig. 4.3). In the front of the t-shirt the time goes from the first to the last injection, while in the back is the other way around.

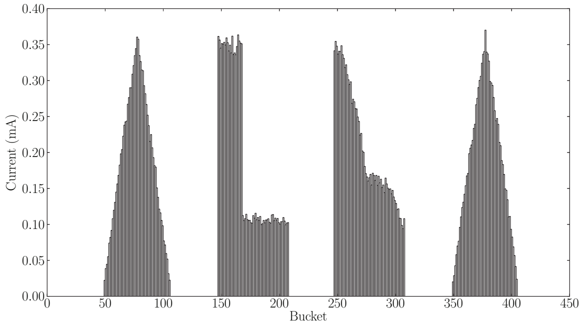

Figure 4.1: "ALBA" FP injected using the SBBS operation mode.

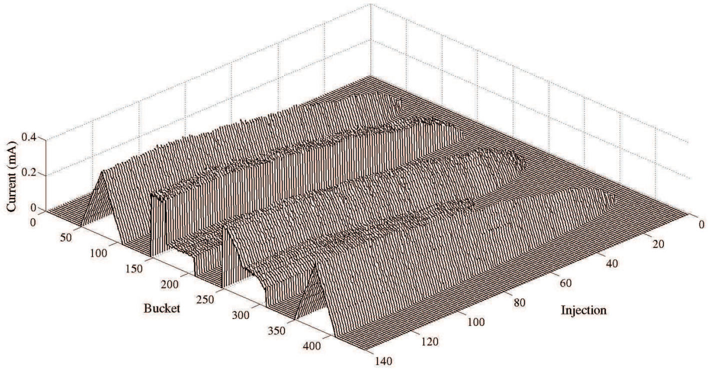

Figure 4.2: Time evolution of the "ALBA" FP injection using the SBBS operation mode.

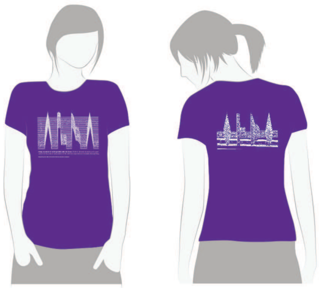

Figure 4.3: ALBA t-shirt using the TCSPC measurement of the FP, used during the 2016 Open Day.

### 4.2.2 *Selective Top-Up*

In the preliminary scheme of the ALBA top-up mode, RF-buckets are refilled every 20 minutes in order to guarantee an almost constant flux of radiation to the beamlines, and to keep the heat-load on the optical components stable. This operation mode is already active since 2014 [63]: the linac works in multi-bunch mode and the refilling is performed train by train, without any check of the current distribution in the storage ring.

An upgrade of the operation mode, consists in the SBBS selective refilling of the emptiest bunches in order to obtain a flat current distribution.As an example the results obtained by the selective refilling of an hybrid FP are presented in Fig. 4.4. The hybrid FP consists in a single train of 322 bunches and a single bunch with around 5 mA at RF-bucket 400. The selective Top-Up was applied only at the main train. The first bunches in the starting beam (black line) are not completely filled: the beam structure is not flat in general and is similar to the one usually obtained with the standard 10-trains ALBA FP. This shape is related with the characteristics of the injector system (linac, booster and transfer lines). After three hours the Top-Up refilling every 20 minutes, the 322 bunches are equally filled and the overall structure is flat, because bunches with larger initial current lose electrons faster with respect to the emptiest ones due to Touschek effect [30], for this reason the flat distribution can be achieved without exceeding the maximum nominal current in the storage ring.

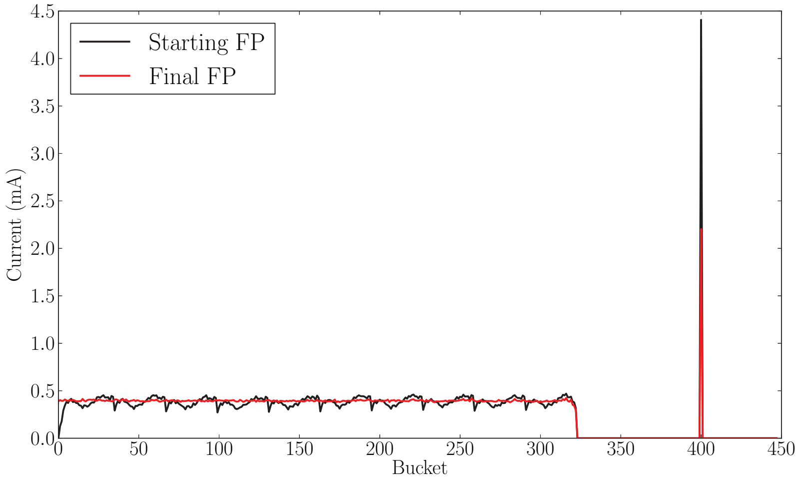

Figure 4.4: Hybrid FP composed by a 322 FP and a single bunch in RF-bucket 400. Black line represents the filling level of the bunches before the selective Top-Up, while the red line is the level after three and half hours of selective Top-Up operation.

A color-map image of the filling level of the bunches in the train as a function of consecutive data acquisitions is presented in Fig. 4.5: after several injections the electron distribution gets uniform, which is represented by a uniform color in the 2D image.

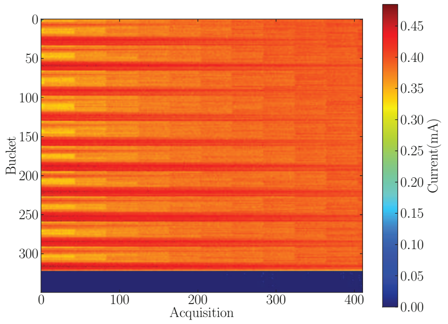

Figure 4.5: Hybrid FP evolution along consecutive acquisitions, performed every 30 s. The total acquisition time is $\simeq 3$ hours

The current in the single bunch of the hybrid FP in Fig. 4.4 was decreasing, since no Top-Up was applied to it. Measuring the current of the single bunch as a function of time, its life time can be derived. The result is presented in Fig. 4.6: black dots are the data while red line is an exponential fit, providing a decay time of 120 minutes for a single bunch with starting current of 4.5 mA.

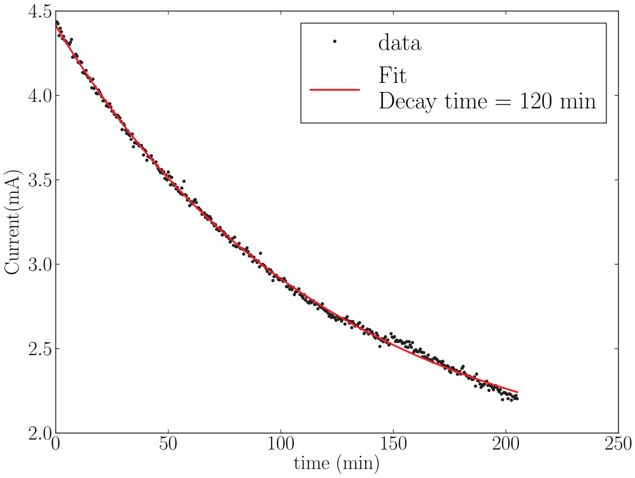

Figure 4.6: Decay time of the single bunch in the hybrid FP: black dots are the data, while the red line is the exponential fit.

One of the most common application of TCSPC is the measurement of the bunch purity, which is defined as the ratio between the number of particles in the single bunch and the ones in the neighbor RF-buckets. Purity is a crucial parameter for time resolved experiments.

Figure 4.7 shows the injection first of a high charge single bunch (up to 3.5 mA) in RF-bucket 3 (black line), surrounded by very low current bunches ($< 0.2$ mA) in RF-buckets [1-6] (red line), injected in a second moment. Before doing this, the bunch cleaning was run using the feedback system [25] to be sure that RF-buckets [1-2] and [4-6] are really empty. The injection in low current bunches is performed by manually switch on/off the linac, and adjusting the gain level to reduce the linac charge to its minimum. The measurements with the PMT (Fig. 4.7(a)) and the APD (Fig. 4.7(b)) are taken in different moments, so the RF-bucket currents are different.

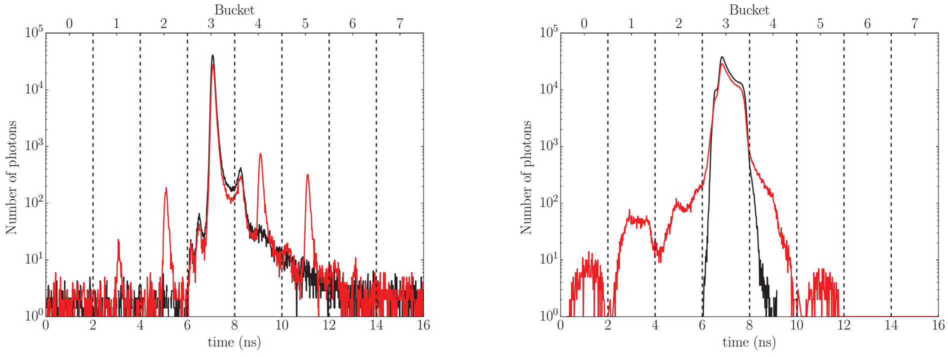

(a) *PMT*.

(b) *APD*.

Figure 4.7: Bunch purity estimation using the PMT and the APD. Black vertical dashed lines represent the time length of a RF-bucket.

The PMT measurement has a constant noise level of around 5 cps for each 16 ps bin, while the APD does not show any count at all in the empty RF-buckets. On the other hand the peak produced by the filled bunches by the PMT is much clear because is narrower than the one from the APD, due to the shorter TTS.

In both cases it is possible to distinguish bunches with less than 10 counts per bin, located around the main bunch, which had a maximum counts of around $6 \times 10^4$. This leads to a dynamic range for the TCSPC better than $10^4$ both for the PMT and the APD.

This result was obtained acquiring data for 200 seconds. Dynamic ranges of $\simeq 10^6$ are necessary to measure bunch purities of $\simeq 10^5$ (usually required for time resolved experiments). This would require longer measurements times ($\gtrsim 1$ hour), but these results looks quite optimistic toward the possibility of obtaining these values using the APD.

On the other hand, the dynamic range of PMT ($10^4$) very likely cannot be improved: focusing on the counts in RF-bucket 6 the measured peak results to be only few counts above the noise level and, therefore even increasing the integration time, the result would not change.

# 5

# SYNCHROTRON RADIATION INTERFEROMETRY IN ACCELERATORS

A widely used technique to measure beam size in light sources is the Synchrotron Radiation Interferometry (SRI), which is based on the analysis of the spatial degree of coherence of the visible part of the synchrotron radiation and has been used in accelerators since late '90s [39]. This Chapter presents the interferometry theory and how practical limitations can affect the SRI measurements. Furthermore, the upgrades performed in the ALBA experimental setup are described.

## 5.1 SYNCHROTRON RADIATION INTERFEROMETER THEORY

In most of the electron machines it is not possible to perform beam size measurements using a direct visible light imaging system because of diffraction limitations (as explained in Sec. 1.5). On the other hand the synchrotron radiation produced by the beam is quasi-coherent due the beam discrete nature: even though each electron is a source of coherent radiation, the final observable light is obtained by summing-up the radiation generated by the different particles. This means that from interference experiments the radiation spatial degree of coherence can be measured and the beam size can be inferred [36].

The setup for SRI measurements is a classical Young-like experiment [64]. It is composed by a double aperture system, orthogonal to the direction of the radiation propagation, as presented in Fig. 5.1.

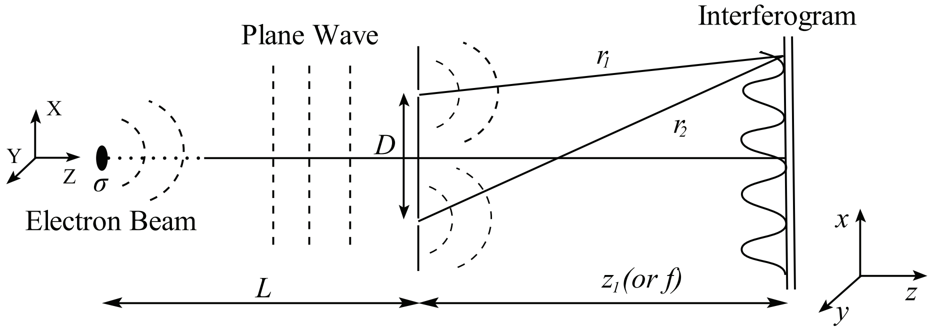

Figure 5.1: Young-like experiment sketch: the radiation is generated by the electron beam, passes through a double aperture system and produces an interference pattern in the observation plane.

Consider the coherent radiation produced by a single electron located at $(X, Y) = (0, 0)$, transversally centered with respect to the two pinholes. The distance between the electron and the double-pinhole system is $L$ and the separation between the pinholes is $D$. Consider also that the electron is moving parallel with respect to the $z$ axis e.g. zero divergence $(X', Y') = (0, 0)$. For simplicity the apertures are considered as ideal pinholes (e. g. point-like). The radiation diffracted by one pinhole interferes with the one diffracted by the other and generates an interference pattern referred to as *interferogram*.

Assuming that the double aperture system is located far from the source point ($L$ large), the radiation wave reaching the pinholes (Fig. 5.1) can be considered as a plane wave traveling on the $z$ direction described as:

$$V_S(z) = V_0 e^{ikz}, \tag{5.1}$$

where $V_0$ is the amplitude of the wave, $k$ is the wave vector $k = \frac{2\pi}{\lambda}$, and $\lambda$ is the radiation wavelength.

The radiation reaching the observation plane (at a distance $z_1$ from the pinholes) will result from the interference between two spherical waves generated by the two pinholes. Along the transverse direction $x$, the amplitude of the wave $V(x)$ is given by the superposition principle [65]:

$$V(x) = \frac{V_0}{r_1(x)} e^{ikr_1(x)} + \frac{V_0}{r_2(x)} e^{ikr_2(x)}, \tag{5.2}$$

where $r_1(x)$ and $r_2(x)$ depends on $x$, and are the distances of the two pinholes from the observation plane.

Restricting to the case of small $x$ (such that $x << z_1$), the angle describing the observation transverse position is:

$$\alpha \simeq \frac{x}{z_1}. \tag{5.3}$$

Locating the observation plane far from the double-aperture system (such that $D << z_1$), the optical path difference can be expressed as

$$r_1(x) - r_2(x) \simeq \alpha D = \frac{x}{z_1} D, \tag{5.4}$$

as shown in Fig. 5.2.

In real experiments a lens (or a system of lenses) is used to obtain the interferogram at a finite distance. For this reason, $z_1$ is often identified as the focal distance of the lens, $f$ (see Fig. 5.2).

The final parametrization of the intensity of the interferogram produced by a single electron on axis, traveling with zero divergence, $I_{s.e.}(x)$, is

$$I_{s.e.}(x) = I_0 \left\{ 1 + \cos\left( \frac{2\pi}{\lambda} \frac{x}{f} D \right) \right\}, \tag{5.5}$$

where $I_0 \propto V_0^2$, the wave vector $k$ is substituted by $\frac{2\pi}{\lambda}$, and $z_1$ by $f$.

Suppose now another electron displaced transversally $(X, Y) \neq (0, 0)$ with a zero divergence $(X', Y') = (0, 0)$, and producing similarly a second plane wave. Since the

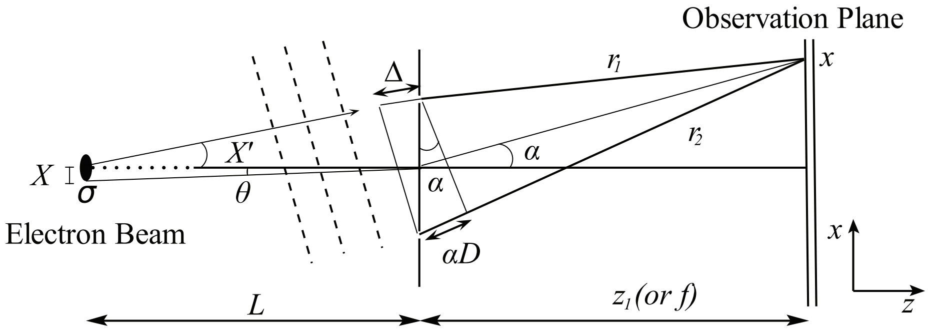

Figure 5.2: Interferometry sketch, highlighting the geometrical consideration described in the text. If the source point is transversally centered and traveling parallel to the $z$ axis the only contribution to the interferometry fringes is given by the optical path difference $\alpha D$. The transverse displacement of the source point adds a further angle $\theta$ to the optical path difference becoming $(\alpha+\theta)D$. Finally the electron beam divergence contributes with a path difference of $\Delta$, induced by an equivalent angle at the source point $\Delta/L$. The final equation for the optical path difference is $(\alpha+\theta+\Delta/L)D$.

particle is running along a different path, the optical path difference calculated in Eq. 5.4 must be corrected by adding to Eq. 5.3 a further angle $\theta$ parameterizing the displacement from a centered particle:

$$\theta = \frac{X}{L}, \tag{5.6}$$

where $X$ is the transverse coordinate of the electron and $L$ the distance between the not-displaced source and the double-pinhole center (see Fig. 5.2).

Consider now an electron with zero transverse displacement $(X, Y) = (0, 0)$ but traveling with a divergence $X'$. The plane wave generated by the electron is tilted by an additional angle due to the divergence. The extra optical path difference $\Delta$ between the light reaching the two pinholes depends on $D$ as:

$$\Delta \simeq X'D, \tag{5.7}$$

where $X'$ is considered small ($X'D << z_1$). Since $\Delta$ can be interpreted as induced by a displacement at the source point, the observation angle $\alpha$ must be corrected by a further factor $\theta'$ given by

$$\theta' = \frac{\Delta}{L} = \frac{X'D}{L}. \tag{5.8}$$

For an electron displaced transversally by a distance $X$, and traveling with a divergence $X'$, the intensity at the observation point is directly given by Eq. 5.5, by adding the contributions obtained in Eq. 5.6 and Eq. 5.8:

$$I_{s.e.}(x, X, X') = I_0(X, X') \left\{ 1 + \cos\left( \frac{2\pi}{\lambda} \left( \frac{x}{f} + \frac{X}{L} + \frac{X'D}{L} \right) D \right) \right\} \tag{5.9}$$

where $I_0(X, X')$ is the intensity of the interferogram associated with the given electron.

Equation 5.9 shows that the cosine phase is different from the one using Eq. 5.5. This introduces a shift in the resulting function, as illustrated in Fig. 5.3, where the intensity of a single electron displaced from the center at different transverse positions is shown.

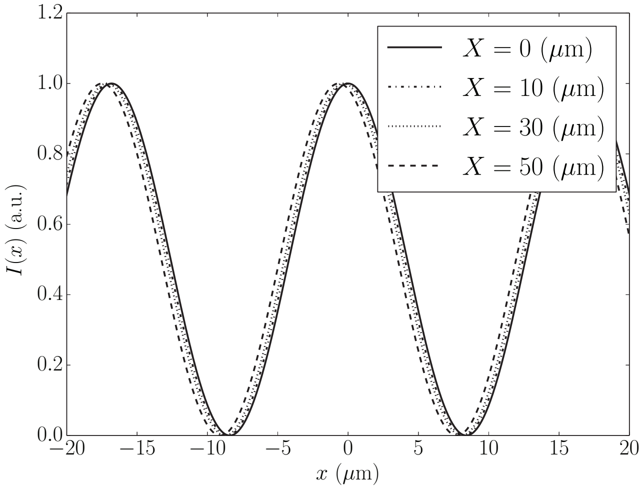

Figure 5.3: Intensity produced by a Young-like experiments for electrons transversally displaced by different offsets.

At ALBA, the beam is composed by more than $10^{12}$ electrons and each electron has a different transverse position and divergence. Interferograms produced by different electrons have a different phase, and the final intensity of the beam interferogram is:

$$I_{tot}(x) = \int_{-\infty}^{\infty} \int_{-\infty}^{\infty} I(x, X, X') dX dX', \tag{5.10}$$

where $I(x, X, X')$ is the one defined in Eq. 5.9.Expanding Eq. 5.10 one obtains:

$$\begin{aligned} I_{tot}(x) = \int_{-\infty}^{\infty} \int_{-\infty}^{\infty} I_0(X, X') dX + \ldots \\ \ldots + \int_{-\infty}^{\infty} \int_{-\infty}^{\infty} I_0(X, X') \cos\left(\frac{2\pi}{\lambda}\left(\frac{x}{f} + \frac{X}{L} + \frac{X'D}{L}\right) D\right) dX dX'. \end{aligned} \tag{5.11}$$

The second integral in Eq. 5.11 can be interpreted as the real part of a complex Fourier transformation where X and D are conjugate variables, and all the other parameters are considered as constants:

$$\mathcal{F}(I_0(X)) \propto \int_{-\infty}^{\infty} I_0(X) e^{-i\left(\frac{2\pi}{\lambda}\left(\frac{x}{f} + \frac{X}{L} + \frac{X'D}{L}\right) D\right)} dX. \tag{5.12}$$

Neglecting all the terms not depending from X and redefining $I_0$ as the total radiation intensity generated from all the electrons, one can define the *visibility function* $\gamma(D)$ as the Fourier transform of the spatial distribution of the source:

$$\gamma(D) = \frac{\int_{-\infty}^{\infty} I_0(X) e^{-i\left(\frac{2\pi}{\lambda}\frac{X}{L}D\right)} dX}{I_0}. \tag{5.13}$$

The parametrization of the intensity of interferogram produced by the beam is obtained by substituting Eq. 5.13 in Eq. 5.11:

$$I_{tot}(x, X') = I_0 \left\{ 1 + \Re\left( \gamma(D) e^{-i\left(\frac{2\pi}{\lambda}\left(\frac{x}{f}+\frac{X'D}{L}\right)D\right)} \right) \right\} \tag{5.14}$$

$$= I_0 \left\{ 1 + |\gamma(D)| \cos\left( \frac{2\pi}{\lambda}\left(\frac{x}{f} + \frac{X'D}{L}\right) D \right) \right\}. \tag{5.15}$$

The same treatment can be applied to the parameters $X'$ and D, resulting on

$$I_{tot}(x) = I_0 \left\{ 1 + |\gamma(D)||\gamma'(D)| \cos\left( \frac{2\pi}{\lambda}\frac{x}{f} D \right) \right\} \tag{5.16}$$

where $\gamma'(D)$ is the visibility function due to the divergence.

The general effect of the visibility functions is to lift-up the minima of the interferogram, as presented in Fig. 5.4, which compares the fringes for a single electron with $X = 0$ and $X' = 0$, and the ones for a beam where both the spatial and the divergence distributions are assumed to be Gaussian with a transverse width of $\sigma = 60\,\mu m$ and a divergence of $\sigma' = 100\,\mu rad$.

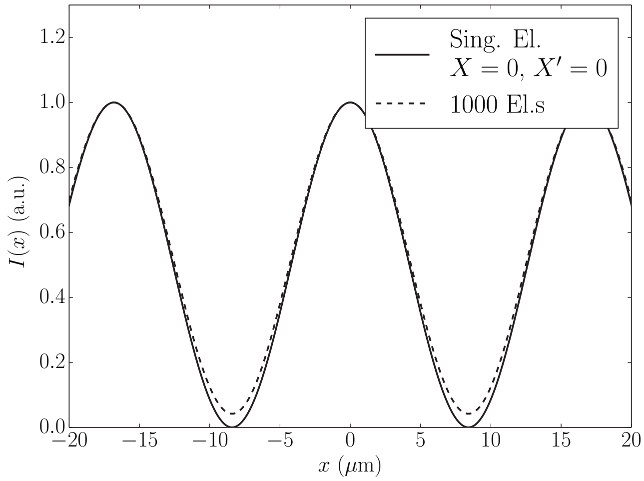

Figure 5.4: Normalized total intensity distribution for a single electron (solid line), and for 1000 electrons distributed with a transverse displacement up to 60 µm.

In this case ($\gamma(D)$ and $\gamma'(D)$ Gaussian) the visibility functions can be expressed as:

$$\gamma(D) = e^{-\frac{1}{2}\left(\frac{2\pi}{\lambda}\frac{\sigma}{L}D\right)^2}, \tag{5.17}$$

$$\gamma'(D) = e^{-\frac{1}{2}\left(\frac{2\pi}{\lambda}\frac{\sigma'}{L}D^2\right)^2}, \tag{5.18}$$

where $\sigma$ and $\sigma'$ are respectively the width of the transverse and the divergence distributions.

Table 5.1 lists the values of the parameters in Eq.s 5.17 and 5.18 for the ALBA experiment.

| | | |
|---|---|---|
| Aperture distance, $D$ | 16 mm | |
| Radiation wavelength, $\lambda$ | 538 nm | |
| Focal length, $f$ | 500 mm | |
| Distance from the source to the apertures, $L$ | 15 m | |
| | $x$ | $y$ |
| Beam size, $\sigma$ | 55 µm | 23 µm |
| Divergence, $\sigma'$ | 135 µrad | 0.3 µrad |

Table 5.1: Values of the parameters used to calculate the visibility functions (Eqs. 5.19 and 5.20), based on SRI at ALBA.

Using these parameters, the results for the visibility functions are:

$$\gamma_x(D) = 0.790981 \qquad \gamma'_x(D) = 0.999638 \tag{5.19}$$

$$\gamma_y(D) = 0.9598242 \qquad \gamma'_y(D) = 0.999999998, \tag{5.20}$$

where the subscript $x$ and $y$ refers to the horizontal and vertical directions respectively. In both cases, the effect of the divergence is much smaller with respect to the one of the beam size, and it can be neglected by approximating $\gamma'(D) \simeq 1$ in Eq. 5.16.

Up to now the apertures were considered as point-like pinholes, which is not realistic. The effect of the finite aperture shape modulates the interferogram envelope. The modulation is given by the Fraunhofer diffraction of a plane wave going through one of the two apertures, and is described by the convolution of the initial plane wave (Eq. 5.1), with the shape of the aperture $f(\xi)$, being $\xi$ the coordinate in the apertures plane [36]. The result for the observed intensity is given by:

$$I(x) = (\mathcal{F}(f(\xi)))^2 \times I_{tot}(x), \tag{5.21}$$

where the first part of the equation gives the envelope of the interferogram.

Using extended pinholes with an aperture radius $a$, the intensity distribution at the observation plane is given by [66]:

$$I_{PH}(x) = I_0 \left\{ \frac{J_1\left(\frac{2\pi a x}{\lambda f}\right)}{\left(\frac{2\pi a x}{\lambda f}\right)} \right\}^2 \times \left\{ 1 + V \cos\left(\frac{2\pi D x}{\lambda f}\right) \right\}, \tag{5.22}$$

where $V$ is called *visibility* and represents the value of the visibility function $\gamma(D)$ for a given pinholes (or slits) separation.

With slits of width $2a$, the intensity becomes [5]:

$$I_{SL}(x) = I_0 \left\{ \text{sinc}\left(\frac{2\pi a x}{\lambda f}\right) \right\}^2 \times \left\{ 1 + V \cos\left(\frac{2\pi D x}{\lambda f}\right) \right\}. \tag{5.23}$$

Figure 5.5 shows the results for the interferogram in the two different cases, were the differences between the two corresponding envelopes can be distinguished.

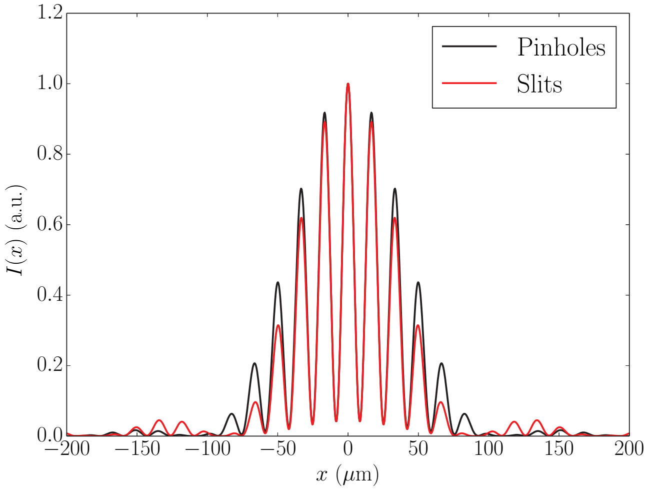

Figure 5.5: Normalized intensity projection of the interferogram using extended pinholes (in black) or rectangular slits (in red).

The visibility can be inferred by:

$$V = \frac{I_{Max} - I_{Min}}{I_{Max} + I_{Min}}, \tag{5.24}$$

with $I_{\text{Max}}$ and $I_{\text{Min}}$ denoting the maximum and its consecutive minimum intensities of the interferogram. However, to obtain a better result, one can also infer $V$ by fitting experimental results using Eq. 5.22 (when using pinholes), or Eq. 5.23 (when using slits).

The beam size is then calculated by inverting Eq. 5.17:

$$\sigma = \frac{\lambda L}{\pi D} \sqrt{\frac{1}{2} \log\left(\frac{1}{V}\right)}. \tag{5.25}$$

This technique is commonly addressed as Synchrotron Radiation Interferometry (SRI).

## 5.2 EXPERIMENTAL SETUP: ALBA DIAGNOSTIC BEAMLINE XANADU

At ALBA the setup is located in the diagnostic beamline, Xanadu. In this beamline, the light generated by a bending magnet (BM01) is guided from the Front-End 01 (FE01), described in Sec. 2.3, to the optical hutch by a set of mirrors. The first is a motorized *in-vacuum* mirror located at the end of FE01, just before the X-ray copper absorber, orientated at 45° with respect to the incident direction of the synchrotron light. A 3D model of the mirror is presented in Fig. 5.6.

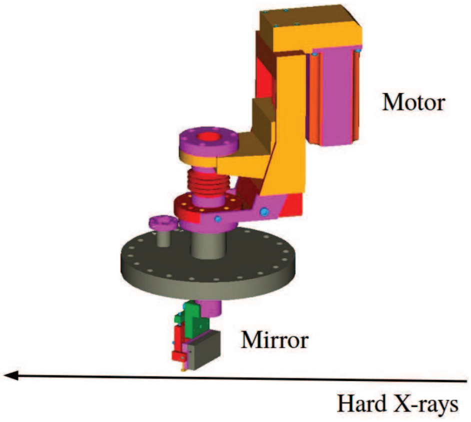

Figure 5.6: 3D model of the FE01 in-vacuum mirror.

The vertical mirror position is controlled with a motor, which allows to insert it in and out from the light fan. The mirror can be inserted from 27 mm down to 5 mm above the orbit plane to avoid the interaction with the hardest X-rays component of the synchrotron radiation (see Sec. A.4). In this way only the upper lobe of the light is reflected and this is why the setup is often called as "half mirror".

The synchrotron radiation is extracted out of the vacuum chamber through an extraction window, and guided to the Xanadu optical hutch by seven *in-air* mirrors. Figure 5.7 presents a 3D model of the mirrors extraction chicane. The yellow arrow represents the optical path of the synchrotron radiation.

The first two in-air mirrors are located inside the tunnel and bring the light to the Xanadu optical hutch. Once the light crosses the shielding wall, two mirrors bring it further down inside a lead cabinet, which was designed for radiation protection. Almost at the ground level, the light crosses a hole in the cabinet, and finally three more mirrors transport the light to the optical table: the first brings the light up to the table level, and the last two are used to rotate the wavefront by 90°, in order to keep the proper horizontal and vertical orientation.

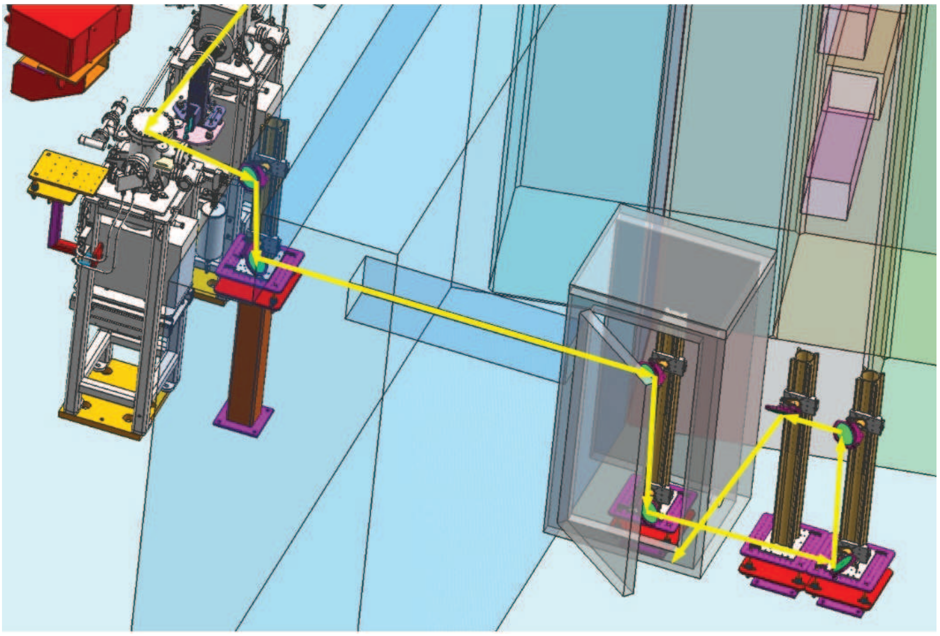

Figure 5.7: 3D model of Xanadu mirrors chicane. The yellow arrow represents the light optical path.

Since the Xanadu beamline was not originally designed for SRI measurements, first attempts were limited by practical constrains which strongly affect the results. The main problems were related with the quality of the optical elements, and the vibration in the optical path [67].

## 5.3 PRACTICAL LIMITATIONS OF SRI: QUALITY OF THE OPTICAL ELEMENTS

One of the key parameters to perform SRI is the surface *flatness* [68], which is defined as the difference between the optical element surface and its ideal surface, measured in fractions of the test wavelength, $\lambda$.

If the flatness of the optical elements is poor, the wavefront reaching the double aperture system is deformed. A simplified and illustrative mirror deformation induced by a flatness $\frac{\lambda}{N}$ is sketched in Fig. 5.8. The mirror is oriented at 45°with respect to the light direction. Due to the deformation, the original light ray passing through the left-most aperture is deviated by an angle $\Delta\Phi$, which can be approximated by:

$$\Delta\Phi \simeq \frac{\sqrt{2}\lambda}{Nd}, \tag{5.26}$$

where d is the mirror length in which the radiation is reflected and covers the separation between the apertures D. At the double-aperture plane, this light ray is displaced by a distance $\Delta D$:

$$\Delta D = L_{Ap}\Delta\Phi, \tag{5.27}$$

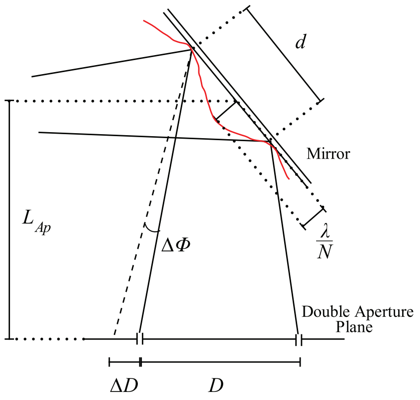

Figure 5.8: Sketch of the effect of surface deformation in a mirror. The black solid line represent the wavefront selected by the apertures separated by a distance D if the mirror is completely flat, while the dashed black lines represent the wavefront path if the mirror is deformed (red line).

where $L_{Ap}$ is the distance between the mirror and the double aperture plane. This is to say that the angular deviation (produced by a poor surface flatness) is equivalent to an apparent change in the distance between the two apertures, so that D must be substituted with $D + \Delta D$ in Eq. 5.5, which introduces a variation in the interferogram fringes period.

Figure 5.9 shows the interference fringes produced by the mirrors with different surface flatness: for flatness in the order of $\frac{\lambda}{3}$ or better the interferogram fringe period does not change significantly, while for flatness worst than $\frac{\lambda}{1}$ this period gradually increases with a consequent effective deformation in the interference pattern.

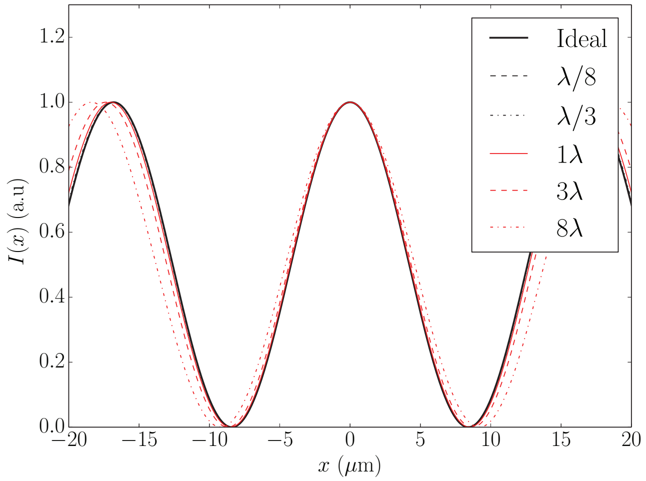

Figure 5.9: Interference fringes for different flatness.

The initial Xanadu in-vacuum mirror was designed with a flatness requirement of $\frac{\lambda}{2}$, and no flatness constrains were required for the extraction window. The other mirrors of the chicane were 2″ Thorlabs "Economy Front Surface Mirrors" [69], with a flatness of 5$\lambda$. Moreover a diameter of 2″ was not sufficient to transport all the radiation wavefront, so the footprint edges seen at the optical table were cut.

The Xanadu beamline was completely upgraded by substituting all the mirrors (either in-air or in-vacuum) and the extraction window with new ones of better optical quality:

- In-air mirrors composing were substituted with 4″ $\frac{\lambda}{10}$ Broadband Dielectric Mirrors by Thorlabs [70].
- New extraction window was substituted with a Torr Scientifc CF63 Bonded Fused Silica Viewport, with a flatness of $\frac{\lambda}{10}$, and a parallelism of 5 arc sec [71].

The new in-vacuum mirror, manufactured by Thales-SESO [72], is customized to ensure the compatibility with the mechanical requirements of the front-end and withstand the bake-out conditions. It is made out of copper with a kanigen nickel coating to protect the Cu from oxidation. Its size is 5 mm larger in the vertical direction with respect to the old mirror in order to allow a deeper insertion in the synchrotron radiation fan, so to extract more light if necessary.

The flatness of the mirror was measured at the ALBA optics laboratory [73] using a Fizeau interferometer [74]. A comparison between the results of the Fizeau measurements for the new and the old in-vacuum mirror is presented in Fig. 5.10.

The results provided a peak-to-valley flatness of the new in-vacuum mirror of $\frac{\lambda}{7}$, improving up to $\frac{\lambda}{8}$ ($x = [20-40]$ mm in Fig. 5.10(a))) in the zone of interest for the synchrotron radiation. The old mirror shows a flatness of $\frac{\lambda}{1}$, but there are some radiated zones where the flatness is not measurable, due to a unexpected nano-crystalline growth of Carbon-Like-Diamond on the surface (for more details see Appendix C [75]).

A picture of the final footprint of the radiation reaching the Xanadu optical table is presented in Fig. 5.11(b), compared with the footprint before the Xanadu upgrade (Fig. 5.11(a)).

Thanks to the larger mirror all the radiation can be collected, and the footprint is not cut. Moreover the darker vertical stripes present in Fig. 5.11(a) disappeared: these stripes were probably related to the nano-crystalline growth on the surface of the old mirror. The well defined horizontal and vertical stripes are due to diffraction, and the net cut on the upper part of the fan indicates that the footprint is upside-down.

Once the new in-vacuum mirror is installed, it needs some time to condition before its final use. Figure 5.12 shows how the new mirror reacts after the first insertion in the synchrotron fan. Three thermocouples are installed at the mirror bottom to avoid overheating. The thermocouples response (blue, green and pink curves) rises up to 27°, as well as the pressure inside FE01 (light blue curve), which gets stable later on. The temperature of the copper absorber at the end of FE01 is shown in red. A clear process of out-gassing is observed during 5 hours.

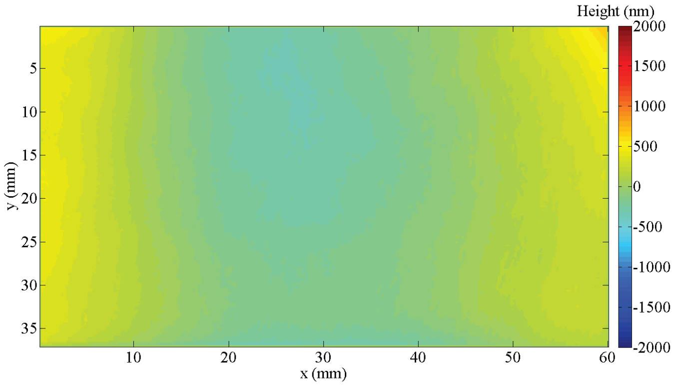

(a) *New*.

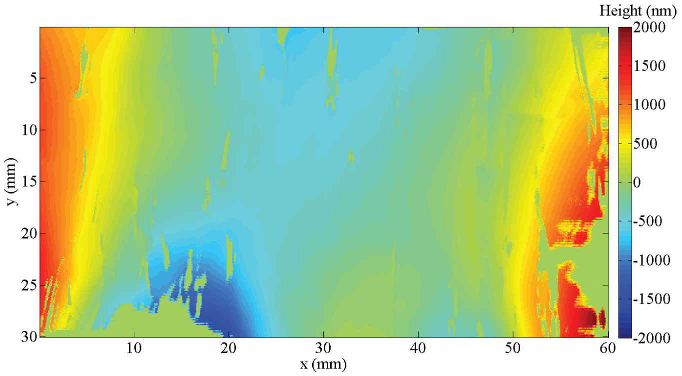

(b) *Old*.

Figure 5.10: Flatness measurements of the new and the old in-vacuum mirrors using the Fizeau Interferometer.

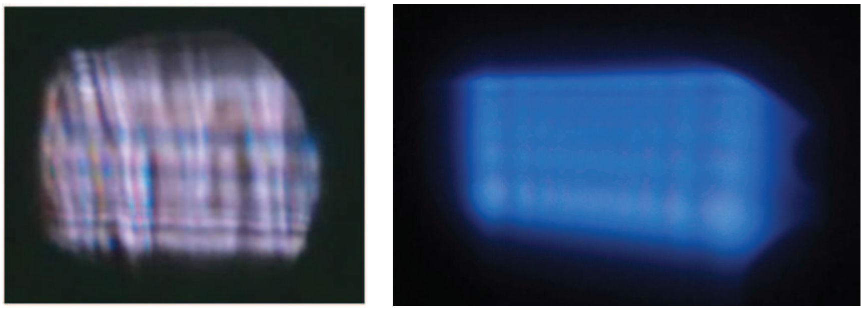

(a) *Before the upgrade*.

(b) *After the upgrade*.

Figure 5.11: Footprint of the synchrotron radiation at the Xanadu optical hutch before and after the beamline upgrade.

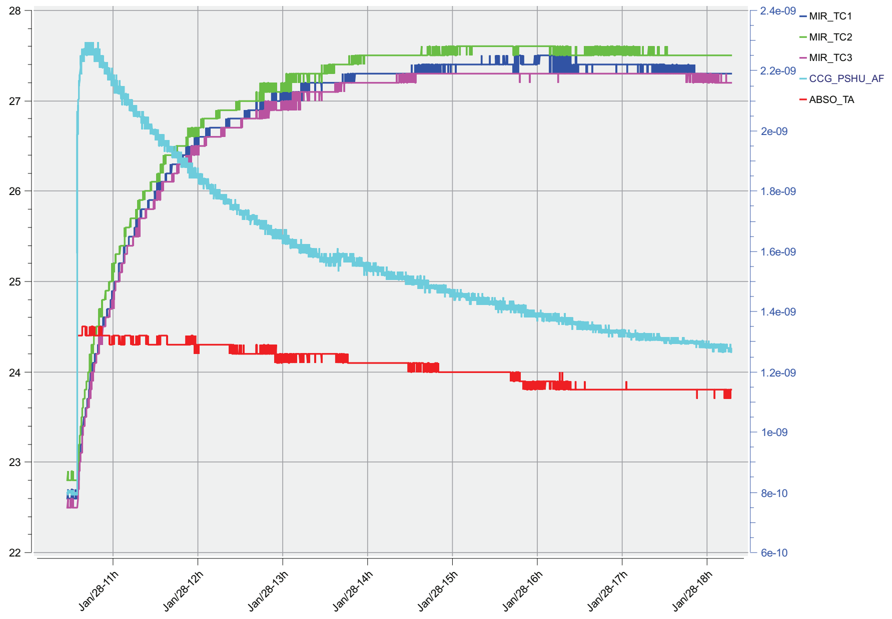

Figure 5.12: Measurements of the temperature of the mirror and the copper absorber, and pressure inside FE01 at the first mirror insertion in the synchrotron radiation fan, as a function of time.

### 5.3.1 *Non-Invasive Mirror Status Monitoring System*

Once the whole beamline is upgraded, a non-invasive way to monitor the status of the optical components during normal operations was developed. The device uses a *Hartmann Mask* [76] to obtain on-line and in-situ qualitative information about the in-vacuum mirror flatness.

The setup is mounted as close as possible to the extraction window and a motor allows to insert and extract the mask when needed without entering the tunnel, as shown in Fig. 5.13.

The Hartmann Mask consists in a 10×10 grid of holes with 1 mm diameter and spaced by 5 mm. The mask converts the incident wavefront in light wavelets. Comparing the position and the intensity of each wavelet with respect to their ideal position, the shape of the wavefront is reconstructed and the optical flatness is estimated. Figure 5.14 presents a sketch of the Hartmann Mask working principle, similarly to what is shown in Fig. 5.8.

Images are acquired at the optical table in the Xanadu optical hutch. Once the mask covers the light fan, the radiation is imaged over a semitransparent plastic plate. A CCD, together with a objective system to focus the camera on the plastic plate, is used to acquire the images. The dimensions in the images are calibrated using a unit reference on the plastic plate.

Figure 5.13: Motorized Hartmann Mask mounted close to the extraction window of FE01.

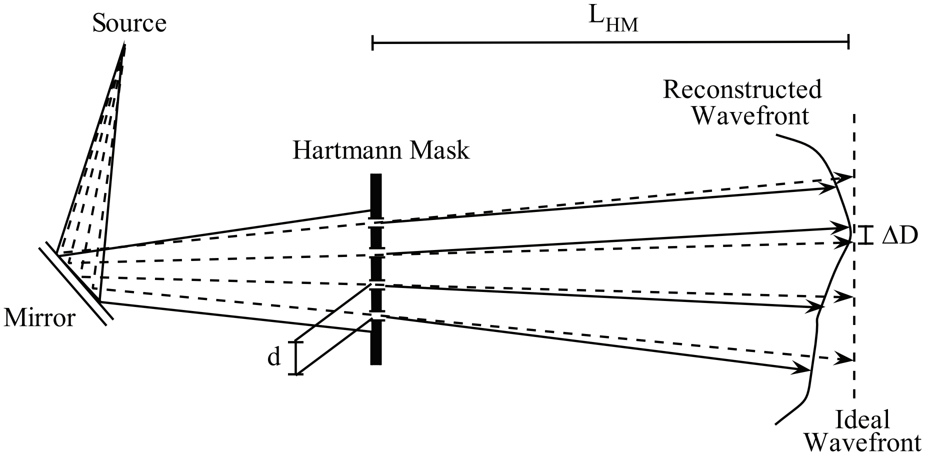

Figure 5.14: Hartmann Mask working principle, converting the wavefront into light wavelets. The dashed lines are the ideal trajectories of the wavelets, while the solid lines are the trajectories of the wavelets after the deviation due to the mirror deformations.

An example of data used to reconstruct the waveform is shown in Fig. 5.15. Images are cut, rotated (if needed), and filtered with a low pass filter. The Hartmann Mask structure expected at the observation point is overlapped to the image, as presented by black dots in Fig. 5.15, while the red dots represent the measured position of the light wavelet centroids, calculated using bi-dimensional Gaussian fits.

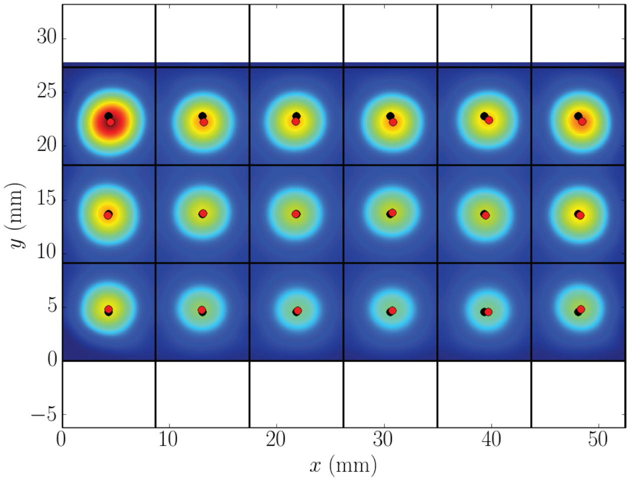

Figure 5.15: Data after the cut, the rotation and the low pass filter. Black vertical and horizontal lines are the grid, black dots are the ideal position of the centroid of the light ray. Red dots represent the measured centroid of the light rays.

The mirror flatness is estimated by looking at the displacement of the centroid with respect to the expected wavelets position.

Similar to the surface flatness effects described in Fig. 5.8 and Eq. 5.26, the angular deviation due to the optical path deformation is

$$\Delta\Phi = \frac{\Delta D}{L_{HM}}, \tag{5.28}$$

where $L_{HM}$ is the distance between the Hartmann Mask and the image plane and $\Delta D$ is the difference between the ideal and the wavelet centers.

From Eq. 5.26, the fraction of $\lambda$, defining the flatness of the optical path is finally evaluated as

$$N = \frac{\sqrt{2}\lambda L_{HM}}{d\Delta}, \tag{5.29}$$

where $\lambda$ was fixed to 540 nm since measurements are performed using white light, and $d = 5\,\text{mm}$ is the distance between the Hartmann Mask holes.

The wavefront shape is inferred by taking the measured centroids weighting them according to their intensity. In Fig. 5.16 is reported the flatness evaluation as deduced by Fig. 5.14.The estimated flatness results in this case $\frac{\lambda}{5}$, which is comparable with the $\frac{\lambda}{8}$ measured with the more precise Fizeau Interferometer. It should be stressed that the Hartmann Mask is a technique devoted to monitor the relative change of the mirror flatness over time, rather than a precise measurement on itself.

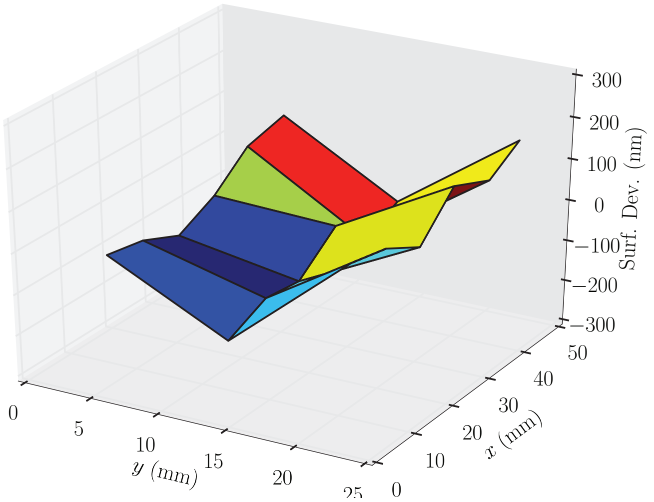

Figure 5.16: Wavefront reconstructed using the Hartmann Mask. On the $z$ axis the deviation with respect a plane wave.

Using the Hartmann Mask setup, it is possible to study the evolution of the flatness during operations, as the ones due to heating processes after inserting the mirror in the synchrotron radiation fan.

For example, Fig. 5.17 shows how the mirror heats up from 23°C (fully-out position), up to 31°C (fully-in position) during 5 hours with a beam current of 130 mA, with the machine in Top-Up mode. Flatness measurements using the Hartmann Mask are taken during this time until the temperature is stabilized.

When inserting the in-vacuum mirror, first the lower part of the optical element is heated by the radiation. This part undergoes to a temperature shock and deforms, leading to a deterioration of the mirror quality. After one hour all the thermal gradients in the mirror disappears and the original flatness is restored.

According to Eq.s 5.26 and 5.27, it is possible to calculate $\Delta D$, which is the variation of the distance of the two apertures as seen by the SRI, with respect to the nominal one D. Figure 5.18 shows the result for $\Delta D$: $\frac{\Delta D}{D}$ is in the order of 1% and according to the beam size calculation in Eq. 5.25, this leads to a change in the measured $\sigma$ of hundredth of nm, which can be neglected since the expected smallest beam size at Xanadu location is $\sigma_y \simeq 15\,\mu\text{m}$. However, this discrepancy is taken into consideration when fitting the interferogram to obtain the beam size, by leaving D as a free parameter in the fit.

## 5.4 LIMITATIONS OF SRI: VIBRATIONS OF THE OPTICAL COMPONENTS

Another limitation for the SRI beam size measurements is the variation of the optical path induced by vibrations in the optical components. This effect induces a shift in the

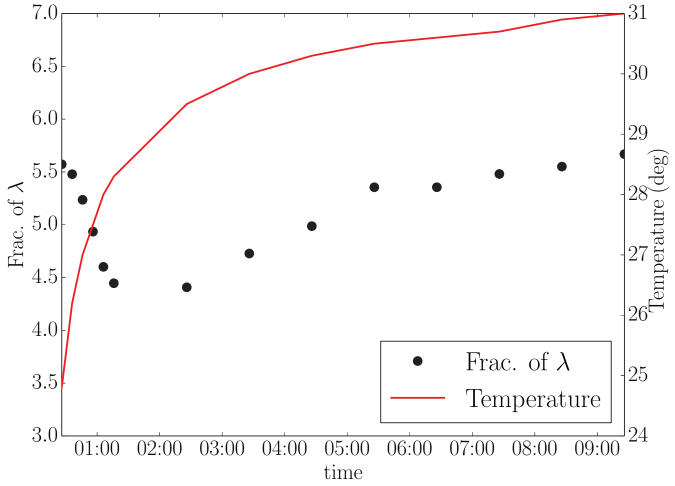

Figure 5.17: Temperature of the in-vacuum mirror and flatness of the optical path as a function of time.

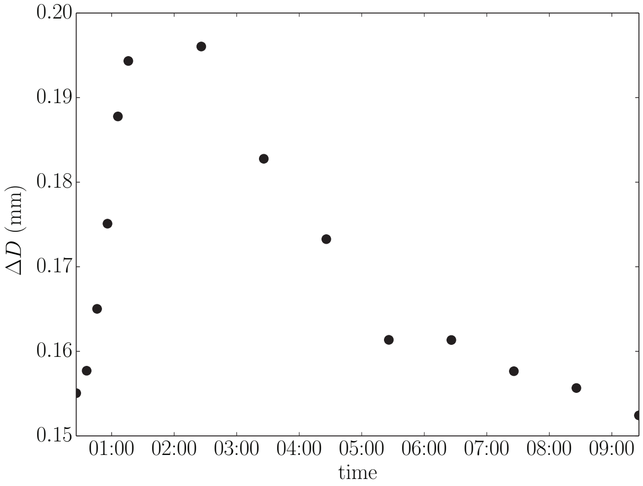

Figure 5.18: Variation of the distance of the two apertures as a function of time, due to the mirror heat-up.

fringe path described by Eq. 5.9, resulting in a modification of the visibility function used to compute the beam size.

The position at which the interferogram is formed, q, is given by the standard lens equation:

$$\frac{1}{q} = \frac{1}{f} - \frac{1}{L}. \tag{5.30}$$

If the optical path L varies, also q should varie, or else the final interferogram is blurred. This effect is specially enhanced if magnification elements are used and it can detrimentally affect the measurements.

In SRI, optical magnification is needed to spread the fringes between several CCD sensor pixels so to ease the fitting process. The most common optical components used for interferogram magnification are eyepieces.The magnification, for an eyepiece with focal length $f_o$, used jointly with a lens of focal length $f$, is given by:

$$M = \frac{f}{f_o}. \tag{5.31}$$

To justify the request of magnification one can refer to Fig. 5.4: the period of the fringes is about 10 µm, while typical pixel size in standard CCD camera is 4 µm.

In general, even a very small vibration will result in a displacement of the final image that could cover more than one pixel when using a magnification. As an example, suppose to use an eyepiece with a focal length of 18 mm. According to Eq. 5.31, the total magnification of the optical system is $M \simeq 28$. If the image is transversally displaced by 0.5 µm, the images on the CCD will be displaced of 14 µm, corresponding with 3.5 pixels. If the vibration period is smaller than the CCD exposure time, the displaced interferograms are summed up incoherently and the maximum/minimum positions spread over several CCD pixels distorting the final image.

This is the case of the Xanadu beamline: since all the mirrors of the optical path are in-air, mechanical vibrations affect the SRI measurements. This kind of vibrations are mainly due to "air-turbulences" produced by the temperature gradient between the tunnel (kept at $23 \pm 0.1$°C) and the Xanadu hutch (without temperature control).

A possible solution (not in the scope of the thesis for budgetary reason) could be to enclose all the optical path and substitute the existing stainless steel pillars by more stable granitic supports, possibly isolated from the ground floor. Another (easier) solution is to reduce the exposure time of the CCD, in order to make it lower than the vibrations period.

### 5.4.1 *Vibration Measurements*

A first way to measure mechanical vibrations of the mirrors holders is to use accelerometers (in collaboration with the Alignment Group); while a second one (in collaboration with the Metrology Group) is the use of a Position Sensor Detector (PSD) to evaluate the position variation of the light fan.

In the first case, accelerometers (Brüel and Kjael, TYPE 8344 [77]) are mounted on the pillars and on the optical table where mirrors and SRI setup are positioned, so to measure the amplitude of their displacement as a function of the frequency. Several positions were chosen for the tests, and the results show that the most influencing components are the pillar holding the mirrors, in particular the one inside the tunnel. Figure 5.19 shows the accelerometers results for this pillar: two frequency regions with high peaks at 20 Hz and 70 Hz are evident. The first peak is probably related with ground floor vibration, while the second is most likely due to air turbulences [78].

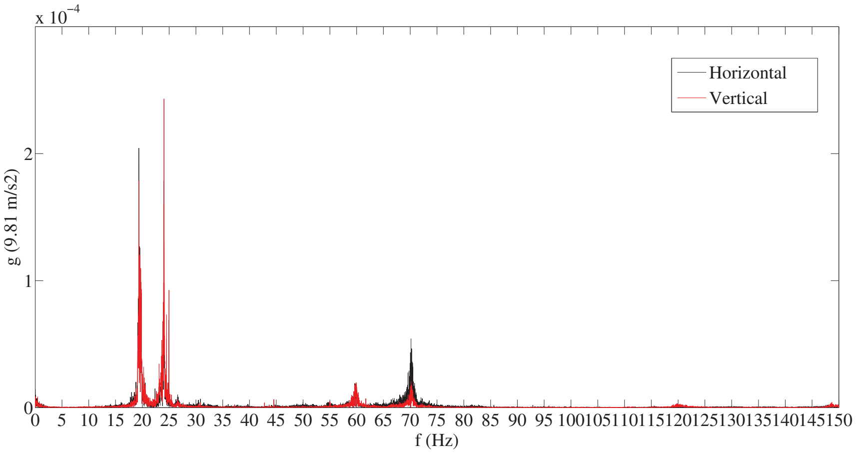

Figure 5.19: Frequency spectrum of the pillar inside the tunnel, measured with accelerometers.

In the second case a PSD is used to measure the displacement of the light fan as a function of the frequency up to 15 kHz. The sensor is a PSD90A by Thorlabs [79], and it is installed on the optical table. It works as a Beam Position Monitor, providing the horizontal and the vertical position of the light fan on the sensor, with a resolution of 4 µm.

Two different tests (with and without the eyepiece) are performed. Figure 5.20 shows the integrated motion spectrum for both the horizontal and vertical planes, with and without the eyepiece (respectively in red and black). The eyepiece magnifies the vibrations amplitude by about a factor 6. This effect is in general more evident in the vertical plane, due to the beamline mechanical structure.

As explained before, a way to reduce the effects of mechanical vibrations is to reduce the exposure time of the CCD. Using, for example, an exposure time 1 ms means not to consider displacements at frequencies below 1 kHz, such as the 20 Hz peak of mechanical vibrations and the 100 Hz present in the vertical direction.

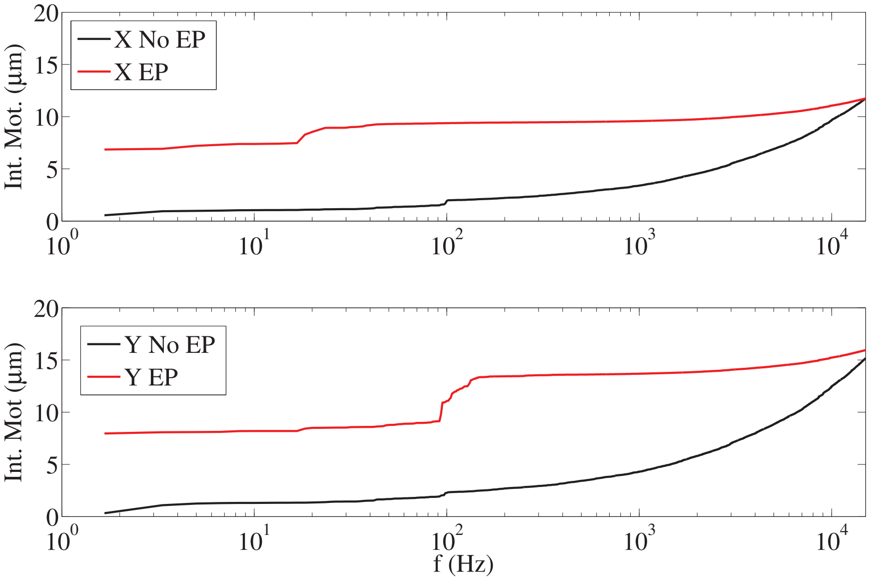

Figure 5.20: Integrated motions of the vibrations measured at the observation plane in the Xanadu optical table. In the top plot the horizontal vibrations are represented while the bottom plot shows vertical vibrations. Red data are taken with the eyepiece (EP), while black data without (No Ep).

# 6

# SYNCHROTRON RADIATION INTERFEROMETRY AT ALBA

To verify the possibility of measuring the beam size using Synchrotron Radiation Interferometry (SRI) in the Xanadu diagnostic beamline at ALBA, simulations based on Synchrotron Radiation Workshop (SRW) [6] were performed. SRW is a computer simulation code to generate synchrotron radiation from different magnetic structures and to model its propagation along the optical components of a beamline.The radiation generation, the propagation line and the interferometer setup were modeled for the Xanadu beamline. It was chosen to simulate vertical SRI measurements since they are the most critical, being $\sigma_y$ less than half of $\sigma_x$ (see Table 6.1).

First measurements and the fitting algorithm are also shown.

## 6.1 FEASIBILITY STUDIES USING SRW CODE

Figure 6.1 shows a sketch of the elements included in th SRW simulations. In order to speed-up the simulations, not all the elements of Xanadu beamline (shown in Fig. 5.7) are introduced in the SRW code. Ideally the in-air mirrors and extraction window do not affect the wavefront and are omitted in the simulations. Instead, the photon shutter and (in-vacuum) extraction mirror cut the light wavefront and cannot be omitted, as well as the double-aperture system (slits or pinholes) and the focusing lens.

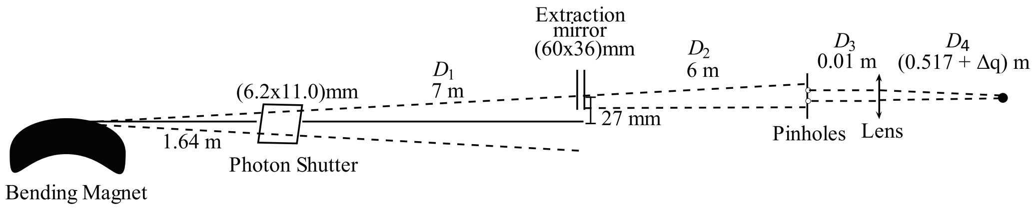

Figure 6.1: Sketch of the distribution of the elements in the simulation.

### 6.1.1 *Simulations structure*

In the simulation procedure a “mixture” of Python and SRW was used. The different parts of the simulations were integrated using Bash scripts.

Simulation is divided in 4 sub-routines:

- Electron beam phase space generation (Python);
- Wavefront generation (SRW);

|  | $x$ | $y$ |
|---|---|---|
| $\beta$-function, $\beta$ (m) | 0.249 | 24.741 |
| Emittance, $\varepsilon$ (nm rad) | 4.6 | 0.023 |
| Coupling, $\mathcal{K}$ (%) | 0.5 |  |
| Dispersion, $\mathcal{D}$ (m) | 0.04 | 0 |
| Energy Spread, $\frac{\Delta E}{E}$ | 0.00105 |  |
| Divergence, $\sigma'$ (μrad) | 136 | 0.37 |
| Beam Size, $\sigma$ (μm) | 54 | 23 |

Table 6.1: Machine parameters to compute the beam size and the horizontal and vertical beam sizes at the Xanadu source point.

- Wavefront propagation (SRW);
- Data analysis (Python).

*Electron Beam Phase Space Generation*

The scope of this routine is to generate the four dimensional transverse phase space ellipse $(x, x', y, y')$ for each particle of the beam at the Xanadu source point. The input parameters to compute the beam size at the source point are listed in Table 6.1. The equation used to calculate the beam size in the horizontal ($x$) and vertical ($y$) directions are:

$$\sigma_x = \sqrt{\beta_x \varepsilon_x + \left(\mathcal{D}_x \frac{\Delta E}{E}\right)^2}, \tag{6.1}$$

$$\sigma_y = \sqrt{\beta_y \varepsilon_y}, \tag{6.2}$$

$$\mathcal{K} = \frac{\varepsilon_y}{\varepsilon_x} \tag{6.3}$$

where $\beta_x$ and $\beta_y$ are the horizontal and vertical $\beta$-functions at the source point, $\varepsilon_x$ and $\varepsilon_y$ are the machine emittances, $\mathcal{D}_x$ is the horizontal dispersion, $\frac{\Delta E}{E}$ is the energy spread and $\mathcal{K}$ is the machine coupling (see Appendix A.3).

The output of the phase space generation is a text file containing the phase space coordinates for each electron, assuming a Gaussian distribution for each variable. Plots of the horizontal and vertical phase space for 10000 electrons, and their projections are shown in Fig. 6.2.

*Wavefront Generation*

The generation and propagation of the synchrotron radiation is performed using the special Python library `srwlib` [80].

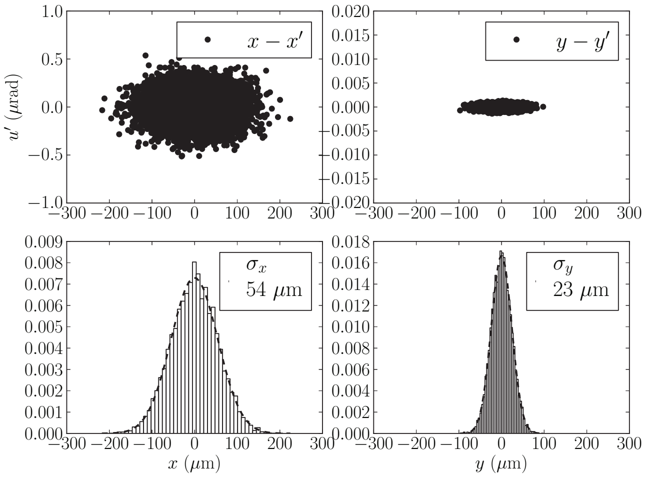

Figure 6.2: Horizontal and vertical phase spaces (top) and its projections (bottom) for the horizontal and vertical plane.

SRW code creates structures defining both the electron beam and the different elements in the simulation (i.e. magnets and optical components). Table 6.2 lists the required simulation elements with their main parameters.

Xanadu synchrotron radiation is produced by a bending magnet of 1.42 T and the source point is 7 mm downstream from the dipole center (see Fig. 6.1).

When an electron passes through the dipole, it generates the initial synchrotron radiation wavefront at the electron transverse coordinate. However, since SRW is not able to properly generate the effect of an extended electron beam on the wavefront, the radiation coming from each single electron is generated individually. The final wavefront (WFR) is given by the sum of all the single wavefronts from each electrons ($WFR_{s.e.}$) of the beam:

$$WFR = \sum_{x,y,x',y'} WFR_{s.e.}. \tag{6.4}$$

The operation is physically meaningful since the radiation produced by different electrons is incoherent.

Figure 6.3(a) shows the radiation at the photon shutter generated by a single electron, while Figure 6.3(b) presents the sum of the wavefronts generated by 1000 electrons, distributed according to the simulated beam phase space. Figure 6.3(a) shows a flat distribution of the intensity in the horizontal direction, while Figure 6.3(b) results from the convolution between the wavefront generated by a single electron and the shape of the whole beam (which has a 2D Gaussian distribution).

| Magnet | |
|---|---|
| Magnetic field | 1.42 T |
| Magnet length | 1.2 m |
| **Photon Shutter** | |
| Longitudinal Distance | 1.64 m |
| Horizontal width | 6.2 mm |
| Vertical width | 11 mm |
| **Extraction Mirror** | |
| Vertical offset | 27 mm |
| Horizontal width | 60 mm |
| Vertical width | 36 mm |
| **Lens** | |
| Focal length | 500 mm |
| Center Position | 27 mm |
| **Pinholes** | |
| Diameter | 3 mm |
| Center Position Top | 32 mm |
| Center Position Bottom | 16 mm |
| **Slits** | |
| Width | 1 mm |
| Length | 20 mm |
| Center Position Top | 32 mm |
| Center Position Bottom | 16 mm |
| **Drift Spaces** | |
| $D_1$ | 7 m |
| $D_2$ | 6 m |
| $D_3$ | 0.01 m |
| $D_4$ | $(0.517 + \Delta q)$ m |

Table 6.2: Main SRW simulation parameters. The value $\Delta q$ of the drift space $D_4$ is let as a free parameter and will be fixed in Sec. 6.1.2.

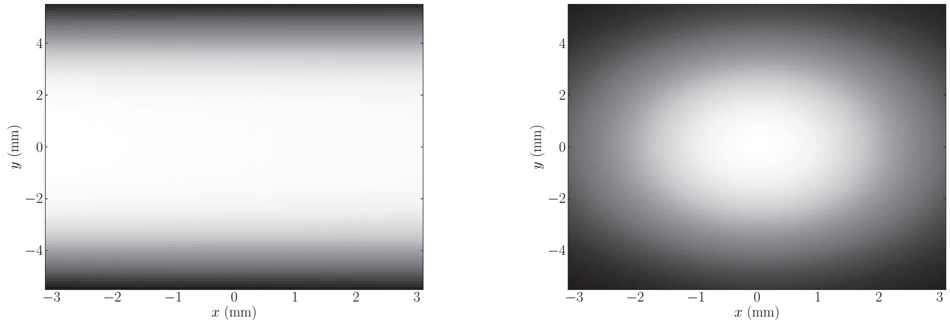

(a) Single electron centered (b) 1000 electrons beam distribution

Figure 6.3: Wavefront at the photon shutter position.

### *Wavefront Propagation*

Once the total wavefront is generated, it is propagated along the beamline to produce the interferogram. The only mirror introduced in the simulation is the in-vacuum mirror since it selects the upper lobe of the radiation and introduces diffraction when the wavefront is cut by the mirror edges. The mirror is also assumed to be perfect and is defined for simplicity as a rectangular aperture (see Fig.6.1).

Each optical element and drift space is represented by a SRW structure. Structures can be joined in "containers", which are listed in Table 6.2 and are described next:

- `optBL`: it defines the optical path from the photon shutter to the double aperture system. It includes:
  - the drift space to the Xanadu in-vacuum mirror ($D_1$);
  - the in-vacuum mirror, consisting on a rectangular aperture $60 \times 36\,\text{mm}$ centered 27 mm above the beam orbit;
  - the drift from the mirror to the table ($D_2$).
- `optAp`: it defines the double aperture system. Both the cases of extended pinholes or slits are simulated
- `optLens`: it defines the optical path from the apertures to the lens and contains:
  - the drift from the pinholes to the lens ($D_3$);
  - a lens with an horizontal and vertical focal distance `f`.
- `optAtFoc`: it defines the optical path from the lens to the focal point and contains the drift space ($D_4$). The total drift space is left as a variable parameter by adding $\Delta q$ to compensate possible misalignments with respect to the radiation fan (recall Eq. 5.30).

The simulation parameters used in this process are summarized in Table 6.2.

As an example, the wavefront before the double aperture system is shown in Fig. 6.4. The result is strongly affected by diffraction produced by the in-vacuum mirror, identified as black horizontal and vertical lines . The result compares well with the real footprint observed in Xanadu presented in Fig. 5.11 in Chap. 5.

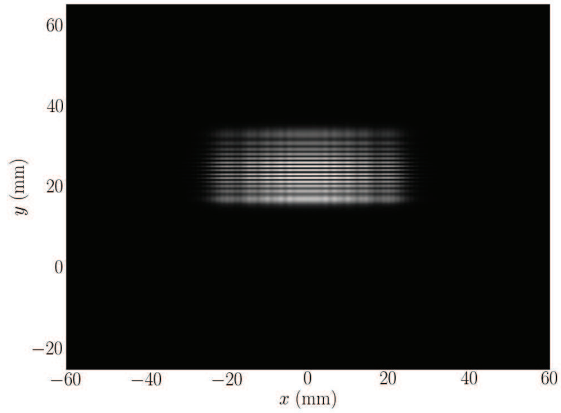

Figure 6.4: Wavefront before the double aperture location: the footprint is affected by diffraction pattern produced by the bottom and the lateral edges of the in-vacuum mirror.

The output of the simulations at the focal point is the interferogram: Figures 6.5(a) and 6.5(b) show the results for the radiation produced by 1000 electrons propagated respectively through pinholes (left) and slits (right). The main difference between the two interferograms is the envelope shape: in the pinholes case the envelope is round, while a thin stripe is obtained when using slits. The other difference is the number of fringes, which roughly depends on the ratio between the aperture width and the distance between them. The interferogram produced using pinhole has less fringes with respect to the one produced using slits.

*Data Analysis*

Simulated data are analyzed looking at the projection of the central slice in the interferogram (see for example Fig. 6.5). Projected data are normalized and fitted according to Eq. 5.22 or Eq. 5.23 respectively for pinholes or slits. The beam size is obtained in both cases using Eq. 5.25 and compared with the initial one (provided as input).

The fit quality is estimated using the $\chi^2$-parameter:

$$\chi^2 = (I_{fit} - I_{sim})^2 \tag{6.5}$$

where $I_{fit}$ is the intensity of the interferogram resulting from the fit and $I_{sim}$ is the one obtained by the simulation.

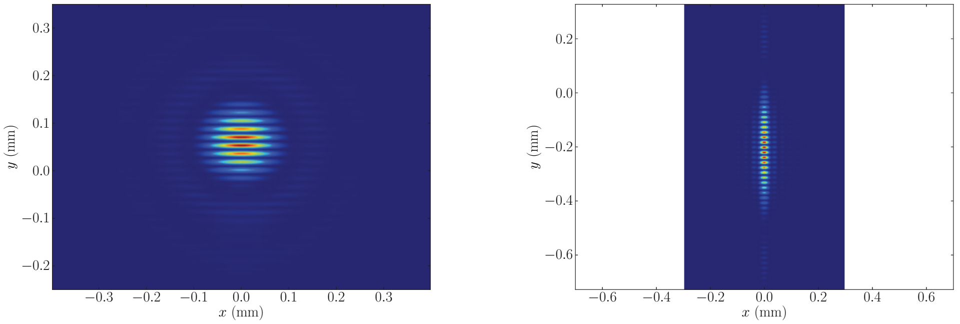

(a) Pinholes

(b) Slits

Figure 6.5: Interferogram produced by the radiation generated by 1000 electrons.

A low $\chi^2$-parameter indicates a good fit quality. On the other hand, large $\chi^2$ values should indicate some mismatch in the experiment: as an example, Figure 6.6 shows an interferogram where the observation point was intentionally displaced at an off-focus position, compared with an interferogram positioned on the right focal position: $\chi^2$ differs by more than one order of magnitude and the inferred beam size for the off-focus case (45 μm) is almost twice the input one (23 μm, recall Table 6.1).

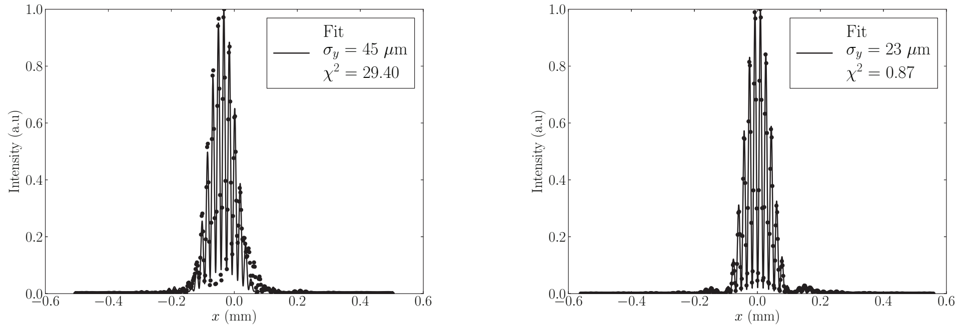

(a) Out of focus

(b) On focus

Figure 6.6: Projected data (black dots) and fit (black line) of simulated interferograms using SRW. Note that in the out-focus case the inferred beam size is about twice the input one.

### 6.1.2 *Simulation Results: Parameters Scan*

To optimize and control the reliability of the simulated experiment, the exact focal distance was found and the stability of the results was checked and the response of the SRI system at different beam sizes was studied.

When the radiation selected by the in-vacuum mirror is not centered with respect to the orbit plane, the calculation of the interferogram observation point results to be difficult.

Given a lens with a focal distance f, if the source is at a distance p, the observation point is located at a distance q given by:

$$\frac{1}{q} = \frac{1}{f} - \frac{1}{p}. \tag{6.6}$$

In order to crosscheck the Influence of the parameter q in the SRI, simulations are performed by scanning a term $\Delta q$, which is added to q and represents the correction offset to be exactly on focus. The parameter $\Delta q$ is scanned first in the $\pm 2.5$ mm range and after $\pm 0.5$ mm: both the beam size and the $\chi^2$ parameter are expected to be minimized at the correct focal distance. Results are shown in Fig. 6.7 and Fig. 6.8: using the pinholes the $\chi^2$ behavior is more consistent with the beam size trend. Moreover the beam size inferred with pinholes is closer to the input case (23 µm), with respect to the one obtained with slits.

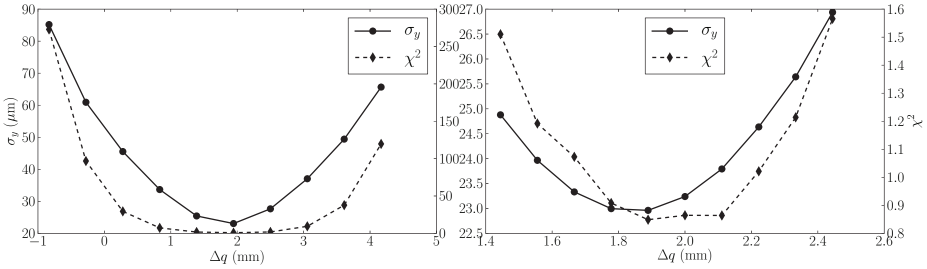

Figure 6.7: $\Delta$q scan in different range using pinholes. The dots and the solid lines represents the beam size measurements, while the diamonds and the dashed line corresponds to the $\chi^2$.

The proper $\Delta$q obtained for pinholes and slits is shown in Table 6.3: the two results are different: this is due to the different width of the two apertures, resulting in different optical paths. Note that small variations of about $\pm 0.5$ mm, corresponding with the 0.1% of the focal length ($f = 500$ mm), overestimate the inferred beam size by about 2 µm. This stresses the importance of being at the appropriate focal point.

An effective way to verify that SRI simulations (and measurements) are correct is to perform SRI measurements for different beam sizes, which in real accelerators are performed by changing the machine coupling ($\mathcal{K} = \frac{\varepsilon_y}{\varepsilon_x}$).

Several simulations are ran changing the number of beam particles ($N = 100, 1000, 10000$) and beam sizes ($\sigma_y = 23$ µm and $\sigma_y = 33$ µm) and using pinholes and slits. For a

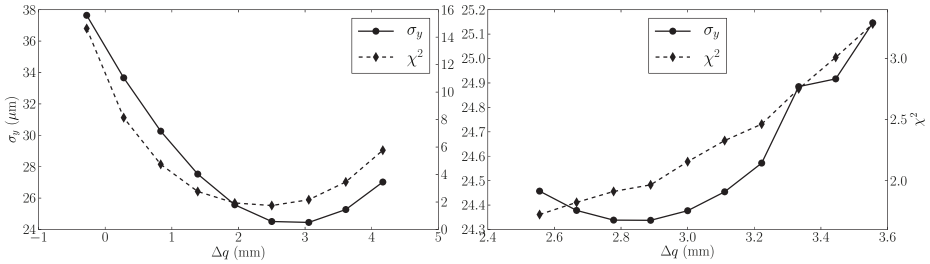

Figure 6.8: Δq scan in different range using slits. The dots and the solid lines represents the beam size measurements, while the diamonds and the dashed line corresponds to the $\chi^2$.

| | Δq (mm) |
|---|---|
| Pinholes | 1.89 |
| Slits | 2.56 |

Table 6.3: Final displacement to the focal position for pinholes and slits.

given set of parameters, 10 simulations are performed to study the fluctuations of the results. The average and the standard deviation of the beam size obtained by each set of parameters are presented in Table 6.4. These tests show, as expected, that the larger is the simulated number of particles, the better is stability result (for both pinholes and slits).

| | $\sigma_y = 23\,\mu m$ | | $\sigma_y = 33\,\mu m$ | |
|---|---|---|---|---|
| Number of particles | Pinholes | Slits | Pinholes | Slits |
| 100 | $23 \pm 1$ | $25 \pm 2$ | $32 \pm 2$ | $31 \pm 1$ |
| 1000 | $23 \pm 1$ | $24 \pm 1$ | $33 \pm 1$ | $32 \pm 2$ |
| 10000 | $23.4 \pm 0.3$ | $24 \pm 1$ | $33 \pm 0.1$ | $34.2 \pm 0.4$ |

Table 6.4: Machine parameters to compute the beam size and the horizontal and vertical results at the Xanadu source point.

For both the beam sizes, measurements are sufficiently stable from 1000 particles. This number of simulated particles is found to be the optimum compromise between performance and CPU time consumption.

The comparison of the $\chi^2$ obtained for each of the 10 wavefront generated with 1000 particles for both pinholes and slits and the two different beam sizes is presented in

Fig. 6.9(a): the results obtained with pinhole is more stable and provides always a better fit quality with respect to the one obtained simulating slits.

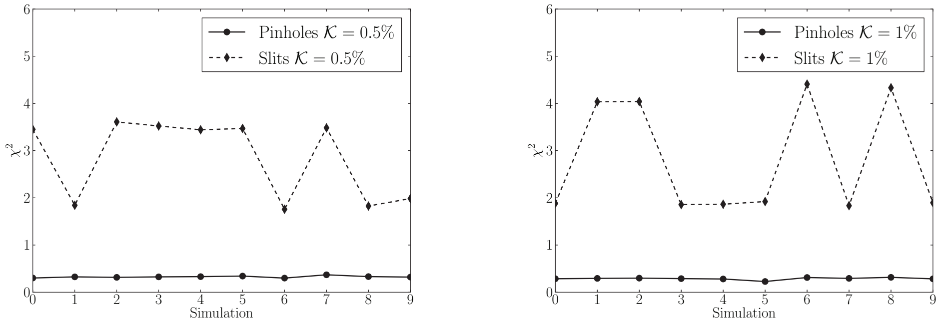

(a) $\sigma = 23\,\mu m$

(b) $\sigma = 33\,\mu m$

Figure 6.9: $\chi^2$ for pinholes (dots) and slits (diamonds) for different beam sizes.

As a conclusion, according to simulations, SRI beam sizes can be helpfully performed in Xanadu, preferably using a double pinholes system.

## 6.2 EXPERIMENTAL RESULTS

### 6.2.1 *The Setup*

A schematic layout of the SRI experimental setup is drawn in Fig. 6.10 highlighting the practical elements used to image the interferogram and not used in Fig. 6.1 for the SRW simulations (the magnifying eyepiece, the polarizer and the color filter). The details about the light transportation from the source point to the optical table in the Xanadu beamline was presented in Sec. 5.2.

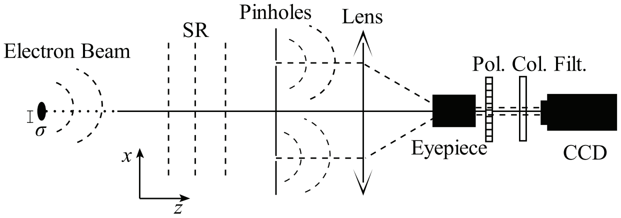

Figure 6.10: Sketch of the SRI experimental setup: the synchrotron radiation (SR) produced by the beam passes through the double pinhole system and is imaged through a lens and an eyepiece to the CCD. The radiation polarization and the wavelength are selected through a polarizer (Pol.) and a color filter (Col. Filt.).

The required components to produce the interferogram installed on the table are described below:

- Double aperture system: although different shapes (slits and pinholes) were tested, all the relevant experiments in this work were performed using a double-pinhole mask, in agreement with the simulations studies presented in Sec. 6.1 and confirmed with practical experience. The standard mask is composed by two pinholes of diameter 3 mm separated by 16 mm;
- Apochromat lens (BORG ED500 $f = 500\,\text{mm}$, flatness $\frac{\lambda}{10}$) to focus the two light beamlets for proper detection of the interferogram;
- Eyepiece (Takahashi MC LE 18 mm), to magnify the interferogram;
- Polarizer: (Thorlabs LPVISE200-A) to select the $\sigma$-polarization of the synchrotron radiation;
- Bandpass filter: (Thorlabs FB540-10) to monochromate the light around $\lambda = (540 \pm 10)\,\text{nm}$;
- CCD camera (Bassler Scout scA1300-32gm), with a pixel size of 3.75 µm. In order to avoid the detrimental effects of the mechanical vibrations presented in Sec. 5.4, the exposure time is usually set to 1 ms.

A critical point to perform SRI measurements is the proper alignment of the components listed above, which are installed on a rail. A first rough alignment is done to obtain the fringes on the CCD and then the eyepiece position is slightly scanned until the maximum visibility is obtained, checking in the meantime that the position of the centroid of the two beamlets does not move.

### 6.2.2 *Data Analysis: Fitting Algorithm*

An example of interferogram in the horizontal and vertical direction is shown in Fig. 6.11 (top plots). In order to infer the beam size, the central slice of the interferogram is projected ($\pm 10$ pixel columns for the horizontal case, and $\pm 10$ pixel rows for the vertical).

Projected data are fitted using a slightly modified version of Eq. 5.22:

$$I_{PH}(x) = I_0 \left\{ \frac{J_1\left(\frac{2\pi a(x+x_0)}{\lambda f}\right)}{\left(\frac{2\pi a(x+x_0)}{\lambda f}\right)} \right\}^2 \times \left\{ 1 + V\cos\left(\frac{2\pi D(x+x_0)}{\lambda f} + \varphi\right) \right\} + A + Bx, \quad (6.7)$$

where beside the parameters of Eq. 5.22, $x_0$ parametrizes the center of the interferogram, $\varphi$ was added to take into account a phase shift of the fringes with respect to the envelope (due to the asymmetry of the double-pinhole system with respect to the synchrotron light fan) and $(A + Bx)$ considers a linear background related to the noise of the CCD. These parameters are left as free parameters during the fitting process, as well as the interferogram intensity $I_0$, the distance between pinholes $D$, the focal length of the optical system $f$ and the visibility $V$. Other parameters such as the

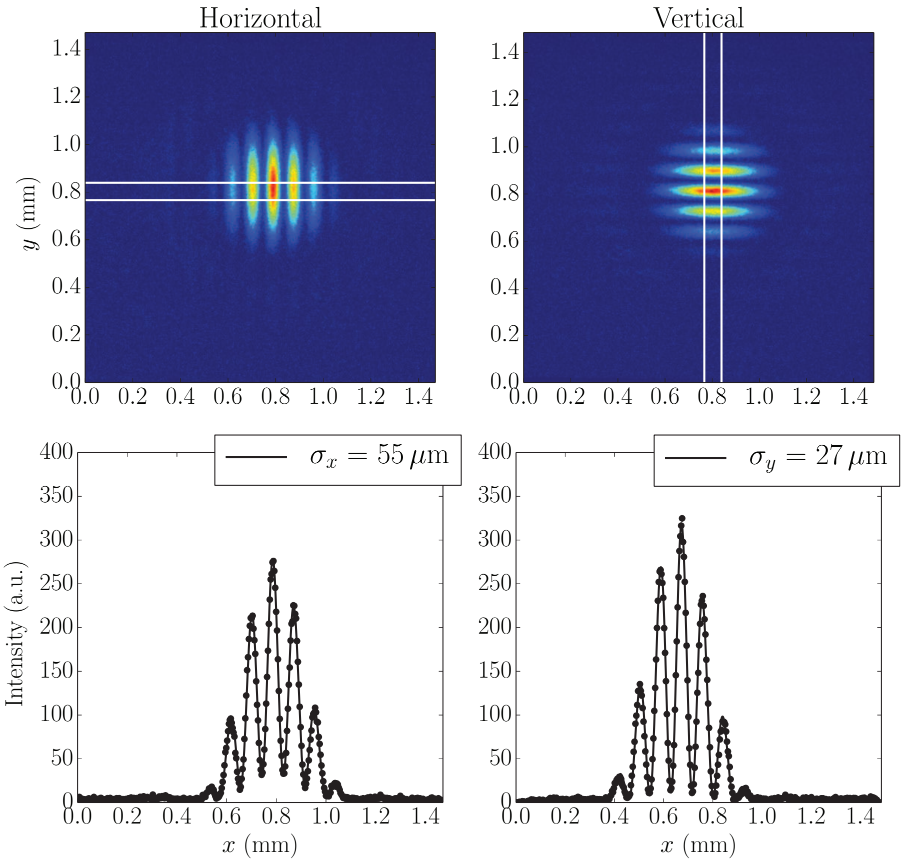

Figure 6.11: Horizontal and vertical SRI. Top images are raw interferograms, the while lines indicates the slice uses to obtain the beam size. The dots in the lower plots are the projections of the slices defined by the white lines. The black lines in the lower plots are the results of the fitting process.

selected wavelength $\lambda$, the pinholes diameter $a$ and the distance between the source and the pinholes $L$, are fixed to their experimental values: $\lambda = 540\,\text{nm}$, $a = 1.5\,\text{mm}$ and $L = 15\,\text{m}$.

Given the high number of free parameters, the fitting process is very sensitive to the initial guesses, which are inferred as follows:

- $x_0$ is estimated by the position of the interferogram maximum.
- $\varphi$ is set to zero since the effect of the asymmetry is very low. A typical value for this parameter is in the order of some mrad.

- A and B: the first is estimated considering one of the first values of the projection, while the second is set to 0, since the effect of the linear noise is usually small.
- D: the distance between the pinholes is left as free parameter since it refers to the distance seen by the wavefront and therefore it can slightly change depending on the quality of the optical path (see Sec. 5.3). Initially the distance between the pinholes center is measured by means of a caliper. Usually a mask with $D = 16\,\text{mm}$ is used, as in the case of Fig. 6.11.
- V: the visibility is estimated according to:

  $$V = \frac{I_{Max} - I_{Min}}{I_{Max} + I_{Min}}, \tag{6.8}$$

  where $I_{Max}$ and $I_{Min}$ are respectively the maximum and the minimum value of an interferogram oscillation. For a single electron the theoretical visibility is 1 and in general the larger is the beam size the smaller is the visibility. In Figure 6.11 bottom, this effect is particularly evident since the horizontal beam size is almost twice the vertical one.
- f: The system focal length depends on the focal lengths of the apochromat lens ($f_{Apo} = 500\,\text{mm}$) and the eyepiece ($F_{EP} = 18\,\text{mm}$) as:

  $$f = \frac{F_{Apo} \times F_{EP}}{\tau}, \tag{6.9}$$

  where $\tau$ is the distance between the two focal planes. Since the exact position of the eyepiece principal plane is not provided by the manufacturer, $f$ is a difficult parameter to precisely evaluate. A first guess on $f$ is calculated using the envelope of the interferogram. An example is shown in Fig. 6.12, corresponding to the vertical interferogram in Fig. 6.11. Black dots are obtained selecting the maxima of each fringe. A fit of the envelope is performed using the first part of Eq. 6.7 and the background components:

  $$I_{Env}(x) = I_0 \left\{ \frac{J_1\left(\frac{2\pi a(x+x_0)}{\lambda f}\right)}{\left(\frac{2\pi a(x+x_0)}{\lambda f}\right)} \right\}^2 + A' + B'x, \tag{6.10}$$

  where $(A' + B'x)$ parametrizes a linear background. From this fit the total focal length $f$ is inferred. The result obtained for Fig. 6.12 is $f = 2429\,\text{mm}$, which, according to Eq. 6.9, provides $\tau = 3.7\,\text{mm}$, i. e. a value estimated to be reasonable.

Using the initial parameters, the fit is performed successfully with $\chi^2$ values usually lower than 1. As an example fits are plotted in Fig. 6.11 (bottom) as a black lines: the measured data (black dots) are well reproduced. In this case $\chi^2 = 0.5$ for the horizontal measurements and $\chi^2 = 0.6$ for the vertical, were obtained.

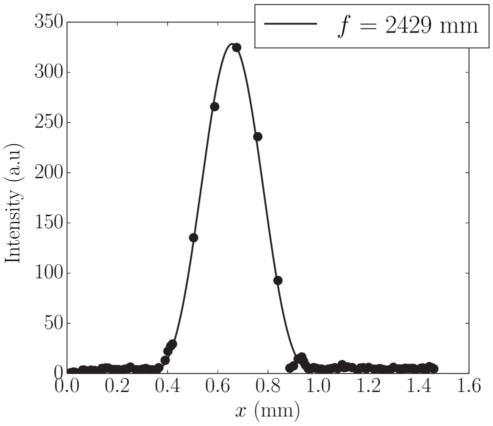

Figure 6.12: Fit of the interferogram maxima to estimate the focal length of the SRI system.

The fit provides the value of the visibility V and the distance between the pinholes D, from which the beam size is inferred using:

$$\sigma = \frac{\lambda L}{\pi D}\sqrt{\frac{1}{2}\log\left(\frac{1}{V}\right)}. \tag{6.11}$$

In the case presented in Fig. 6.11 both the horizontal and the vertical beam sizes:

$$\sigma_x = 55\,\mu\text{m} \qquad \text{and} \qquad \sigma_y = 27\,\mu\text{m} \tag{6.12}$$

are compatibles with the lattice analysis performed using LOCO for the given day: [1]

$$\sigma_x^{LOCO} = 56\,\mu\text{m} \qquad \text{and} \qquad \sigma_y^{LOCO} = 26\,\mu\text{m}. \tag{6.13}$$

### 6.2.3 *Stability Measurements*

Due to mechanical vibrations the results from the interferogram fluctuate by $\simeq 5\%$. In order to limit the effect of the fluctuations several interferograms, usually 100, are registered for each measurement. The fitting process is applied separately to each interferogram, but only the ones providing a $\chi^2 < 1$ are selected. The final result is the average over all the selected measurements, while the statistical error is provided by the standard deviation of the results distribution. Usually, out of 100 acquisitions, around 70 are selected for the analysis.

Figure 6.13 presents the beam size results σ, the focal distance f and the distance between the pinholes D, for each of the selected interferograms.

---

[1] The beam size, as well as the emittance, is not fixed in general but depends on several external aspects acting on the machine lattice. For this reason a LOCO is applied at the beginning of every operation week to predict the expected values for the given lattice.

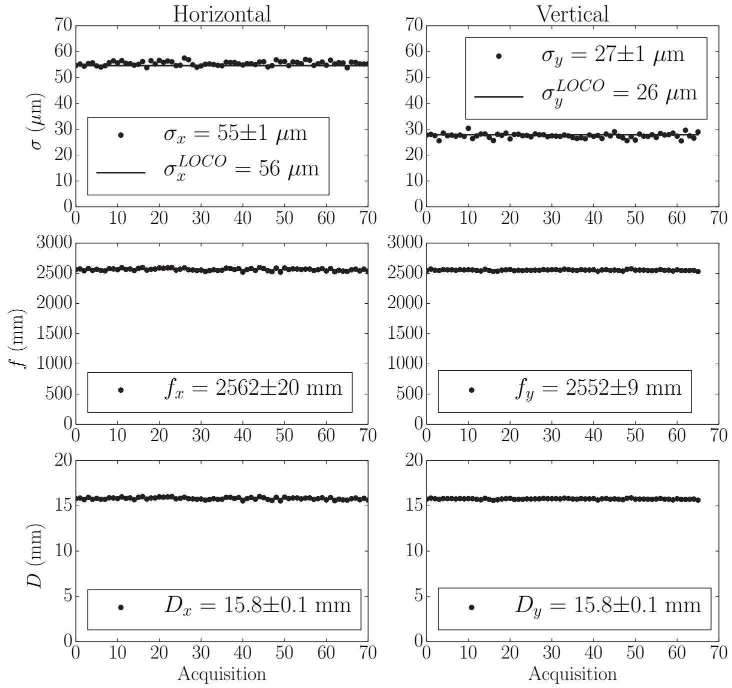

Figure 6.13: Results for the beam size σ, focal distance f and distance between the pinholes D for all the selected interferograms.

Again, the beam size results are compatible with the ones estimated by LOCO (see Eq. 6.13), even if some fluctuations are present in both horizontal and vertical directions.

The average focal length changes slightly (0.4%) between vertical and horizontal measurements. This is related with the relative position of the pinholes, the light fan, and the focusing lens. If the pinholes are not exactly centered with respect to the radiation footprint, the distance crossed by the light to reach the aperture system is slightly different in the two planes. According to Eq. 6.6, the total focal length f also changes slightly.

The distance between the pinholes obtained by the fit ($D = 15.8 \pm 0.1\,\mathrm{mm}$) is compatible with the manufacturing distance ($D = 16\,\mathrm{mm}$) and with the modifications seen by the wavefront due to possible optical path deformations (recall Sec. 5.3).

## 6.3 PINHOLES DISTANCE SCAN

Until this moment the beam size was measured fixing the distance between the pinholes and measuring the visibility. The value for σ is obtained by inverting Eq. 5.17, which is defined assuming that the electron beam producing the synchrotron radiation has a Gaussian distribution.

If the beam distribution is Gaussian, the visibility function also is Gaussian:

$$\gamma(D) = e^{-\frac{1}{2}\left(\frac{2\pi}{\lambda}\frac{\sigma}{L}D\right)^2}. \tag{6.14}$$

A way to verify this assumption is to directly reconstruct $\gamma(D)$ by measuring the visibility $V$ at different distances between pinholes $D$ and fitting the results using Eq. 6.14. Since all the parameters of the fit are known, it is possible to infer the beam size from the same measurement.

At ALBA this technique can be applied only on the horizontal plane, due to the limited aperture of the vertical fan. Pinhole distance was scan in a range [8,30] mm, which is dictated by the width of the synchrotron radiation footprint and the diameter of the pinholes. For each pinholes distance, 100 interferograms were registered and fitted using Eq. 6.7.

The resulting visibilities were fitted using Eq. 6.14, leaving the $\sigma$ as free parameter. The result is presented in Fig. 6.14 and is in good agreement with the expected horizontal beam size (see Eq. 6.13); furthermore the low $\chi^2$ proves that the assumption of a Gaussian distributed beam is acceptable.

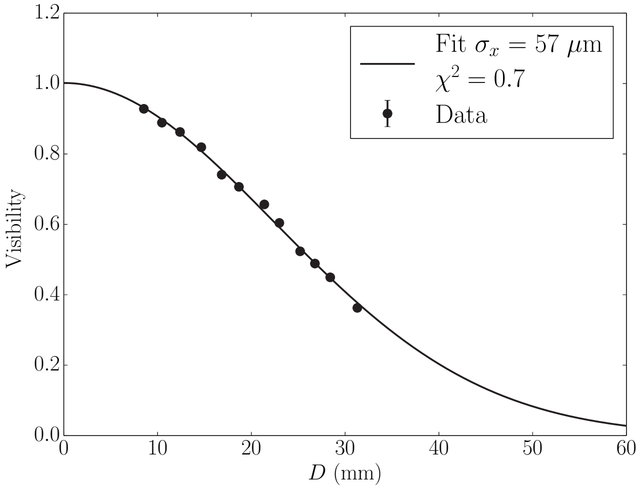

Figure 6.14: Visibility as a function of the pinholes distance. Black dots correspond to the measured data, while the black line is obtained by fitting the data using Eq. 6.14

# 7

# SRI: APPLICATIONS AND RESULTS

## 7.1 FULL TRANSVERSE BEAM PROFILE RECONSTRUCTION

New generation of Synchrotron Light Sources are characterized by their low emittance and low coupling beams, with horizontal emittances in the nm range (or below). The beam coupling is usually controlled using skew quadrupoles and it typically ranges between ~[0.1, 2]%. Changing the beam coupling not only provides a change in the vertical beam emittance, it also produces a change in the beam tilt. Figure 7.1 shows the (modeled) behaviour of the beam tilt angle, and the beam sizes along the first ALBA quadrant (where the SRI source point is located) for three different set of skew quadrupoles, providing three different beam couplings: in all the dipoles the beam tilt changes.

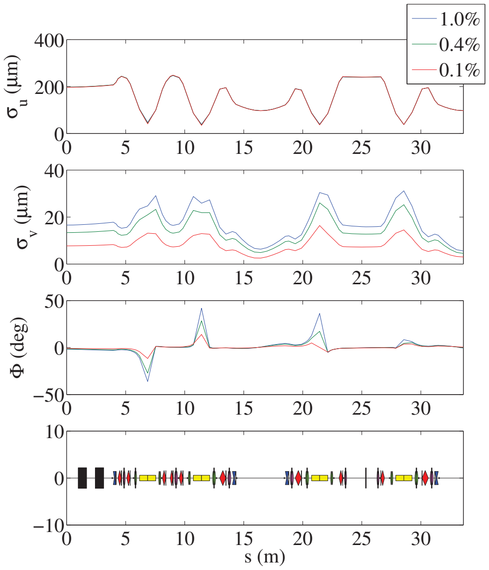

Figure 7.1: Beam tilt angle Φ for three different settings of the skew quads at ALBA in Sector 1. Bending magnets are represented by yellow rectangles. Xanadu beamline takes light from the first bending.

However the standard SRI technique using a double-pinhole system only provides the projected beam size along the axes of the apertures and therefore information about the beam tilt change for different couplings is not available.

This Section presents a completely new method to reconstruct the transverse beam profile is developed using a rotating double-pinhole system, which allows to properly measure the beam size and relative beam-tilt angle. Furthermore, it was demonstrated through simulations, how this method allows to infer ultra-small beam sizes, in case of limitations of the standard SRI setup [81, 82].

### 7.1.1 *Beam Shape Reconstruction*

A generic shape with a 2-axis symmetry, such as the beam ellipse, can be reconstructed by measuring its projections $\sigma_p$ along different axis. This kind of measurements is performed rotating the double-pinholes mask by a given angle $\theta$.

When tilting the 2-pinholes axis by $\theta$, the interference fringes appear tilted. The projection $\sigma_p$ is inferred by analyzing the fringes in the direction of the rotating angle $\theta$. Figure 7.2 presents interferograms obtained for pinholes rotated at 0°, 45°, 90° and 135° and the related fit, measured at Xanadu.

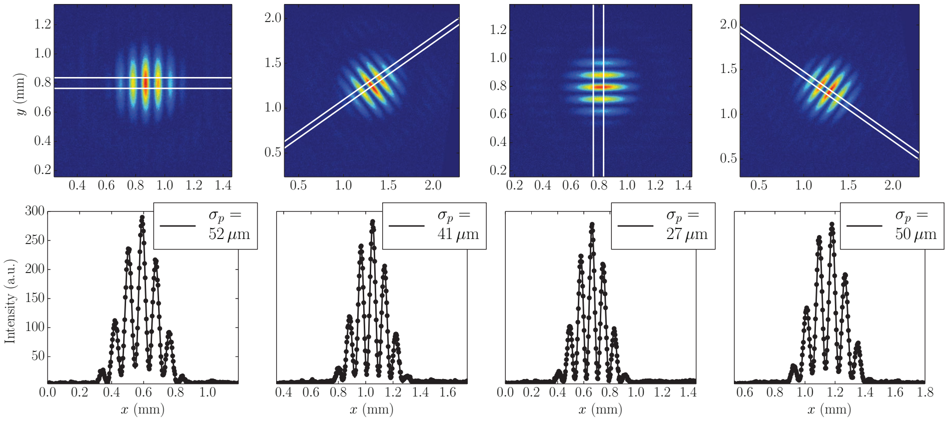

Figure 7.2: Interferograms rotated at 0°, 45°, 90°, and 135° to measure the size of the projection of the beam along the respective axis. White lines in the top plots are oriented in the direction of the pinholes axis, rotated by angle $\theta$, and represent the slices selected for the fitting process.

From each measurement at a given $\theta$, two parallel lines

$$y = mx \pm Y_0, \tag{7.1}$$

tangents to the transverse beam shape, can be calculated as shown in Fig. 7.3. The slope of the lines, $m$, is given by the 2-pinholes tilt angle $\theta$, while the position of the intersecting points between the tangent line and the y-axis, marked as $\pm Y_0$ are inferred from the triangle $OPY_0$. The mathematical expressions are:

$$\begin{cases} m = \tan(\theta + 90^\circ) \\ \pm Y_0 = \pm \frac{\sigma_p}{2\sin(\theta)} \end{cases} \tag{7.2}$$

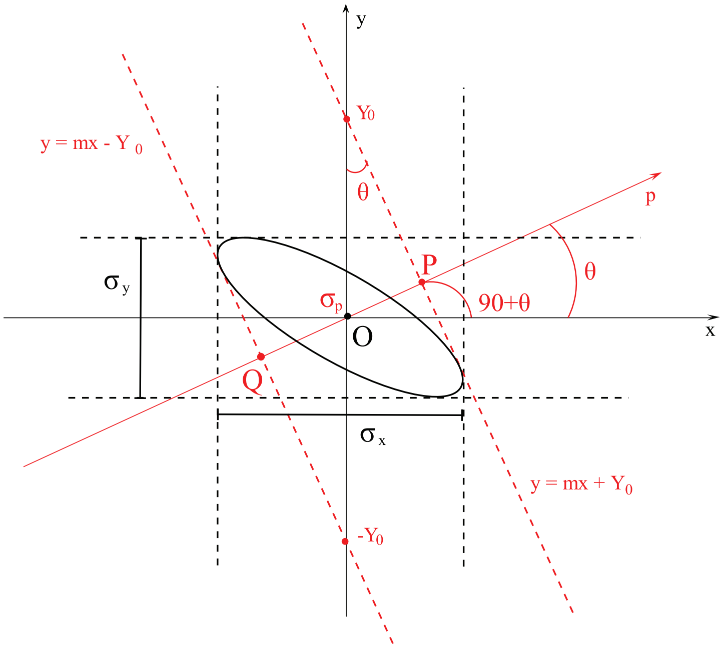

Figure 7.3: Sketch of the transverse beam shape reconstruction using tangent lines calculated according to Eq. 7.2. Black lines represent the laboratory reference system, black dashed lines are drawn considering $\theta = 0^\circ$ and $\theta = 90^\circ$ and provide the projection along the $x$ and $y$ axis ($\sigma_x$ and $\sigma_y$). The red solid line represent the rotation direction of the 2-pinholes axis of a generic angle $\theta$, while red dashed lines are the tangent lines calculated taking into account $\sigma_p$ (the distance PQ in the drawing).

An example of beam reconstruction is presented in Fig. 7.4, top. Data were taken rotating the pinhole system every 5° in the range [0°, 200°], the tangential lines are calculated using Eq. 7.2. This provides a "tomographic" reconstruction where the beam profile corresponds to the hollow shape enclosed by the black tangential lines. Obviously, the larger is the number of tangent lines, the more precise the beam shape can be reconstructed.

Next, a useful simplification assuming an elliptic beam is presented.

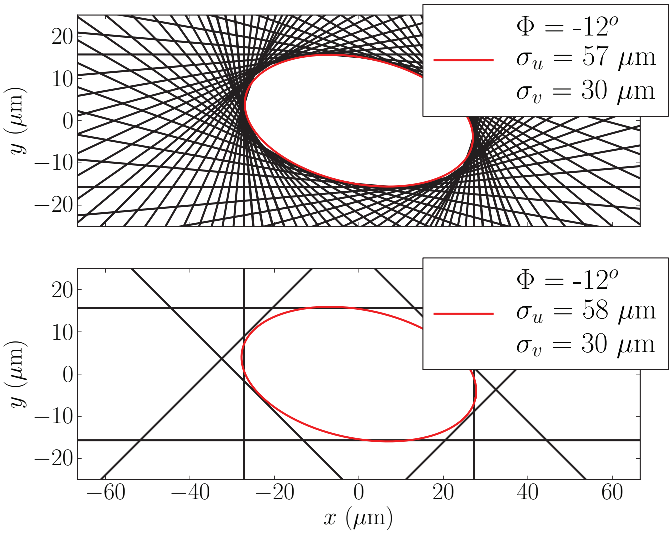

Figure 7.4: The top plot shows the full reconstruction of the transverse beam shape using tangents lines. In the bottom plot, only the lines obtained by the projections at 0°, 45°, 90° and 135° are considered. The red ellipses are drawn using the results of the fit presented in Fig. 7.6

.

### 7.1.2 *Elliptic Beam*

Assume that the beam can be described by the tilted ellipse shown in Fig. 7.5, with $\sigma_u$ and $\sigma_v$ the ellipse semi-axis and $\Phi$ the ellipse angle tilt. This ellipse is described by the general expression:

$$ax^2 + by^2 + 2cxy = 1 \, , \tag{7.3}$$

where the parameters $(a, b, c)$ are:

$$a = \left(\frac{\cos^2\Phi}{\sigma_u^2} + \frac{\sin^2\Phi}{\sigma_v^2}\right) \tag{7.4a}$$

$$b = \left(\frac{\sin^2\Phi}{\sigma_u^2} + \frac{\cos^2\Phi}{\sigma_v^2}\right) \tag{7.4b}$$

$$c = \cos\Phi\sin\Phi\left(\frac{1}{\sigma_v^2} - \frac{1}{\sigma_u^2}\right) \, . \tag{7.4c}$$

For convenience, Eq. 7.3 was written in analogy with the well-known *phase space ellipse* in the Accelerator Physics, where the parameter b in this case corresponds to

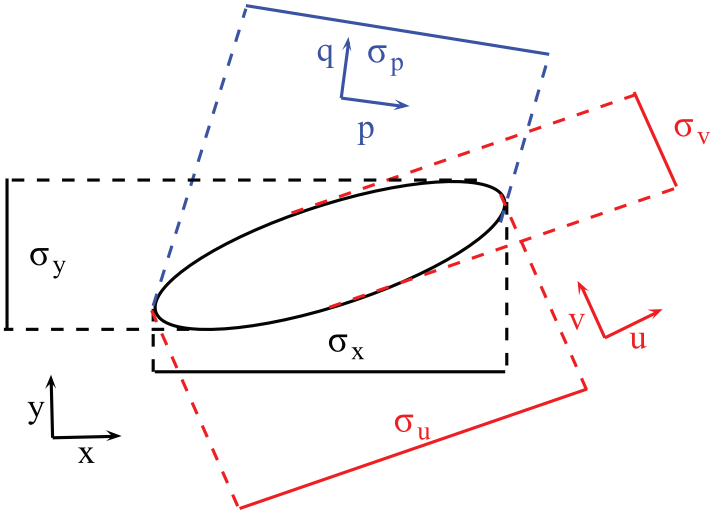

Figure 7.5: General tilted ellipse: $(x, y)$ is the laboratory reference system (in black), $(u, v)$ refers to the reference system in which the ellipse is not tilted (in red), while $(p, q)$ refers to the one rotated by an angle $\theta$ with respect to the laboratory system (in blue).

$\beta/\varepsilon$ in Ref. [30] (see also Fig. A.3), with $\beta$ the vertical beta function and $\varepsilon$ the beam emittance. The horizontal projection can be expressed as:

$$\sigma_p = \sqrt{\left(\frac{A}{\pi}\right) b} \, , \tag{7.5}$$

where $A$ corresponds to the ellipse area,

$$A = \pi \, \sigma_u \, \sigma_v \, . \tag{7.6}$$

Merging Eqs. 7.4c, 7.5 and 7.6, we find that the horizontal projection is:

$$\sigma_x = \sqrt{\sigma_u^2 \cos^2 \Phi + \sigma_v^2 \sin^2 \Phi} \, . \tag{7.7}$$

Rotation of the double-pinhole system by a known angle $\theta$ is equivalent to rotate the coordinate system by the same amount. In this new coordinate system, the tilt angle is now $\Phi - \theta$ and so the (new) projection is:

$$\sigma_p(\theta) = \sqrt{\sigma_u^2 \cos^2(\Phi - \theta) + \sigma_v^2 \sin^2(\Phi - \theta)} \tag{7.8}$$

where $\sigma_p(\theta)$ is the projected beam size at the angle $\theta$.

The same data used to reconstruct the beam shape in Fig. 7.4 were fitted using Eq. 7.8. The result is presented in the top plot of Fig. 7.6. This function fits to the data accurately, indicating a good agreement with the proposed model. At the maxima location ($\theta \simeq 170°$) the measurements look flatter with respect to the fit. This might indicate that the real shape of the beam is not exactly elliptic.

From the same set of data, the four projections for 0°, 45°, 90°, and 135° were extracted. The data and fit using Eq. 7.8 are presented in the middle plot of Fig. 7.6. Also in this case the agreement is good: in the bottom plot of Fig. 7.6 the difference between the two fitting curves as a percentage of the first ($\frac{\Delta\sigma_p}{\sigma_p}$) is presented. The maximum deviation is lower than 1 µm. This value is smaller with respect to the statistical error associated with standard SRI beam size measurements ($\gtrsim$1 µm).

The red ellipses presented in Fig. 7.4 are drawn using the results of the fits presented in Fig. 7.6.

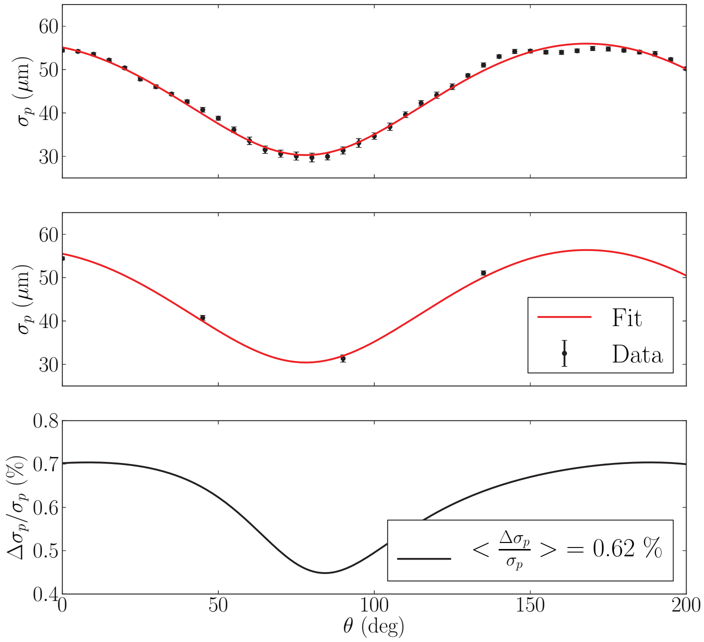

Figure 7.6: Beam projection as a function of the pinhole rotation angle $\theta$. The first plot results from 40 measurements, while the second from the projections at 0°, 45°, 90°, and 135°. The third plot (black line) shows the difference between the fits obtained with 40 and 4 points divided by the values of the 40 points curve.

The same procedure was applied to other quartets of projections taken at angles separated by 45°, starting from different initial angles $\theta_0$, i. e. $\theta_0 = 0°$ refers to the quartet [0°, 45°, 90°, 135°], while $\theta_0 = 5°$ corresponds to [5°, 50°, 95°, 140°] . The relative difference $\frac{\Delta\sigma}{\sigma}$ was calculated for the different quartets and results are presented in Fig. 7.7. The mean deviation from the results obtained is always below the 1% of the value obtained when fitting 40 points: this error is lower than the statistical error obtained during standard SRI measurements and indicates that there is no preferred quartet combination for the fitting process.

This method allows to properly reproduce the geometrical beam ellipse, since it provides its eigenvalues ($\sigma_u$ and $\sigma_v$) and the beam tilt. Moreover, using the fitting method,

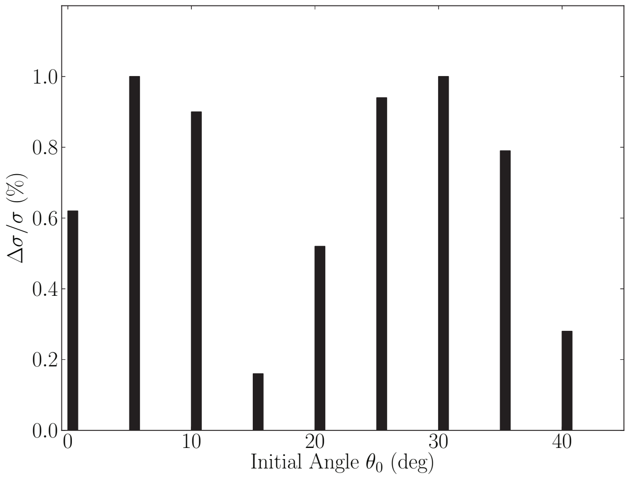

Figure 7.7: Mean value of the difference between the curve obtained by fitting 200 projections and the one fitting only 4 projections as a percentage of the first.

only four projections are required to reconstruct the full beam: this simplification allows to significantly speed up the measurement process.

### 7.1.3 *Results for Different Couplings*

In order to check the reconstruction technique reliability, measurements were performed at five different values of the machine coupling to change tilt and beam sizes.

The beam sizes values were measured rotating the double pinhole system at 0°, 45°, 90° and 135°, using the 2-pinholes SRI reconstruction. The fit results using Eq. 7.8 are presented in Fig. 7.8(a), while the reconstructed ellipses inside the tangent lines are presented in Fig. 7.8(b).

A machine optics analysis using the program "Linear Optics from Closed Orbits" (LOCO) [31, 32] was launched at each coupling in order to compare the results obtained by the measurements with the expected values.

Figure 7.9 presents the comparison of SRI reconstruction with LOCO outputs. Results for the beam sizes are consistent at least for the first four values of the coupling and only for the largest coupling (0.8%) the LOCO and the SRI values differ for more than $1-sigma$ both for horizontal and vertical beam sizes. On the other hand, the measured tilt angle ($\Phi$) is always within the statistical error of the measurements. Taking into account that the pinholes mask was rotated manually and possible misalignments between the rotation stage and the CCD (about 3°), the experiments are considered satisfactory.

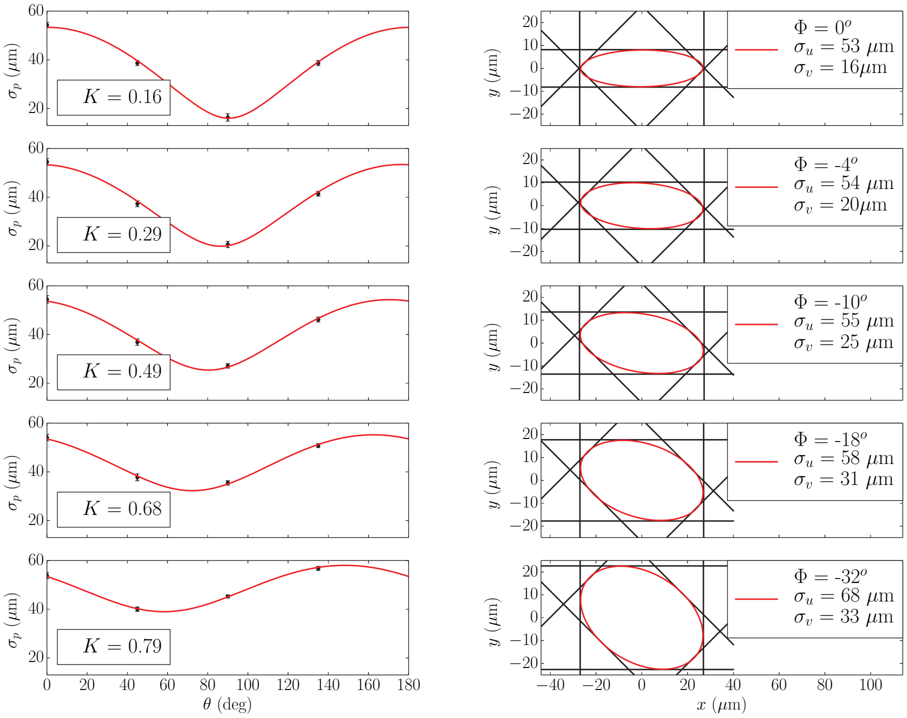

(a) *Fit of projections taken at 0°, 45°, 90°, and 135°. Black dots are real data, and the red lines are obtained by fitting.*

(b) *Beam ellipse: black lines are calculated from real data and the red ellipse is drawn from the result of the fit.*

Figure 7.8: Beam ellipse reconstruction at different couplings.

### 7.1.4 *Ultra-Low Beam Size Measurements*

At ALBA the smallest vertical beam size achievable is 15 µm but other machines currently operate at beam sizes of 3.5 µm [83] while future machines will reach $\sigma_y = 2$ µm [84, 85], which cannot be measured with standard SRI technique due to practical limitations [83]. The "rotating mask" technique can be applied to the measurement of this ultra-low beam sizes: SRW simulations were performed to prove this possibility.

Simulations are performed as in Sec. 6.1 and tilting the double-pinhole mask. An elliptic beam with zero tilt and an horizontal beam size of 55 µm was generated. The vertical beam size was changed from 2 to 10 µm and the tilt angle left at 0 for simplicity. To perform the beam reconstruction, projection measurements were simulated sampling the angle in steps of 15°, by skipping $\theta = 90°$, which corresponds to the minimum beam size.

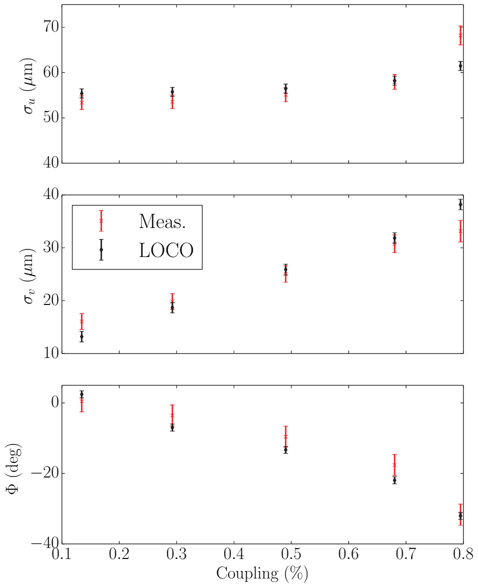

Figure 7.9: Comparison of the SRI reconstruction with the results from LOCO for the horizontal and vertical beam size and the beam tilt at the Xanadu location.

Final interferograms were analyzed and the projected beam sizes as a function of the angles were fitted using Eq. 7.8 to obtain the beam ellipse parameters. Figure 7.10 presents the results obtained when simulating a non-tilted beam with horizontal and vertical beam sizes of 55 µm and 2, 5, 7 and 10 µm respectively. Obtained results are compatible with the initial parameters.

In order to understand the limit of the SRI reconstruction method for ultra-small beam sizes, a systematic study on the error that might affect the fit was performed, where the SRW simulations were taken as starting point. Each reconstruction consists of beam projections sampled for 11 rotation angles, θ.

When performing real measurements at Xanadu beamline, each SRI projected beam size measurement fluctuates by around 1.5 µm. To simulate these fluctuations, each $\sigma_p$ used for the reconstruction was smeared by a random value generated according to a normal distribution centered in 0 and with standard deviation given by the expected statistical fluctuation. For each beam size the smearing and reconstruction process are repeated 100 times. The average of the results and the corresponding standard deviation provide the final beam size with an associated error.

Statistical fluctuations of 0.5, 1, 1.5 and 2 µm were used to smear the results. The standard fluctuation obtained when measuring the ALBA beam size is around 1.5 µm, mainly due to the Xanadu optical components vibrations. Other SRI measurements,

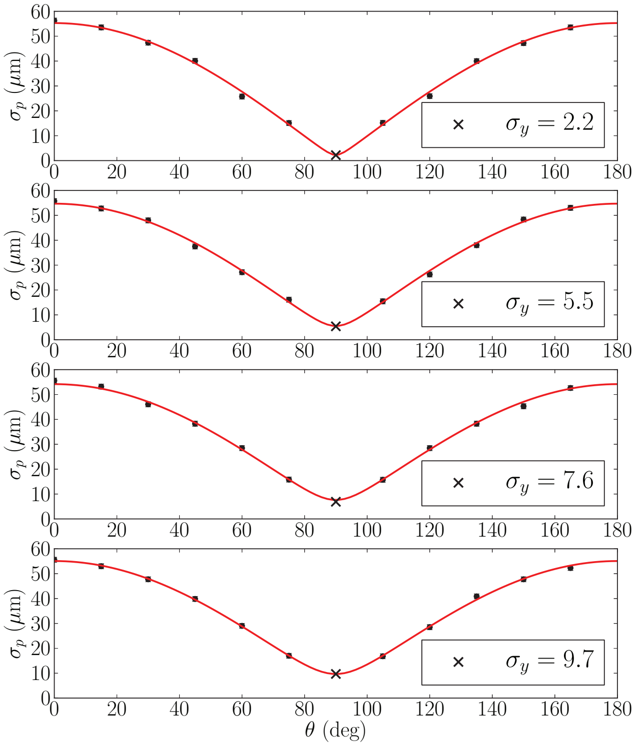

Figure 7.10: SRW simulated 2, 5, 7 and 10 μm vertical beam size reconstruction using the rotated SRI technique. Black dots are the SRW simulated data, the error bar is fixed to 1.5 μm and red line is the result of the fit using Eq. 7.8. Black × indicates the inferred vertical beam size, using the fit.

performed in different machines at more stable beamlines, may have sub-micrometer fluctuations [37].

The results for the different beam sizes are presented in Table 7.1 and Fig. 7.11: to a small smearing statistical error, corresponds a small error associated with the final reconstruction. For 2 μm beam sizes, even the smallest deviation leads to fluctuations in the beam size reconstruction of 85% of expected value. This stress the importance of a careful design of the SRI beamlines, with good quality of the optical elements and stable supports to decrease the measurement fluctuations.

On the other hand, the average of several measurements provides for all the simulated beam sizes a result compatible with the expectations improving the standard SRI resolution.

| $\sigma_y$ Expected (μm) | $\sigma_y$ Rec. (μm) | Smeared Rec. $\sigma_y$ (μm) | | | |
|---|---|---|---|---|---|
| | Not Smeared | Sim. 0.5 μm | Sim. 1 μm | Sim. 1.5 μm | Sim. 2 μm |
| 2 | 2.2 | 2.3±1.7 | 2.6±2.3 | 2.5±2.8 | 3.3±3.4 |
| 5 | 5.4 | 5.3±1.1 | 5.7±1.6 | 5.7±2.1 | 6.5±2.9 |
| 7 | 6.9 | 7.0±0.8 | 6.6±1.7 | 6.9±1.9 | 7.5±2.4 |
| 10 | 9.7 | 9.7±0.6 | 9.5±1.4 | 9.6±2.1 | 9.3±2.53 |

Table 7.1: Results of SRW simulations of beam profile reconstruction for ultra-small beam sizes: rotating SRI reconstruction without smearing are compared with results produced by smearing the rotated beam sizes by 0.5, 1, 1.5 and 2 μm.

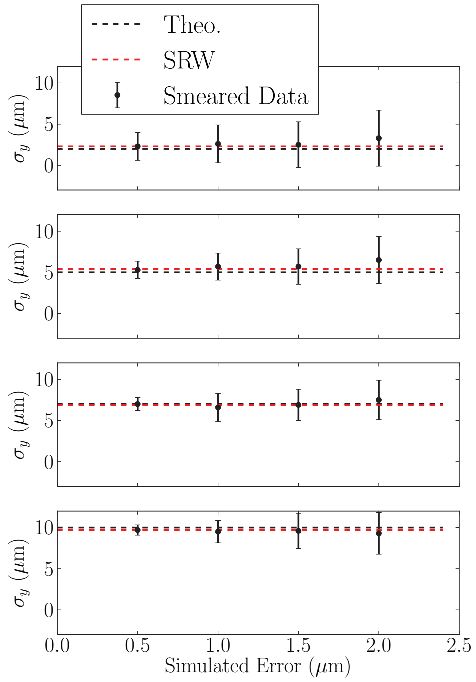

Figure 7.11: Results for 2 μm, 5 μm, 7 μm and 10 μm beam size reconstruction for SRI beam size measurement as a function of the measurement fluctuations. The error bar results from the standard deviation of the beam size of 100 smeared reconstructions, black dashed line is the theoretical value, while red dashed line is the result obtained performing rotating SRI SRW simulations.

### 7.1.5 *Emittance Measurements*

Thanks to the full beam reconstruction in the transverse plane, according to Eq. A.12 it is possible to measure the beam emittance.The machine parameters such as the

$\beta$ function and the dispersion at Xanadu location are obtained by LOCO, while the effective horizontal and vertical beam sizes are obtained with the full beam reconstruction technique. The results for the horizontal and vertical emittance $\varepsilon_u$ and $\varepsilon_v$ and the coupling $\mathcal{K}$ (see Eq. A.13) are presented in Fig. 7.12. Red dots represent the emittance measured using results from the full reconstruction technique, while black dots indicate the expected value obtained using LOCO. Error-bars are calculated using the statistical error of the SRI measurements and assuming an error of 2% on the LOCO estimation for the machine functions at the Xanadu location. The results are compatibles with LOCO expected values.

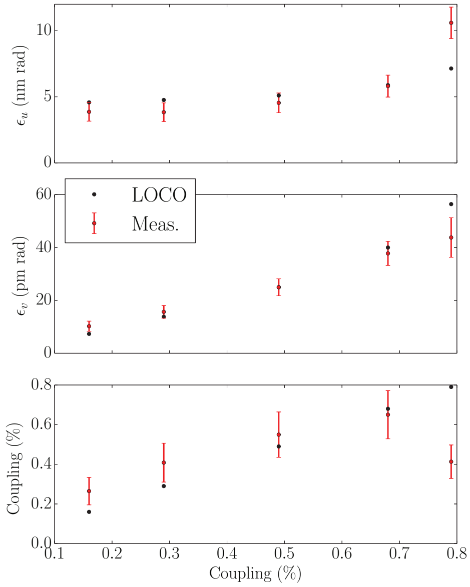

Figure 7.12: Results for the horizontal and vertical emittance, ($\varepsilon_u$, $\varepsilon_v$) and the beam coupling ($\mathcal{K}$). In red measurements performed with the full beam reconstruction technique, while in black results provided by LOCO.

## 7.2 SRI AT LOW CURRENT: MATCHING ALGORITHM

The results described in the previous sections corresponds to the ALBA standard operation condition, with a current of 130 mA. However, for low beam current (below $\simeq 50$ mA), the signal-to-noise ratio of the interferogram becomes poor and the SRI measurements are not reliable. The increase of the CCD exposure time cannot be larger than $\simeq 1$ ms, because for longer times the vibrations in the optical path strongly affect the SRI measurements (recall Sec. 5.4).

To overcome this limitation, an off-line matching algorithm was developed taking inspiration from the Shift and Add techniques used to improve the resolution and the dynamic range of astronomical images [86, 87, 66].

### 7.2.1 *Matching Algorithm*

The basic idea is to add N different interferograms until a proper signal-to-noise ratio is obtained: this cannot be done by a direct superposition of images, since it would be equivalent to increase the CCD exposure time. Intuitively the process consists on the overlap of several 2D interferograms, matching the horizontal and vertical center. This is done computing the cross-correlation between a reference image and the next and shift the latter in order to remove the effects due to vibrations.

The cross-correlation between two functions $f(t)$ and $g(t)$ is defined as:

$$(f \star g)(\tau) = \int_{-\infty}^{+\infty} f^*(t) \times g(t+\tau)dt \tag{7.9}$$

where $f^*(t)$ denotes the complex conjugate of $f(t)$ and $\tau$ is the spatial lag between the two functions.

The matching algorithm takes the first image as reference $\mathcal{R}(x, y)$ and computes the cross-correlation between $\mathcal{R}(x, y)$ and one of the following images $\mathcal{I}(x, y)$. To do so the images are first filtered applying a 2D low pass filter. Then the square of the cross-correlation $\mathcal{C}(\Delta_x, \Delta_y)$ is calculated applying Eq. 7.9, which avoids problems with complex values:

$$\mathcal{C}^2(\Delta_x, \Delta_y) = \{\mathcal{F}^{-1}(\mathcal{F}(\mathcal{R}^*(x, y)) \times \mathcal{F}(\mathcal{I}(x, y)))\}^2 \tag{7.10}$$

where $\mathcal{F}$ denotes the Fourier transform and ($\Delta_x$, $\Delta_y$) represents the lags in the horizontal and the vertical directions. The shift to be applied to the image $(\delta_x, \delta_y)$ corresponds to lag at the maximum intensity of the cross-correlation matrix:

$$\text{Max}(\mathcal{C}^2(\Delta_x, \Delta_y)) = \mathcal{C}^2(\delta_x, \delta_y). \tag{7.11}$$

To have a sub-pixel resolution the maximum is found projecting the cross-correlation matrix on the horizontal and the vertical axis and fitting it with a Gaussian function.

The image $\mathcal{S}(x, y)$, centered with respect to the one taken as a reference, is obtained shifting the raw image $\mathcal{I}(x, y)$:

$$\mathcal{S}(x, y) = \mathcal{I}(x - \delta_x, y - \delta_y). \tag{7.12}$$

Given a total number of images N, the final improved image is provided by:

$$\mathcal{I}_{Tot}(x, y) = \mathcal{R} + \sum_{n=1}^{N} \mathcal{S}_n(x, y). \tag{7.13}$$

### 7.2.2 *Results*

As a test, to simulate the low current conditions during normal operation, the exposure time of the CCD-camera was reduced of a factor 10 and set to 0.1 ms.

Experiments were performed with pinholes of 3 mm of diameter and separated by 16 mm. 3000 pictures were acquired using the fast CCD with an acquisition rate of 50 Hz to speed up the measurement process. The vertical beam size was measured since is the smaller and it is usually more difficult to resolve.

The algorithm described in the previous Section is applied to all the collected interferograms, and the final image is analyzed using the standard fitting process.

Figure 7.13 shows the central slice projection of each interferogram, without (top) and with (bottom) the application of the matching algorithm. In the first case the interferogram projections are shifted one with respect to the other and if summing directly the curves, the visibility decreases.

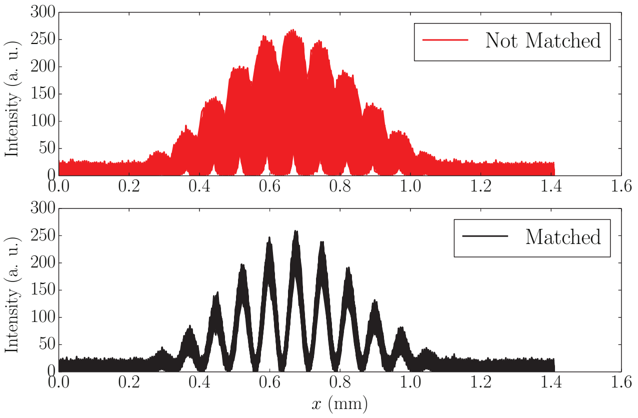

Figure 7.13: Projections of the central slice of each interferogram without (top, red) and with (bottom, black) the application of the matching algorithm.

Figure 7.14 presents the interferogram and the projection fit for a single acquisition (top), for the interferogram obtained by summing all the images without any treatment (middle) and with the application of the matching algorithm (bottom). In the first case (Fig. 7.14, top), when analyzing a single image at low exposure time, the intensity of the image is very low and the resolution of the interferogram is poor. When projecting the central slice over the $y$ axis, the data are noisy and the fit is not able to provide the correct result.

When all the interferogram are summed up directly (Fig. 7.14, middle) the final image is blurred as expected from the optical path vibrations. The fit provides a result that is much larger than the expected one.

Finally, the interferogram obtained summing the images after the application of the matching algorithm (Fig. 7.14, bottom) provides the expected result provided by LOCO.

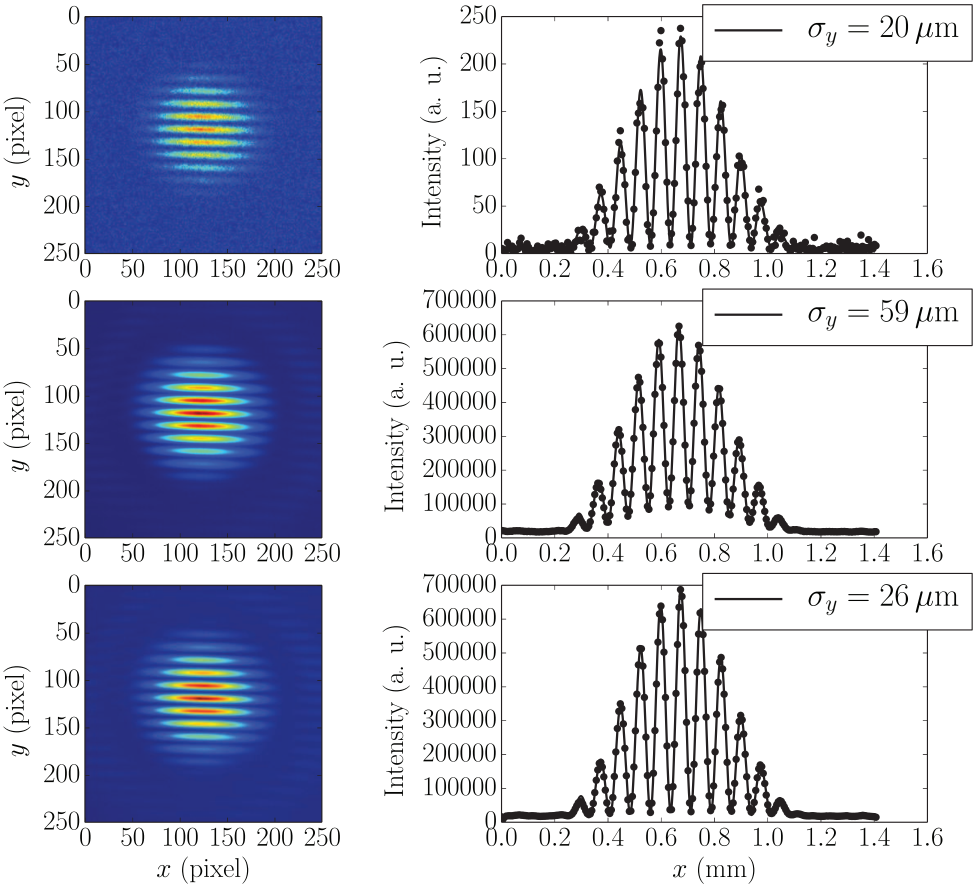

Figure 7.14: Interferograms and analysis of the projections for a single image at low exposure time (top), the direct sum of all the images (middle) and the sum of the images using the matching algorithm (bottom).

A coupling scan was performed to validate the method. Data were acquired using a standard exposure time (1 ms) and a lower one (0.1 ms) to simulate the low current operation mode (see Fig. 7.15). The matching algorithm was applied to interferograms acquired at low exposure times. The error bar of the results obtained with the matching algorithm is set to 1.5 µm, as in the case of standard conditions.

Figure 7.15 shows that the results obtained with the matching are compatibles with the measurements in the standard conditions, obtained using 1 ms of exposure time.

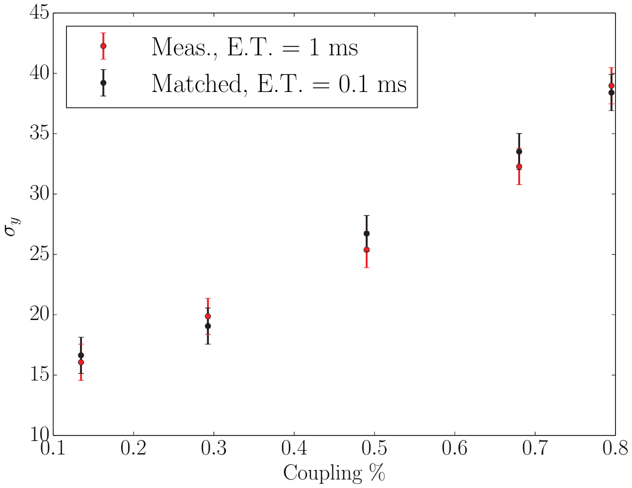

Figure 7.15: Coupling scan for standard SRI measurements (red dots) and the one obtained at low exposure time and applying the matching algorithm (black dots).

Finally, to proof the algorithm capability to measure the beam size at low current, data were acquired scanning this value.

This experiment was performed using pinholes of 5 mm of diameter to increase the flux of synchrotron radiation on the CCD. Interferograms were registered during multi-bunch operation, using a standard coupling ($\sigma_y^{\mathrm{LOCO}} = 25\,\mu\mathrm{m}$), for different currents in a range of [3,120] mA, using a standard CCD exposure time of 1 ms. Figure 7.16 presents the vertical beam size obtained either by using a standard data analysis: the associated error is the standard deviation of the results (in black) or by applying the matching algorithm (in red). The results for the $\chi^2$ are also presented in both cases (bottom plot of Fig. 7.16, using the same color schemes).

Results show that the matching algorithm is reliable to measure the vertical beam size at low current. It is worth noting that, when performing a standard data analysis, the first measurements (at 3 mA) present a very large error bar because the resolution of the interferogram is extremely poor and the fit is not properly working, as shown by the large $\chi^2$. Standard measurements start to provide reliable results at a current of 60 mA. On the other side, results obtained using the matching algorithm are stable at the expected value for $\sigma_y$ and the $\chi^2$ is always lower with respect to the one obtained with standard data analysis, thanks to the improvement of the resolution. As an example a single interferogram measured at 3 mA and the one obtained after matching 500 of them and their fits, are presented in Fig. 7.17. The improvement of the resolution is evident.

The matching algorithm is potentially useful when doing, for example, single bunch studies, where the beam current typically ranges between [0,10] mA.

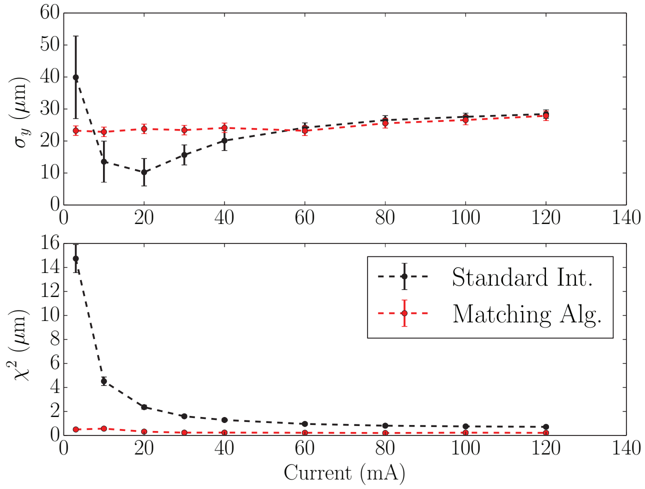

Figure 7.16: Vertical beam size (top) and $\chi^2$ (bottom) obtained without and with the application of the matching algorithm.

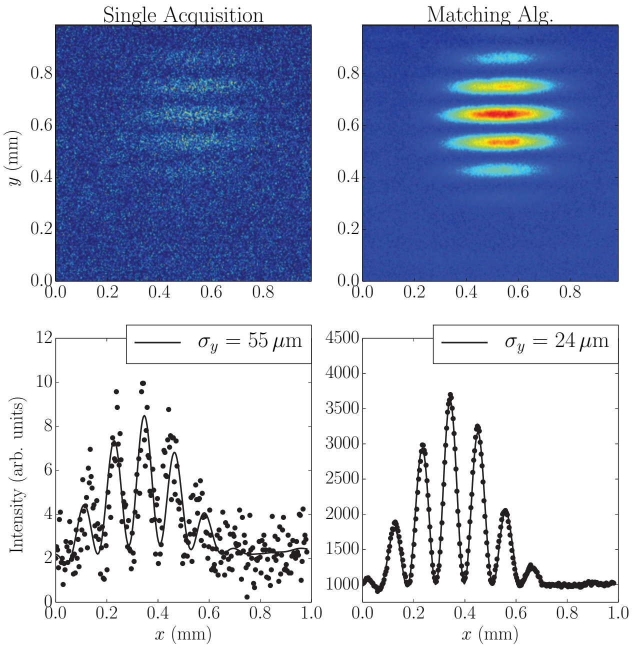

Figure 7.17: Single interferogram acquisition (left) and interferogram obtained applying the matching algorithm (right) and their fit, with a stored current of 3 mA.

## 7.3 BUNCH-BY-BUNCH SIZE MEASUREMENTS USING SRI

Accelerators performances are often limited by transverse Couple Bunch Instabilities (CBI) [88, 89, 90], where the field produced by the bunch $m$ affects the bunch $m+1$. The identification of the nature of CBI is not a straight forward task, being Resistive Wall and ion-related instabilities the most common types of transverse instabilities in light sources [91].

The study of the beam size evolution on a bunch-by-bunch base provide a good tool to understand these instabilities. This evolution can be analyzed by registering SRI-interferograms by means of a Fast Gated Camera (FGC), rather than a standard CCD as presented in Sec. 6.2.1.

### 7.3.1 *Fast Gated Cameras*

FGCs are able to reduce the exposure time down to 2 ns, corresponding to the ALBA RF-bucket length. Figure 7.18 presents the working principle of a general FGC [92]. When the light impinges on the image intensifier photo-cathode, photo-electrons are emitted and guided towards a Multi-Channel-Plate (MCP) by an electric field. A high potential is applied across the MCP, in such a way that electrons are accelerated in the channels and extract secondary electrons producing an amplification. The final electron cloud reaches the Phosphor and provides a light output which is finally read by the CCD. The gating mode is obtained by using a pulsed power supply that enables the operation of the MCP for the requested time.

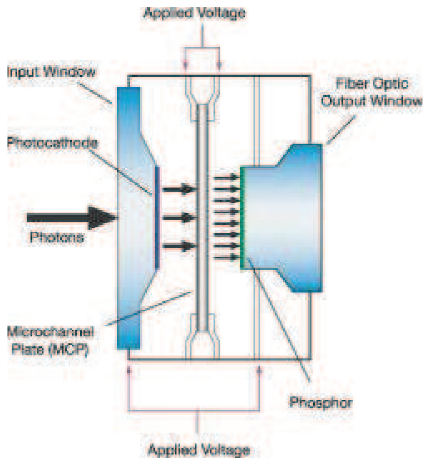

Figure 7.18: Working principle of the FGC: light produces photo-electron in the photo-cathode which are driven to the MCP. Here electrons are multiplied and accelerated down to the phosphor where they are again converted in visible light. The gate is obtained by inverting the voltage in the MCP.

Electrons exiting the photo-cathode are affected by space-charge effects, which typically enlarges the image generated by incident light. This image degradation may also depend on the gain applied to the MCP in order to increase the number of electrons.

Two different devices were tested: one is an Image Intensifier C9546-01 by Hamamatsu [93], the other is an integrated FGC iStar 334T Series by Andor [94]. The characteristics of the two devices are listed in Table 7.2.

| | Image Intensifier C9546-01 (Hamamatsu) | FGC iStar 334T Series (Andor) |
|---|---|---|
| CCD-Camera | – | Integrated |
| Cooled | No | Yes |
| photo-cathode | | |
| Material | GaAsP | Multi Alkali |
| Spectral Response (nm) | 280-720 | 180-850 |
| Active Area (mm) | 17 | 18 |
| Phosphor | | |
| Material | P43 | P46 |
| Decay Time (µs) | 1500 | 0.2 |
| Resolution Limit (µm) | 7.5 | 13 |
| Gate | | |
| Repetition Rate (kHz) | 10 | 500 |
| Minimum Width (ns) | 3 | <2 |
| Jitter (ns) | 0.5 | 0.035 |

Table 7.2: Characteristics of the FGCs tested at ALBA. More details in [93] and [94].

The Image Intensifier C9546-01 needs to be matched to an external CCD camera to register images. Since this is compatible with the standard CCD cameras and the timing system at ALBA, the device represented an interesting (and economic) solution: unfortunately the results were not satisfactory. Figure 7.19(a) presents the projection of the Interferogram used to obtain the vertical beam size measured with the standard CCD, while Figure 7.19(b) presents the results for the Image Intensifier C9546-01 in non-gated mode and 1 ms exposure time at different gains. The interferogram visibility changes because the fringes get wider and the beam size growth with the intensifier gain, as presented in Fig. 7.20.

FGC iStar 334T Series is a built-in device including a gated Image Intensifier and a fast CCD camera, which are coupled through a fiber optic. It also includes a Digital Delay Generator, which supplies the FGC timing system. Figure 7.19(c) (also obtained in not-gated mode) shows that interferograms are not deformed when changing the gain. Figure 7.20 shows that the measured beam size is not the expected one ($\sigma_y \simeq 25\,\mu\text{m}$), but remains stable: this characteristic is very important because in bunch-by-bunch measurements the light level produced by a single bunch is very low. Due to this optimum linearity with the FGC gain, this system was finally acquired by ALBA.

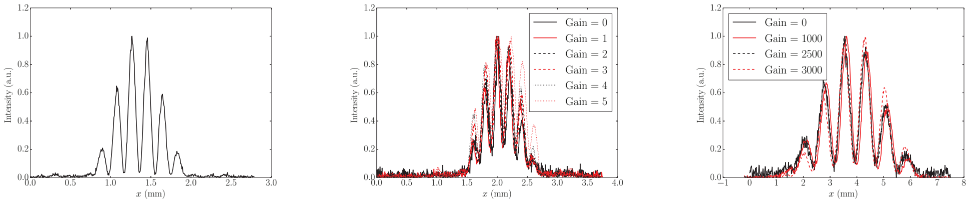

(a) Standard CCD (b) Image Intensifier C9546-01 (c) FGC iStar 334T

Figure 7.19: Interferograms measured with the normal CCD used for SRI (a) and FGC DEMO at different gains (b) and (c).

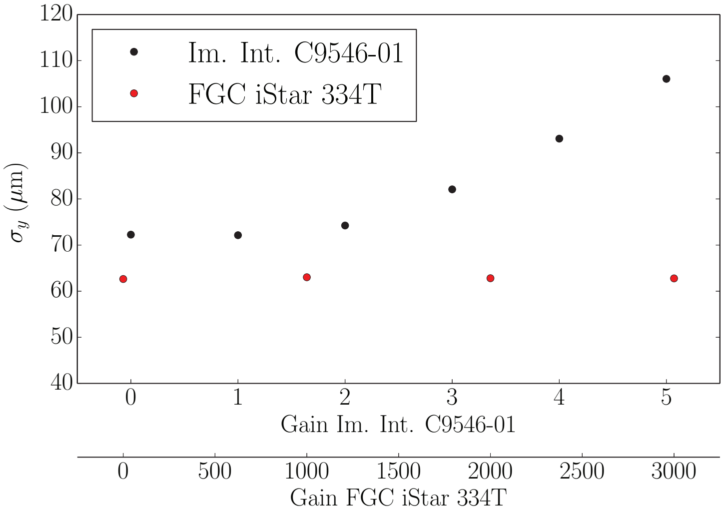

Figure 7.20: SRI beam size measurement using the Image Intensifier C9546-01 (in black) and FGC iStar 334T (in red) as a function of the gain.

### 7.3.2 *Experimental Results*

The interferometer setup used to perform vertical bunch-by-bunch size measurements is the one used for standard application, only substituting the CCD for the

FGC and modifying the pinhole size. Since the pixel size of the FGC is larger than the standard one of the CCD, pinholes with a diameter of 8.5 mm were chosen: in this way the fringes get wider and they are spread over more pixels. Furthermore, wider pinholes leads to a considerable increase of the light intensity.

In any case, the light level produced by a single bunch in a single turn is not enough to produce a meaningful image even at the maximum gain of the iStar 334T. The solution is then to acquire several pictures of the same bunch over different turns and integrate them: for this reason temporal synchronization becomes a crucial point.

Since the maximum gate repetition rate of the FGC camera is 500 kHZ (see Table 7.2) and the machine revolution frequency is $f_0 = 1.116\,\text{MHz}$, the maximum trigger frequency compatible with the FGC is $f^{FGC} = f_0/3 = 371\,\text{kHz}$, i.e. an image of a bunch is taken every third turn.

Figure 7.21 shows a schematic of the FGC synchronization. A trigger from the ALBA timing system is sent to the FGC synchronous with the beam revolution. The trigger reaches the internal delay generator, which generate the gate and the FGC integrated CCD camera. The FGC internal delay generator waits the chosen delay to gate on the appropriate bunch, after the trigger signal. After three turns, the trigger is fired again and the sequence is repeated. The camera starts to acquire synchronous with the trigger and continues for the time selected by the exposure time.

In order to obtain an image from all bunches, the internal delay generator allows to program a sequence in which the gate delay is automatically shifted in steps of 2 ns form 0 to 896 ns (machine revolution period). Furthermore, the gate width is set to 2.5 ns and a previous scan, with a smaller step (10 ps) is performed to crosscheck that the trigger does not fall in the middle of the RF-bucket.

First measurements of the bunch-by-bunch size are shown in Fig. 7.22, corresponding to a beam of 130 mA with a 10-Train Filling Pattern. The FGC exposure time is 100 ms, which becomes a limiting factor for these kind measurements. As explained in Sec. 5.4, an exposure time larger than 1 ms leads to a blurring of the interferogram, due to the mechanical vibrations of the beamline. For this reason, even if the effective exposure time[1] is small ($\simeq 370\,\mu\text{s}$, in this case), the total single shots measured with the interferogram are summed over all the exposure time and the image results blurred.

This effect must be added to the other blurring due to the fringes space charge. Therefore only a qualitative result can be obtained. Figure 7.22 (black dots) presents bunch-by-bunch size measurement during normal operation (10-Trains filling pattern, 130 mA): the vertical size is almost the double with respect the expected one.

The proper vertical bunch size can be obtained by calibrating the FGC results. For this reason, measurements at different couplings were performed, using a standard CCD and the FGC and the linearity between the two measurements is crosschecked.

---

[1] The effective exposure time (EET) is defined as the gate width (GW) multiplied by the number of pulses ($N_p$) contained in the CCD exposure time (ET), when triggered at a given frequency ($f_T$):

$$\text{EET} = GW \times N_p \qquad\qquad N_p = \text{ET} \times f_T$$

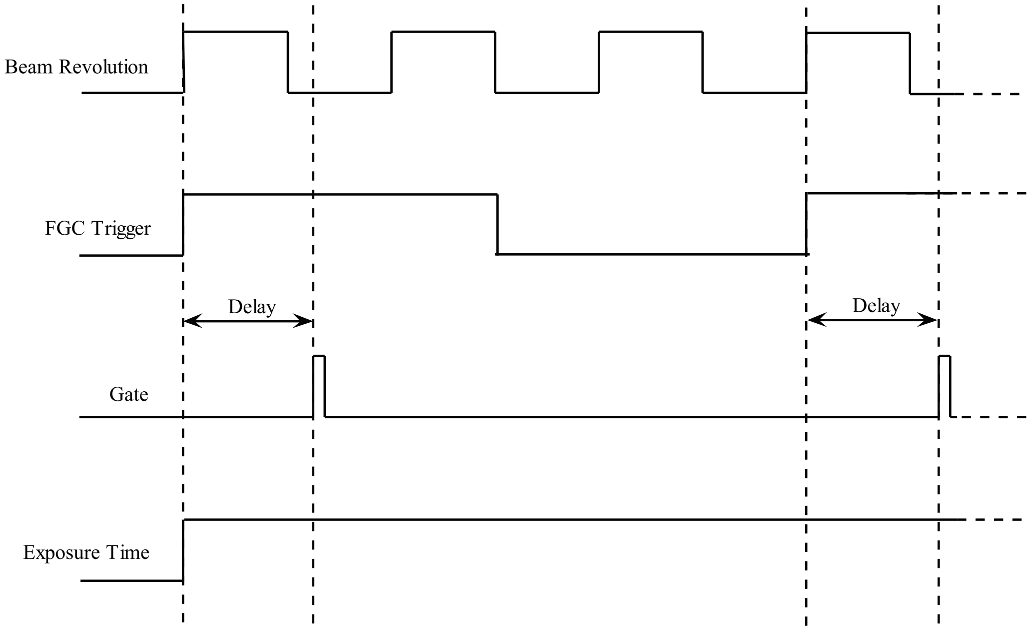

Figure 7.21: Scheme of the FGC synchronization. The first pulse from the top is the beam revolution. The FGC is triggered using a signal synchronous with the beam revolution $f_0 = 1.116\,\text{MHz}$, which has a frequency of $f^{FGC} = f_0/3 = 371\,\text{kHz}$. The gate has a pulse width of 2.5 ns and is synchronous with the FGC trigger, up to a delay that can be moved by a delay generator internal to the FGC. The camera exposure time is also triggered by the FGC trigger and all the pulses collected during exposure time are integrated on the chip.

The $\sigma_y^{FGC}$ was estimated as an average over the measured bunch sizes and the standard deviation is used as error bar. The result, presented in Fig. 7.23, shows that the relation between $\sigma_y^{FGC}$ and $\sigma_y^{CCD}$ is linear. The calibration is inferred by performing a linear fit of the data.

The bunch by bunch results after the calibration are presented by red dots in Fig. 7.22: their average value is $(27 \pm 7)\,\mu\text{m}$, which is compatible with the vertical beam size provided by LOCO that day. The huge fluctuation is due to the large FGC exposure time.

### 7.3.3 *Observation of Transverse Coupled-Bunch Instabilities*

This bunch by bunch size measurement system paves the way towards proper studies of CBI. The consequence of these instabilities is typically to excite oscillation modes along the train of bunches: these modes lead to a rigid transverse oscillation of the bunches since they enter off-center in the focusing magnetic elements and a cause beam size growth.

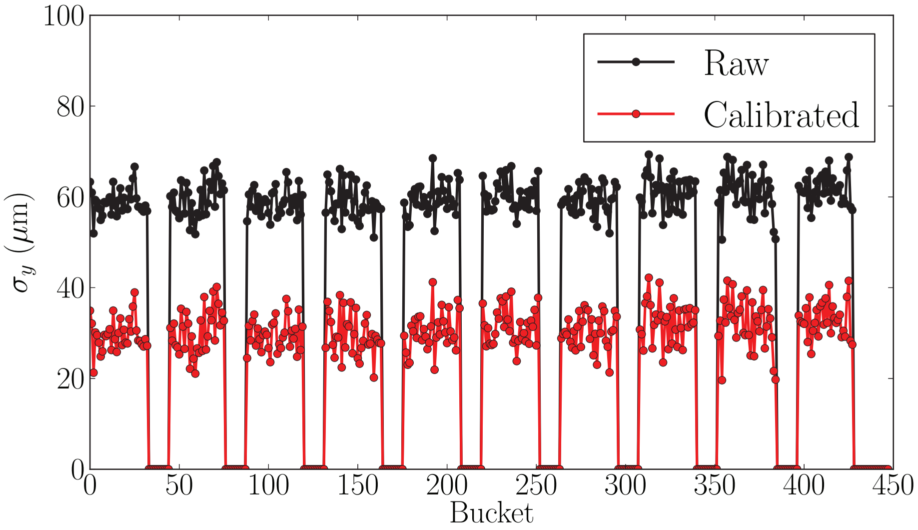

Figure 7.22: Measurement of the vertical size of all the bunches during normal operations, with a beam current of 130 mA and a standard 10-Train filling pattern. Direct results from the FCG in black, while results after the calibration are in red.

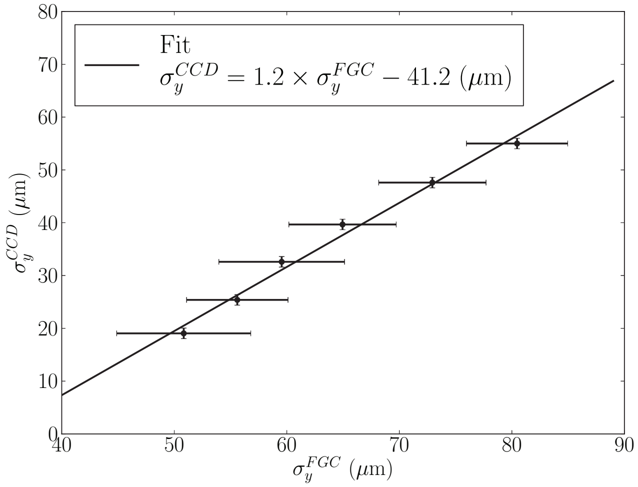

Figure 7.23: Results for the FGC at different coupling as a function of the same measurements performed using a standard CCD.

Fig. 7.24 shows beam size results using the X-rays pinhole, when changing the machine chromaticity. The storage ring was filled with 130 mA and operating in Top-Up mode. Bunches were distributed in a hybrid filling pattern: 320 bunches in a single train (125 mA) and a single bunch of 5 mA at RF-bucket 400. Vertical beam size measurements using the X-rays pinhole (pink line) show a sudden beam size growth from 29 µm up to 120 µm, when the sextupoles current (for example red line) is decreased to change the chromaticity from $\xi = 4.5$ to $\xi = 3.5$. When using the pinhole, the beam size corresponds to the average value of the 321 bunches.

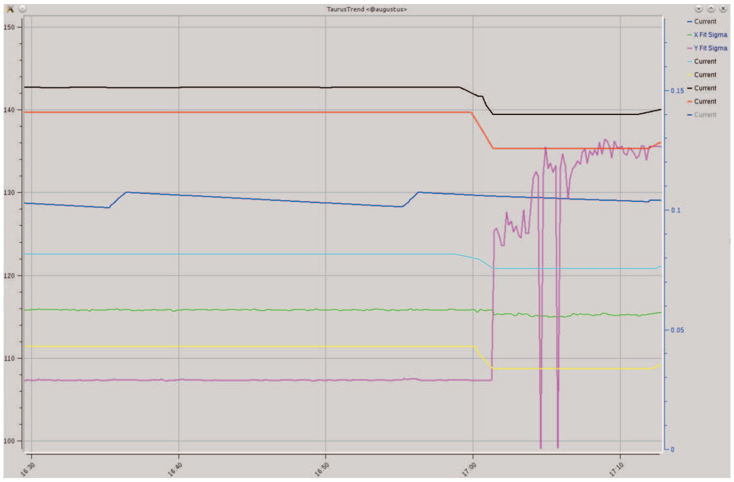

Figure 7.24: X-rays pinhole beam size measurements (vertical in pink and horizontal in green) when decreasing the sextupoles current to low the chromaticity (black, red, light blue and yellow line). The blue line represents the evolution of the current in the storage ring,

Figure 7.25 shows the bunch-by-bunch size measurements using the SRI setup with the FGC. For the nominal chromaticity $\xi = 4.5$ all the bunches have a similar beam size (black dots). On the other hand, when lowering the chromaticity to $\xi = 3.5$, the bunch size gradually grows along the train, until, at around RF-bucket number 130, a modulation arises: the bunch size shows a fast growth rising in around 10 RF-buckets (i.e. RF-buckets 250-260) and a slower decay of $\simeq$ 20 RF-buckets (i.e. between RF-buckets 260-280). The size of the single bunch at RF-bucket 400 remains unchanged, indicating that an interval of 80 RF-buckets is a sufficient gap to damp the instability.

While the linear increase of the bunch size evolution in Fig. 7.25 up to RF-bucket $\simeq 130$ seems to indicate a Resistive Wall instability (purely related to the interaction of the beam with the surrounding vacuum chamber wall), the modulation present between RF-buckets 130 and 320 points towards the presence of Fast Ion Instabilities (related to the interaction between the beam and the residual gas in the vacuum chamber). This mixture of instabilities were already observed at Soleil [91] but could not be precisely analyzed due to a lack of diagnostics.

The bunch-by-bunch size measurement set-up (SRI+FGC) presents a new tool, which allows for instance the study of the internal dynamics of these phenomena. Currently, further studies are being carried out with this set-up to precisely understand the observed instabilities [95].

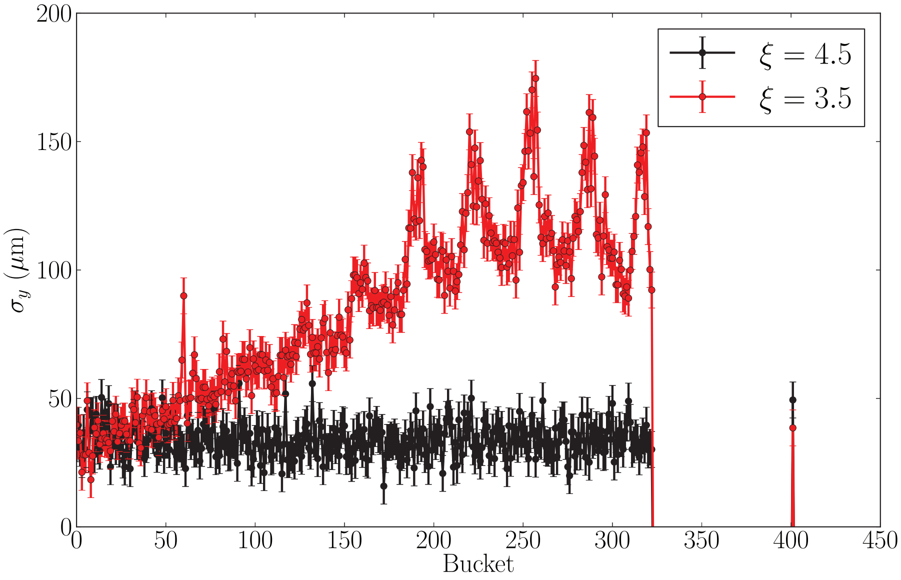

Figure 7.25: Vertical bunch size of all the bunches of the filling pattern at $\xi = 4.5$ (black dots) and $\xi = 3.5$ (red dots).

# CONCLUSIONS

> There is a crack in everything
> That's how the light gets in
>
> Leonard Cohen

The object of this PhD thesis was the development of synchrotron radiation diagnostics tools to obtain a better characterization of the ALBA electron beam. In particular, two fully operative beam diagnostics systems were set up: one to infer the machine Filling Pattern (FP) and another to measure the transverse beam size. Improvements on the state of art of these tools and further applications were proposed, implemented and successfully tested.

In order to monitor the machine FP, the Time Correlated Single Photon Counting (TCSPC) technique was developed at ALBA. Two different photon detectors for two different wavelength ranges were tested: in the visible range the Photomultiplier (PMT) Hamamatsu H10721-201, while in the X-rays range, the Avalanche Photo-Diode (APD) C5658, also from Hamamatsu.

Specific feasibility studies were performed for the two detectors to properly design and locate the experimental stations inside the tunnel. A characterization of both detectors was performed in-house. A method to measure the detectors Transit Time Spread (TTS) was proposed using the ALBA machine operating in single bunch. Furthermore, the APD efficiency for X-rays of 8 keV was measured at the XALOC beamline and found to be $10^{-5}$. Even though this APD was used in other Synchrotron Light Sources, its efficiency for X-rays was still unknown.

The PMT was found to be more appropriate for the daily application of FP measurements at ALBA. It has a shorter TTS than the APD (0.09 ns and 0.47 ns, respectively) and allows a fast FP measurement with an optimum dynamic range ($10^3$) for the current ALBA operation mode. This measurement system is routinely used in the ALBA Control Room and its implementation paved the way for the new "Single Bunch Bucket Selection" (SBBS) operation mode, which can be used to shape specific FPs or to perform "selective Top-Up" by refilling the emptiest bunches and obtain a flat FP. SBBS and selective Top-Up were successfully commissioned during the period of this thesis. Other applications, like the measurement of a single bunch life-time were also demonstrated.

On the other hand, the high Signal to Noise Ratio (SNR) of the APD when using X-rays allows to perform clean single bunch measurements. The TTS and the shape of the single bunch distribution (slightly larger than an ALBA RF-bucket), made the APD not appropriate for FP measurements, since consecutive bunches resulted mixed. However, high dynamic ranges to measure the single bunch (in the order of $10^6$) can be achieved. This high dynamic range is required only for time resolved experiments, which currently are not in the scope of the ALBA facility.

In parallel, a reliable set-up to measure the transverse beam size was developed using the Synchrotron Radiation Interferometry (SRI) in the ALBA diagnostic beamline Xanadu. A careful analysis of the SRI theory showed how the limitation of this technique is due to mirrors flatness. The full beamline was upgraded using mirrors with a flatness better than $\frac{\lambda}{8}$ for the in-vacuum mirror and $\frac{\lambda}{10}$ for the in-air mirrors. In all cases, a precise characterization was done in-house using a Fizeau interferometer and furthermore, in order to monitor possible mirror degradations at any time, a Hartmann Mask was installed and tested.

Following the SRW simulations and in agreement with the experimental evidences, the ALBA SRI set-up uses pinholes instead of rectangular slits (which are more commonly used in accelerators). The beam size is monitored on-line using a fitting algorithm. However, due to the optical path changes related with vibrations, it is not possible to increase the CCD exposure time to improve the SNR of the interferograms. This initially limited the SRI beam size measurements to beam current larger than $\simeq$ 60 mA. This limitation was overcome with the development of a "Matching Algorithm", which was originally developed to increase the SNR of astronomical images and now, for the first time, was applied for accelerators beam size measurements. The algorithm overlaps images with a low SNR to properly reconstruct the interferogram and infer the beam size. With this technique, beam sizes for current down to 3 mA were measured.

Once the SRI technique was reliably implemented, further improvements were developed. In particular a method to fully reconstruct the transverse beam shape by rotating the double-pinhole mask was successfully developed and tested. The method allows to measure, using the SRI, all the geometrical beam ellipse parameters (horizontal and vertical beam size and the beam tilt). It was demonstrated, via SRW simulations, that the same technique can be used to perform ultra-low beam size measurements (down to 2 µm), which can be of great help for the future light sources like ESRF-II (France) or Sirius (Brazil).

Finally, the SRI set-up was upgraded substituting the standard CCD camera with a Fast Gated Camera (FGC) to measure the beam size in a bunch-by-bunch basis for the first time in 3rd generation Synchrotron Light Sources. Applications of this system include the observation of the beam size increase along the bunch train due to Coupled Bunch Instabilities. This provides the community with a new diagnostic tool to study the internal dynamics of these phenomena. At ALBA, the possibility of having both Resistive Wall and Ion Cloud instabilities was shown using this system.

## Part I

# APPENDIX

# A

# BEAM DYNAMICS AND SYNCHROTRON RADIATION

In Synchrotron Light Sources (SLS), beam particles are required to maintain a constant energy and specific longitudinal and transverse characteristics so to provide photon beams as required from experiments.

The beam energy and time distribution are result of the Radio-Frequency cavities (RF), while its characteristics in the transverse plane depends on the accelerator magnets lattice. In general it is essential to monitor the beam characteristics in real time, to optimize the machine performances.

A full introduction on the accelerator physics can be found in [30].

## A.1 REFERENCE FRAME AND NOTATION

The standard reference frame used to describe the trajectory of the particles in these machines is presented in Fig. A.1. $x$ and $y$ are the transverse coordinates, in particular $x$ (horizontal) lays on the orbit plane, and $y$ (vertical) is orthogonal, while $z$ follows the particle motion and simply represents the longitudinal position along the accelerator.

In accelerator physics, since electrons circulating in the machine travel nearly at the speed of light $c$, $z$ is often indicated by $s$, which is defined as

$$s = ct. \tag{A.1}$$

Therefore, space derivation corresponds to time derivation: $ds = cdt$ and all the dynamic equation describing the motion of the particles are expressed in terms of space.

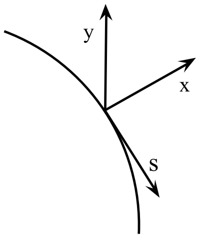

Figure A.1: Reference Frame used in circular accelerators: $x$ and $y$ are the transversal coordinates while $s$ is the longitudinal.

In particular when describing the motion on the transverse plane, the transverse velocities of a particle are defined as

$$x' = \frac{dx}{ds} \qquad\qquad y' = \frac{dy}{ds}. \tag{A.2}$$

$x'$ and $y'$ are dimensionless and represents the angular deviation (or divergence) with respect to the ideal trajectory given by the planar, close, and circular orbit.

## A.2 LONGITUDINAL BEAM STRUCTURE

In particle accelerators RF cavities are mainly used to accelerate the beam [30, 96]. RF cavities are metallic chambers containing an electromagnetic field, provided by an RF power supply feeding the cavity, which is designed with a specific shape resonant at a given frequency. The electromagnetic field oscillates inside the cavity at this frequency and if a charged particle arrives in the accelerating structure at the proper time, it experiences a voltage difference which increases its energy. This is the so called *Synchronous Particle*.

If $V$ is the maximum voltage in the cavity and $\Phi$ is the phase at which a particle of charge $q$ enters, the acquired energy $E$ is given by

$$E = qV \sin \Phi. \tag{A.3}$$

In a real beam not all the particles have the nominal energy, but all of them have the same revolution period. In SLS machines, which operate "above transition", higher energy particles run on a longer orbit with respect to the synchronous particle, and will arrive later in RF cavity experimenting a lower accelerating voltage. On the other hand, particles having a lower energy will arrive before and will acquire more energy. This provokes a longitudinal focusing effect, which compacts the bunch.

The process is sketched in Fig. A.2, where a high energy particles is indicated as "Late Particles" while a low energy one is the "Early Particle". The synchronous particle is the "Stable Particle".

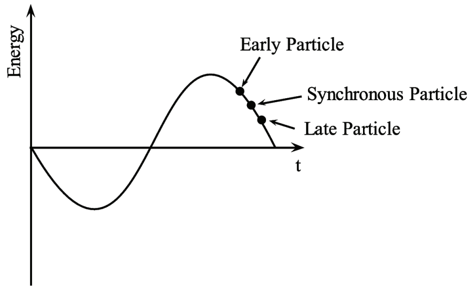

Figure A.2: Energy gained by particles in a RF-cavity as a function of arrival time. "Early Particles" arrive before since they are less energetic with respect to the "Synchronous Particle", and run along a shorter orbit. In this way they gain more energy. "Late Particles", which are more energetics and run over a longer orbit arrive later and gain less energy.

RF cavities also define the longitudinal structure of the beam in the accelerator: particles that arrives far from the Synchronous Particle may also be decelerated and get lost. Only particles arriving within a proper time interval $\Delta t$, and with an energy spread lower than a proper $\Delta E$ can be accelerated.

The phase space enclosed in $(\Delta t, \Delta E)$ is called *RF-Bucket* and define the momentum acceptance of the machine. In each RF-bucket it is possible to host a single bunch. These intervals also provide the shape of the longitudinal structure of the beam, i.e. the bunch length. The temporal length of a RF-buckets is identified with the RF period of the machine, which is the maximum distance between two consecutive bunches.

Moreover circular accelerators have a larger revolution with respect to the RF period. Thus, several bunches can be accommodated in different RF-buckets, and can be accelerated simultaneously. The distance between two consecutive bunches is given by the RF period.

The choice of the RF frequency $f_{RF}$ and of the beam revolution frequency $f_{rev}$ fixes the *Harmonic Number* $h$:

$$h = \frac{f_{RF}}{f_{rev}}. \tag{A.4}$$

The harmonic number $h$ defines the number of RF-buckets of the machine that can be accelerated simultaneously.

In general not all the RF-buckets must be filled: the distribution of the bunches among the RF-buckets, is called *Filling Pattern*. The best choice of the filling pattern depends from the experimental purpose of the accelerator and from beam stability considerations.

## A.3 TRANSVERSE BEAM DYNAMICS

In particle accelerators the beam dynamic is determined by the magnet lattice, defining the so called *Machine Parameters*. From these parameters one can infer the transverse particle distribution along the machine [30, 97].

When a charged particle is traveling in an accelerator, it experiences a force due to the magnetic and electric field. The equation of motion for the transverse coordinates is given at the leading order by the *Hill Equation*:

$$u'' = -k(s)u, \tag{A.5}$$

where $u$ is either $x$ or $y$, $k(s)$ describes the applied force at a given $s$, and $u'' = \frac{d^2u}{ds^2}$. $k(s)$ is completely determined by the magnets and it is known at every point of the machine.

The solution of the Hill Equation gives the transversal position of the particle with respect to the Synchronous Particle's orbit and can be expressed as an oscillating function:

$$u(s) = A\sqrt{\beta(s)}\cos\varphi(s). \tag{A.6}$$

where $A$ describes the amplitude dependence on the initial conditions related with a given particle, while $\beta(s)$ and $\varphi(s)$ describe the amplitude and the phase dependence of the transverse oscillation at a given $s$.

These oscillations of the particle in the transverse plane are called *Betatron Oscillations*. The parameters describing the Betatron oscillations, $\alpha(s)$, $\beta(s)$, and $\gamma(s)$, are the *Twiss Parameters* and are essential to understand the behavior of the beam.

$\beta(s)$ is the same of the Hill Equation solution (Eq. A.6), moreover $\alpha(s)$ and $\gamma(s)$ are defined such that:

$$\tan(2\phi(s)) = \frac{2\alpha(s)}{\gamma(s) - \beta(s)}. \tag{A.7}$$

Finally they fulfill the following relations:

$$\alpha(s) = -\frac{1}{2}\frac{d\beta(s)}{ds} \qquad \gamma(s) = \frac{(1+\alpha^2(s))}{\beta(s)} \tag{A.8}$$

Twiss parameters and Eq. A.6 can be used to find the equation governing the phase space trajectory and construct a constant of motion. The result can be expressed as an ellipse in the phase space:

$$\gamma(s)u^2 + 2\alpha(s)uu' + \beta(s)u'^2 = A^2, \tag{A.9}$$

where $A$ is the same as Eq. A.6, and $\pi A^2$ represents the area of the phase space ellipse, which is independent from $s$. This means that the ellipse changes its shape along $s$ but maintaining its area constant.

Equation A.6 refers to a single particle oscillating with a maximum amplitude given by

$$\Xi(s) = A\sqrt{\beta(s)}. \tag{A.10}$$

To consider all the particles in the beam usually one set as maximum amplitude of the oscillation, $\Xi(s)$ as the beam size $\sigma(s)$, and defines the beam *emittance* as $\varepsilon = A^2$. Substituting the definition of emittance in Eq. A.10 one obtains the following relation between the emittance and the beam size:

$$\sigma(s) = \sqrt{\varepsilon\beta(s)}. \tag{A.11}$$

Note that since $\varepsilon$ is a constant of motion, and $\beta(s)$ changes along the machine, the beam size along the machine position $s$, also changes.

A graphical representation of the phase space ellipse with the results for the meaningful point as a function of the Twiss Parameters is presented in Fig. A.3.

The emittance and the Twiss parameters are defined independently for the $(x, x')$ and in the $(y, y')$ phase space, and a different emittance for each direction can be calculated.

Equation A.11 shows that the emittance $\varepsilon$ on an accelerator is inferred from the beam size at a given position $s$, since the value of $\beta(s)$ is known form the machine lattice with a good accuracy (at ALBA usually this is $\simeq 1\%$).

However the dispersion in the bending magnets adds a further component to Eq. A.11 in the horizontal plane. A further spread in their position is generated due to the energy spread $\frac{\Delta E}{E}$:

$$\sigma_x(s) = \sqrt{\varepsilon\beta_x(s) + \left(\mathcal{D}_x(s)\frac{\Delta E}{E}\right)^2} \tag{A.12}$$

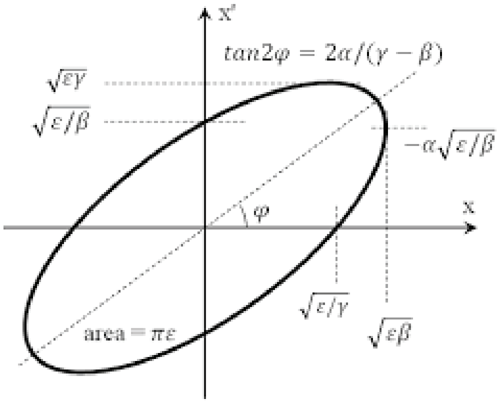

Figure A.3: Phase Space ellipse with the expressions of the meaningful points as a function of the Twiss parameters.

where $\mathcal{D}_x(s)$ describes the dispersion at the location $s$.

In light sources the $x$ and the $y$ directions are never completely independent due to the not perfect alignment of the magnets in the lattice. To define how much the two components are coupled one defines the machine *coupling*, $\mathcal{K}$ as

$$\mathcal{K} = \frac{\varepsilon_y}{\varepsilon_x}. \tag{A.13}$$

## A.4 SYNCHROTRON RADIATION

Synchrotron radiation is produced when a relativistic charged particle is accelerated radially. The derivation of the theory is completely classical and can be found in [10, 65, 98].

The power distribution can be parametrized as a function of the frequency of the produced radiation $\omega$, and the emission angle with respect to the orbit plane $\psi$. In literature these two parameters are usually presented normalized by others that depends from the characteristics of the machine which produces the radiation.

The radiation frequency is usually expressed in terms of the so called "critical frequency" $\omega_c$:

$$\omega \longrightarrow \frac{\omega}{\omega_c} \qquad\qquad \omega_c = \frac{3c\gamma^3}{2\rho}, \tag{A.14}$$

where $c$ is the speed of light, $\gamma$ is the Lorentz factor, and $\rho$ is the giro-radius of the particle inside the magnet where the radiation is produced. Physically, $\omega_c$ is the frequency dividing the synchrotron radiation spectrum in two parts of equal areas.

The emission angle is instead multiplied by the Lorentz factor $\gamma$:

$$\psi \longrightarrow \gamma\psi \qquad\qquad \gamma = \frac{E}{mc^2} \tag{A.15}$$

where $E$ and $m$ are respectively the energy and mass of the beam particles.

Using this parametrization, the power distribution of emitted radiation is given by:

$$\frac{dP_{ob}}{d\frac{\omega}{\omega_c}d\gamma\psi} = P_T\left(F_\sigma\left(\frac{\omega}{\omega_c},\gamma\psi\right) + F_\pi\left(\frac{\omega}{\omega_c},\gamma\psi\right)\right) \tag{A.16}$$

where $P_T$ is the total power emitted by the beam in the rest frame, and $F_\sigma\left(\frac{\omega}{\omega_c},\gamma\psi\right)$ and $F_\pi\left(\frac{\omega}{\omega_c},\gamma\psi\right)$ are distribution functions respectively for the emission of the $\sigma$ and the $\pi$ polarized radiation, defined as:

$$F_\sigma(\omega,\psi) = \frac{9}{2\pi}\left(\frac{3}{4}\frac{\omega}{\omega_c}\right)^{\frac{2}{3}} Ai'^2\left(\left(\frac{3}{4}\frac{\omega}{\omega_c}\right)^{\frac{2}{3}} + (1+\gamma^2\psi^2)\right) \tag{A.17}$$

$$F_\pi(\omega,\psi) = \frac{9}{2\pi}\left(\frac{3}{4}\frac{\omega}{\omega_c}\right)^{\frac{4}{3}} \gamma^2\psi^2 Ai^2\left(\left(\frac{3}{4}\frac{\omega}{\omega_c}\right)^{\frac{2}{3}} + (1+\gamma^2\psi^2)\right) \tag{A.18}$$

where $Ai$ and $Ai'$ are respectively the Airy Function and its derivative.

Figure A.4 presents the functions described in Eq. A.17, and A.18 and their sum contained in Eq. A.16 for the ALBA case. It is worth to notice that the distribution of the $F_\sigma$ is different for the one of $F_\pi$. In particular, most of the produced radiation is $\sigma$-polarized and lays on in a narrow cone of the orbit plane (Fig. A.4(a)). On the other hand, the distribution of the radiation produced with a $\pi$-polarization has a zero on the orbit plane and its intensity is much lower with respect to the $\sigma$-polarized one (Fig. A.4(b)). In general the spectrum of the emitted radiation is broad, and directed forwards.

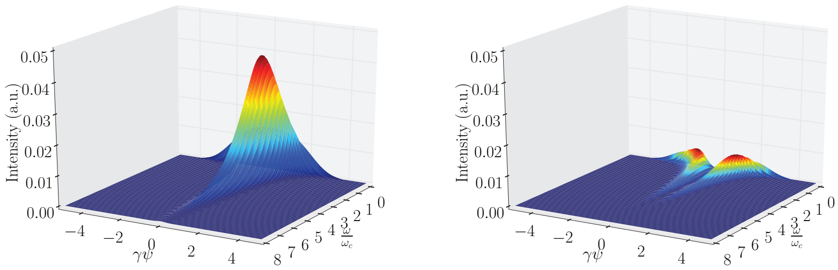

(a) $F_\sigma(\omega, \psi)$ (b) $F_\pi(\omega, \psi)$

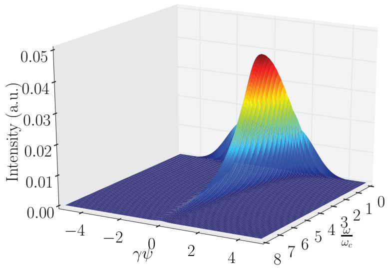

(c) $F_\sigma(\omega, \psi) + F_\pi(\omega, \psi)$

Figure A.4: $F_\sigma$ and $F_\sigma$ functions described in Eq. A.17, and A.18 and their sum contained in Eq. A.16. The frequency axis is normalized to the critical frequency $\omega_c$, and the emission angle axis is multiplied by the Lorentz factor $\gamma$.

# B

# SIGNAL INVERSION SYSTEM

The Picoharp300 needs as input negative pulses of amplitude between 0 and -1 V with a rise-time shorter than 2 ns. Rather than designing a circuit to invert the C5658 Avalanche-PhotoDiote (APD) signal, which will also attenuate it and decrease the signal to noise ration because of the small pulse width ($\simeq 1$ ns), it is decided to generate the negative pulses using the Digital Delay Generator DG645, triggered by the APD output signal.

When a photon is detected by the APD, its output signal acts as trigger of the DG645, which in term produces a negative pulse of -600 mV, width of 10 ns, and rise time of 1.5 ns (see Fig. B.1). This is the pulse which the Picoharp300 will be counting for the TCSPC process.

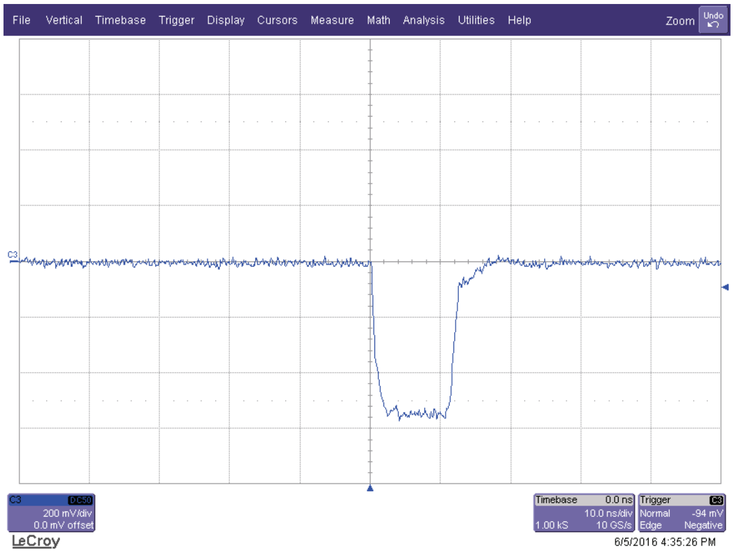

C3 DC50
200 mV/div
0.0 mV offset

Timebase 0.0 ns
10.0 ns/div
1.00 kS 10 GS/s

Trigger C3
Normal -94 mV
Edge Negative

6/5/2016 4:35:26 PM

Figure B.1: Pulse produced by the DG645 observed at the oscilloscope.

In order to crosscheck that the conversion system does not affect the temporal resolution of the TCSPC measurements, the time jitter between two channels of the same function generator are measured with and without the pulse conversion of the DG645. Figure B.2 presents a sketch of the setup. The first channel of the function generator (Ch. 1) produces a squared negative pulse, with an amplitude of -600 mV, and a frequency of 1 MHz used to trigger the Picoharp300. The second channel of the function generator (Ch.2) generates a squared pulse with an absolute amplitude of 600 mV, and different frequencies. The pulse can be connected directly with the Picoharp300 (using a negative polarity, sketch A Fig. B.2), or can trigger the DG645 (using a positive polarity, sketch B Fig. B.2) to produce the negative polarity signal to be sent to the photon counter. The comparison between the width of the two results provides the temporal jitter introduced by the DG645 when producing the desired pulse.

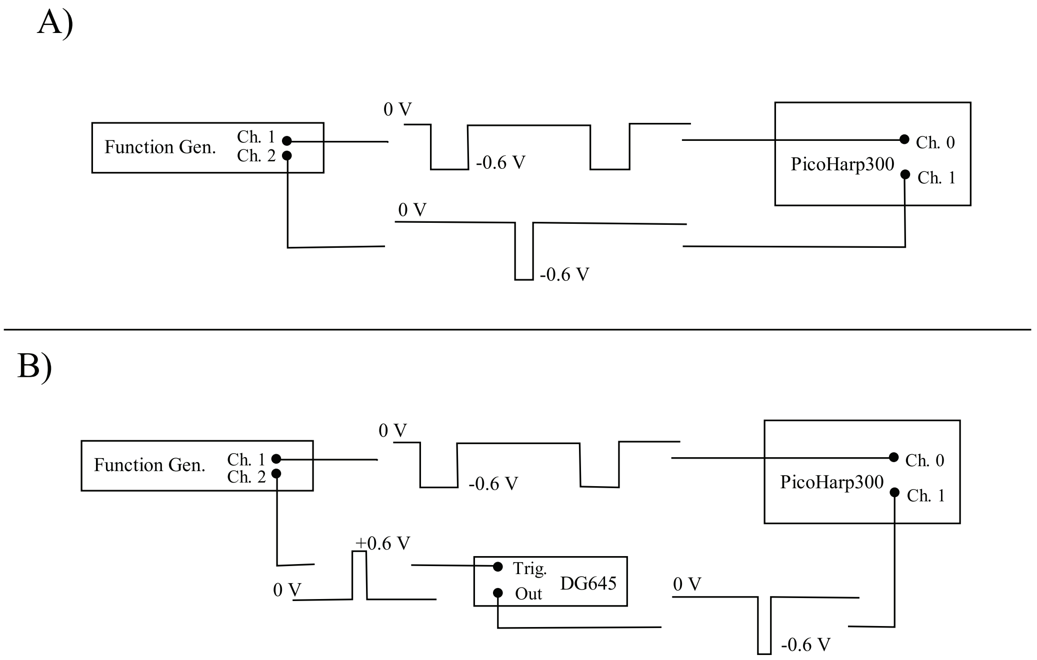

Figure B.2: Sketch of the TTS measurement of the DG645. The top diagram (sketch A) presents the setting to measure the temporal spread between the two channels of the function generator. In the bottom diagram (sketch B) the same measurement is performed, inverting the signal from the Ch. 2 of the function generator using the DG645.

Results are presented in Fig. B.3. The black solid line is the jitter measured directly connecting the Ch. 2 of the function generator to the Picoharp300 (sketch A in Fig. B.2), while dashed lines represent the same measurements using inverting the signal using the DG645 (sketch B in Fig. B.2). Although the function generator has an internal jitter, the width of the signal does not change significantly after passing through the DG645.

Another important element in this case is that the total number of counts stays constant, in order to be sure that the DG645 fires a signal for each trigger. Figure B.4 shows the number of signals counted when the function generator is directly connected to the Picoharp300 and when the pulses are inverted by the DG645. The number of signals is the same for both the measuring techniques.

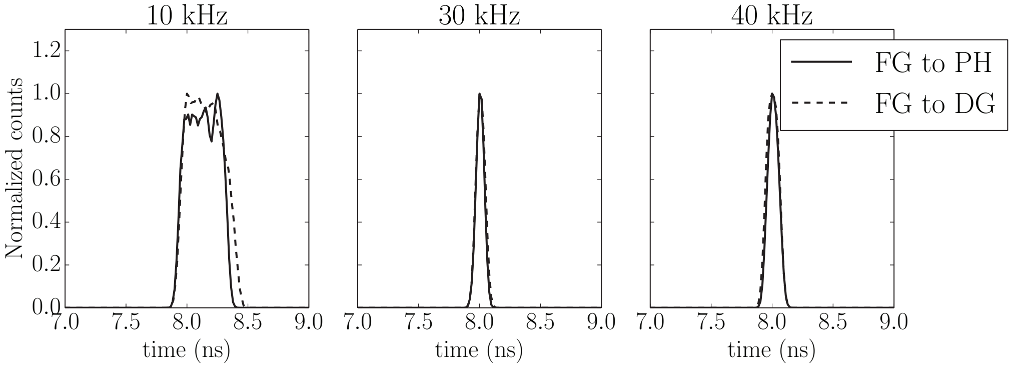

Figure B.3: Jitter of the signal generated by the function generator, with and without inverting the signal using the DG645. The black solid line is the signal directly plugged from the function generator (FG) to the Picoharp300 (PH), while the dashed line is the same signal passing through the DG645 (DG).

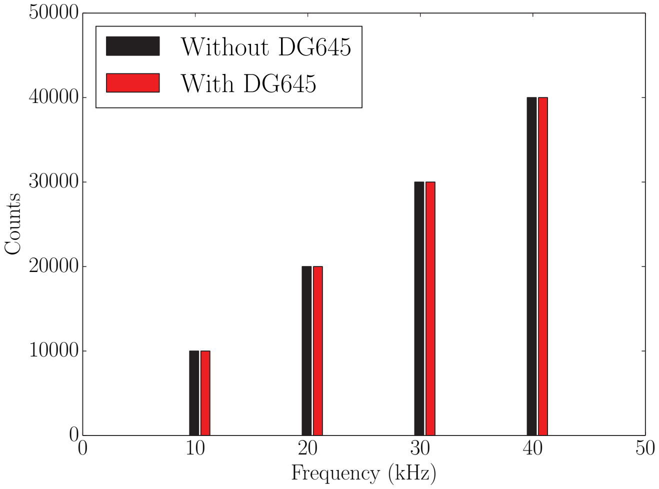

Figure B.4: Number of pulses counted reaching directly the Picoharp300, without the DG645, and the ones counted after being inverted by the DG645 at different frequencies.

# C

# CARBON-LIKE-DIAMOND STUDIES

Experiments were performed together with the ALBA Experiments group to understand the nature of the growth on the in-vacuum mirror. Results from a Raman scattering experiment shows that the growth is compatible with a nano-crystalline carbon-like-diamond structure. The results are show in Fig. C.1 together with results published in literature [99]. The peak at $1332\,\mathrm{cm}^{-1}$ is typical of the diamond and the one present at $1550\,\mathrm{cm}^{-1}$ is typical of carbon. The total structure is comparable with the footprint of nano-crystalline carbon-like-diamond. Further studies will be performed to understand the nature of the growth and prevent it if possible.

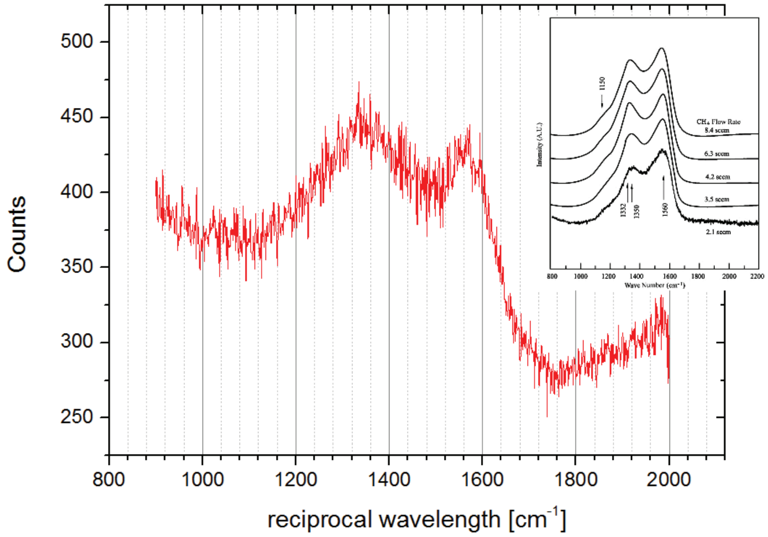

Figure C.1: Raman spectrum of the old Xanadu mirror (in red) and spectra taken from the literature (inserted) [99].

# BIBLIOGRAPHY

[1] M. Pont. Operation status of alba synchrotron light source. *Conf.Proc.*, C1205201: 1659–1661, 2012. (Cited on pages xi, 2, and 3.)

[2] L. Torino and U. Iriso. Charge Distribution Measurements at ALBA. *Conf.Proc.*, 2013. (Cited on pages xi, 6, 8, and 40.)

[3] C.A. Thomas, G. Rehm, H.L. Owen, N.G. Wyles, S.W. Botchway, et al. Bunch purity measurement for Diamond. *Nucl.Instrum.Meth.*, A566:762–766, 2006. doi: 10.1016/j.nima.2006.07.059. (Cited on pages xi, 15, 25, and 26.)

[4] F. Fernàndez and U. Iriso. Measurements of the sr pinhole apertures. ALBA Project Document No. AAD-SR-DI-XSR-01, 2011. (Cited on pages xi and 11.)

[5] T. Mitsuhashi. Measurement Of Small Transverse Beam Size Using Interferometry. *DIPAC*, 2001. (Cited on pages xii and 53.)

[6] O. Chubar and P. Elleaume. Accurate and efficient computation of synchrotron radiation in the near field region. *Conf. Proc.*, C980622:1177–1179, 1998. (Cited on pages xii and 67.)

[7] lightsources.org. `http://www.lightsources.org/`. (Cited on page 1.)

[8] Doug Vaughan Al Thompson. *X-ray data booklet*. Lawrence Berkeley National Laboratory, 2001. `http://xdb.lbl.gov/xdb.pdf`. (Cited on pages 1, 26, and 27.)

[9] Hermann Winick. *Synchrotron radiation sources: A primer*. World Scientific, Singapor; River Edge, 1995. (Cited on page 1.)

[10] J. A. Clarke. *The Science and Technology of Undulators and Wigglers*. Oxford Science Publication, 1st edition, 2004. (Cited on pages 1, 15, and 117.)

[11] MAX IV. `https://www.maxiv.lu.se/`. (Cited on page 2.)

[12] D. Einfeld. Alba synchrotron light source commissioning. *Conf.Proc.*, C110904:1–5, 2011. (Cited on page 2.)

[13] D. Einfeld. Alba synchrotron light source commissioning. *Conf.Proc.*, C110904:1–5, 2011. (Cited on page 3.)

[14] G. Benedetti, D. Einfeld, Z. Martí, M. Munoz, and M. Pont. Optics for the alba booster synchrotron. *Conf.Proc.*, C0806233:WEPC067, 2008. (Cited on page 2.)

[15] D. Einfeld, E. Al-Dmour, Munoz M. Campmany, J.and, F. Pérez, and M. Pont. Progress With The Synchrotron Light Source ALBA. *ALBA Technical Note*, 2005. (Cited on page 2.)

[16] M. Munoz, G. Benedetti, D. Einfeld, and Z. Marti. Alternative Lattice Settings for ALBA Storage Ring. *Conf.Proc.*, C0806233:WEPC045, 2008. (Cited on page 2.)

[17] F. Perez, B. Bravo, P. Sanchez, and A. Salom. Commissioning of the alba storage ring rf system. *Conf.Proc.*, pages 178–180, 2011. (Cited on page 4.)

[18] M. Munñoz and D. Einfeld. Optics for the ALBA lattice. *Conf. Proc.*, MPPE069, 2005. (Cited on page 4.)

[19] P. Forck. Lecture Notes on Beam Instrumentation and Diagnostics. *Joint University Accelerator School January*, 2006. (Cited on page 5.)

[20] U. Iriso, A. Olmos, and F. Pérez. Electron Beam Diagnostics for the ALBA Light Source. *DIPAC*, 2007. (Cited on page 5.)

[21] U. Iriso, M. Álvarez, F. Fernández, F. Pérez, and A. Olmos. Diagnostic During the ALBA Storage Ring Commissioning. *DIPAC*, 2011. (Cited on pages 5 and 6.)

[22] F. Perez, A. Olmos, and T. F. Gunzel. BPM design for the ALBA synchrotron. *Conf. Proc.*, C060626:1190–1192, 2006. (Cited on page 6.)

[23] A. Olmos, J. Moldes, S. Blanch, X. Serra, Z. Martí, R. Petrocelli, M. Muñoz, and A. Gutiérrez. First Steps Towards a Fast Orbit Feedback at ALBA. *Conf. Proc.*, WEPC22:727–730, 2013. (Cited on page 6.)

[24] R. Petrocelli Z. Martí D. Yepez S. Blanch X. Serra G. Cuni S. Rubio A. Olmos, J. Moldes. Commissioning Fast Orbit Feedback System at ALBA. *Conf. Proc.*, WEPD23:691–695, 2014. (Cited on page 6.)

[25] J. Moldes F. Perez M. Abbott G. Rehm I. Uzun A. Olmos, U. Iriso. Integration of the Diamond Transverse Multibunch Feedback System at Alba. *Conf. Proc.*, TUPB046:414–417, 2015. (Cited on pages 6 and 44.)

[26] U. Iriso A. Nosych. Studies and Historical Analysis of ALBA Beam Loss Monitors. *Conf. Proc.*, MOPG22, 2016. (Cited on page 6.)

[27] U. Iriso and F. Frenández. Visible Synchrotron Radiation Front End and Beamline for Longitudinal Beam Diagnostic. *ALBA Project Document*. (Cited on page 6.)

[28] U. Iriso and F. Perez. Synchrotron radiation monitors at ALBA. *Conf.Proc.*, C060626:3410–3412, 2006. (Cited on page 6.)

[29] Torino L. Filling Pattern Measurements at ALBA. Master's thesis, Università di Pisa, 2013-07-16. URL `https://intranet.cells.es/Divisions/Accelerators/publications/ACDIV-2013-12`. (Cited on page 8.)

[30] H. Wiedemann. *Particle Accelerator Physics*. Springer, 3rd edition, 2007. (Cited on pages 9, 42, 87, 113, 114, and 115.)

[31] J. Safranek. Experimental determination of storage ring optics using orbit response measurements. *Nucl. Instrum. Meth.*, A388:27–36, 1997. (Cited on pages 9 and 89.)

[32] G. Benedetti, D. Einfeld, Z. Martí, and M. Munoz. LOCO in the ALBA Storage Ring. *Conf. Proc.*, C110904:2055–2057, 2011. (Cited on pages 9 and 89.)

[33] G. Kube. Review of synchrotron radiation based diagnostics for transverse profile measurements. *Conf. Proc.*, MOO1A03:6–10, 2007. (Cited on page 9.)

[34] U. Iriso, M. Alvarez, F. Fernandez, A. Olmos, and F. Pérez. Diagnostics during the ALBA Storage Ring Commissioning. *Conf. Proc.*, TUOA02:280–282, 2011. (Cited on page 10.)

[35] C. Penel P. Elleaume, C. Fortgang and E. Tarazona. Measuring Beam Sizes and Ultra-Small Electron Emittances Using an X-ray Pinhole Camera. *Journal of Synchrotron Radiation*, (2):209–214, 1995. (Cited on page 10.)

[36] M Born and E Wolf. *Principles of Optics*. Cambridge University Press, 7 edition, 1999. (Cited on pages 12, 47, and 52.)

[37] A. Andersson, M. B oge, A. L ideke, V. Schlott, and A. Streun. Determination of a small vertical electron beam profile and emittance at the swiss light source. *Nuclear Instruments and Methods in Physics Research Section A: Accelerators, Spectrometers, Detectors and Associated Equipment*, 591(3):437 – 446, 2008. (Cited on pages 12 and 92.)

[38] A. A. Michelson and F. G. Pease. Measurement of the diameter of alpha Orionis with the interferometer. *Astrophys. J.*, (53):249â259, 1921. (Cited on page 13.)

[39] T. Mitsuhashi. Beam profile and size measurement by SR interferometers. In *Beam measurement. Proceedings, Joint US-CERN-Japan-Russia School on Particle Accelerators, Montreux and Geneva, Switzerland, May 11-20, 1998*, 1998. (Cited on pages 13 and 47.)

[40] Benjamin Kehrer, Andrii Borysenko, Edmund Hertle, Nicole Hiller, Michael Holz, Anke-Susanne MÃ¼ller, Patrik SchÃ¶nfeldt, and Paul SchÃ¼tze. Visible Light Diagnostics at the ANKA Storage Ring. In *Proceedings, 6th International Particle Accelerator Conference (IPAC 2015): Richmond, Virginia, USA, May 3-8, 2015*, page MOPHA037, 2015. (Cited on page 15.)

[41] Jenny Chen C.H. Kuo K.T. Hsu C.Y. Wu, K.H. Hu. Filling Pattern Measurement for the Taiwan Light Source. In *Proceedings, European Particle Accelerator Conference (EPAC 2008): Genoa, Italy, 2008*, page TUPC038, 2008. (Cited on page 15.)

[42] N. Hubert. Purity measurement at soleil. Talk for DEELS 2014, Grenoble (France), 2014. (Cited on pages 15, 25, and 26.)

[43] Jeff A. *A Longitudinal Density Monitor for the LHC*. PhD thesis, Liverpool University, 2012-12-11. URL `http://inspirehep.net/record/1231117/files/CERN-THESIS-2012-240.pdf`. (Cited on page 15.)

[44] T. Obina, T. Kasuga, M. Tobiyama, T. Katsura, and K. Tamura. Measurement of the longitudinal bunch structure in the Photon Factory positron storage ring with a photon counting method. *Nucl. Instrum. Meth.*, A354:204–214, 1995. doi: 10.1016/0168-9002(94)01047-1. (Cited on page 15.)

[45] Stand Alone TCSPC Module with USB 2.0 Interface. *PicoQuant GmbH*, . (Cited on page 15.)

[46] PicoHarp 300, Userâs Manual and Technical Data. *PicoQuant GmbH*, . (Cited on page 15.)

[47] M. Wahl. Time-Correlated Single Photon Counting. *PicoQuant GmbH*. (Cited on page 16.)

[48] Metal Package PMT, Photosensor Modules H10720/H10721 Series. *Hamamatsu*, . (Cited on page 17.)

[49] Photomultiplier Tube R4124. *Hamamatsu*, . (Cited on page 17.)

[50] High Speed Current Amplifier HCA-40M-100K-C Datasheet. *FEMTO*. (Cited on page 17.)

[51] Mounted N-BK7 Reflective Neutral Density Filters. *Throlabs*, . `https://www.thorlabs.de/newgrouppage9.cfm?objectgroup_id=119`. (Cited on page 21.)

[52] Laser Line and Bandpass Filters . *Thorlabs*. `http://www.thorlabs.com/catalogpages/V21/810.PDF`. (Cited on page 21.)

[53] Rectangular, Continuously Variable, Metallic Neutral Density Filters. *Throlabs*, . `https://www.thorlabs.de/newgrouppage9.cfm?objectgroup_id=1623`. (Cited on page 21.)

[54] APD module C5658 series Data Sheet. *Hamamatsu*. `http://www.hamamatsu.com/resources/pdf/ssd/c5658_kacc1023e.pdf`. (Cited on pages 25 and 26.)

[55] Si APD S12023 series Data Sheet. *Hamamatsu*. `http://www.hamamatsu.com/resources/pdf/ssd/s12023-02_etc_kapd1007e.pdf`. (Cited on page 25.)

[56] Shunji Kishimoto. Bunch-purity measurements of synchrotron x-ray beams with an avalanche photodiode detector. *Nuclear Instruments and Methods in Physics Research Section A: Accelerators, Spectrometers, Detectors and Associated Equipment*, 351 (2):554 – 558, 1994. doi: http://dx.doi.org/10.1016/0168-9002(94)91385-4. (Cited on pages 25 and 26.)

[57] T. Obina, T. Kasuga, M. Tobiyama, T. Katsura, and K. Tamura. Measurement of the longitudinal bunch structure in the Photon Factory positron storage ring with a photon counting method. *Nucl.Instrum.Meth.*, A354:204–214, 1995. doi: 10.1016/0168-9002(94)01047-1. (Cited on page 25.)

[58] XOPx2.4. *ESRF*. `http://www.esrf.eu/Instrumentation/software/data-analysis/xop2.4`. (Cited on page 27.)

[59] Transmission Calculator. `http://henke.lbl.gov/optical_constants/filter2.html`. (Cited on page 29.)

[60] Jordi Juanhuix, Fernando Gil-Ortiz, Guifré Cuní, Carles Colldelram, Josep Nicolás, Julio Lidón, Eva Boter, Claude Ruget, Salvador Ferrer, and Jordi Benach. Developments in optics and performance at BL13-XALOC, the macromolecular crystallography beamline at the Alba Synchrotron. *Journal of Synchrotron Radiation*, 21(4):679–689, Jul 2014. doi: 10.1107/S160057751400825X. URL `http://dx.doi.org/10.1107/S160057751400825X`. (Cited on page 31.)

[61] Transmissive photodiode: DDS1-XXXX/X. *ALIBAVA*. `https://computing.cells.es/products/electronics/dds1-photodiode/brochure`. (Cited on page 31.)

[62] F. Pèrez R. Muñoz Horta, D. Lanaia. Status and Operation of the ALBA Linac. *Conf. Proc.*, THOP05, 2016. (Cited on page 40.)

[63] M. Pont, G. Benedetti, J. Moldes, R. Muñoz Horta, A. Olmos, and F. Pérez. Top-up Operation at ALBA Synchrotron Light Source. *Conf.Proc.*, page MOPRO090, 2014. (Cited on page 42.)

[64] A. Glindemann. Optical interferometry. In William F. van Altena, editor, *Astronomy and Astrophysiscs, Methods, Models, and Applications*, chapter 11, pages 154–172. Cambridge University Press, 2016. (Cited on page 47.)

[65] John David Jackson. *Classical Electrodynamics*. John Wiley & Sons, Inc., New Jersey, USA, 3 edition, 1991. (Cited on pages 48 and 117.)

[66] U. Iriso L. Torino. Limitations and Solutions of Beam Size Measurements via Interferometry at ALBA. *Conf. Proc.*, TUPB049:428–432, 2015. (Cited on pages 52 and 95.)

[67] L. Torino and U. Iriso. Limitation and Solution for Beam Size Measurements via Interferometry at ALBA. *Conf.Proc.*, pages 925–928, 2013. (Cited on page 55.)

[68] D. Malacara. *Optical Shop Testing*. Wiley-Interscience, 2 edition, 1992. (Cited on page 55.)

[69] Economy Front Surface Mirrors. *Throlabs*. `https://www.thorlabs.de/newgrouppage9.cfm?objectgroup_id=890`. (Cited on page 57.)

[70] Broadband Dielectric Mirrors. *Throlabs*. https://www.thorlabs.de/newgrouppage9.cfm?objectgroup_id=139. (Cited on page 57.)

[71] CF63 Bonded Fused Silica Viewport,. *Torr Scientific*. http://torrscientific.co.uk/wp-content/uploads/2015/04/TSL-Catalogue-2015-Copyright.pdf. (Cited on page 57.)

[72] Thales-SESO. https://www.thalesgroup.com/en/japan/thales-seso-seso. (Cited on page 57.)

[73] J. Nicolas, J.C. Martinez, C Colldelram, J Vidal, and J. Campos. The opticas laboratory at alba. ACTOP08, 2014. (Cited on page 57.)

[74] ADE PhaseShift Minifiz 100 . *KLA-Tencor*. (Cited on page 57.)

[75] L. Torino, U. Iriso, and T. Mitsuhashi. Beam Size Measurements Using Synchrotron Radiation Interferometry at ALBA. *Conf. Proc.*, TUPF23:374–379, 2014. (Cited on page 57.)

[76] M. Arinaga et al. KEKB beam instrumentation systems. *Nucl. Instrum. Meth.*, A499:100–137, 2003. doi: 10.1016/S0168-9002(02)01783-7. (Cited on page 59.)

[77] Piezoelectric accelerometer, TEDS. *Brüel and Kjael, TYPE 8344*. https://www.bksv.com/en/products/transducers/vibration/Vibration-transducers/accelerometers/8344. (Cited on page 64.)

[78] J. Ladrera and M. Llonch. Private Communications. (Cited on page 65.)

[79] Position Sensing Detectors. *Thorlabs*. https://www.thorlabs.de/thorproduct.cfm?partnumber=PDP90A. (Cited on page 65.)

[80] SRW, github. https://github.com/ochubar/SRW. (Cited on page 68.)

[81] L. Torino and U. Iriso. Transverse beam profile reconstruction using synchrotron radiation interferometry. *Phys. Rev. Accel. Beams*, 19(12):122801, 2016. doi: 10.1103/PhysRevAccelBeams.19.122801. (Cited on page 84.)

[82] U. Iriso L. Torino. Beam Shape Reconstruction Using Synchrotron Radiation Interferometry. *Conf. Proc.*, WEBL03, 2016. (Cited on page 84.)

[83] T. Mitsuhashi. Recent Trends in Beam Size Measurements using the Spatial Coherence of Visible Synchrotron Radiation. *Conf. Proc.*, THYC2:3662–3667, 2015. (Cited on page 90.)

[84] F. Ewald. Challenges for emittance diagnostics for the ESRF low emittance lattice. DEELS15, 2015. (Cited on page 90.)

[85] Sirius Light Source. http://lnls.cnpem.br/sirius-new-brazilian-synchrotron-light-source/. (Cited on page 90.)

[86] A. Labeyrie. Attainment of diffraction limited resolution in large telescopes by fourier analysing speckle patterns in star images. *Astronomy and Astrophysiscs*, 6: 85, may 1970. (Cited on page 95.)

[87] K. T. Knox and B. J. Thompson. Recovery of images from atmospherically degraded short-exposure photographs. *The Astrophysical Journal*, 193:L45–L48, oct 1974. doi: 10.1086/181627. (Cited on page 95.)

[88] A. Chao. *Physics of Collective Beam Instabilities in High Energy Accelerators*. 1993. (Cited on page 100.)

[89] J. C. Bergstrom. Jack's Book (On Beam Instabilities and Other Things). 2006. (Cited on page 100.)

[90] S. Khan. Simulation of Transverse Coupled Bunch Instabilities. *Conf. Proc.*, WAB03, 1996. (Cited on page 100.)

[91] R. Nagaoka. Fast beam-ion Instabilities observation at Soleil. *Conf. Proc.*, 2010. (Cited on pages 100 and 106.)

[92] Intensified CCD Cameras . *Andor*, . `http://www.andor.com/learning-academy/intensified-ccd-cameras-the-technology-behind-iccds`. (Cited on page 100.)

[93] High-Speed Gated Image Intensifier Units C9016-2x, C9546, C9547 Series. *Hamamatsu*. `http://www.hamamatsu.com/resources/pdf/etd/C9016-2x_C9546_TAPP1052E.pdf`. (Cited on page 101.)

[94] iStar 334T Series. *Andor*, . `http://www.andor.com/pdfs/specifications/Andor_iStar_334_Specifications.pdf`. (Cited on page 101.)

[95] U. Iriso, T. Guenzel, and L. Torino. Bunch by Bunch Instabilities at ALBA. *Conf. Proc.*, 2017. (Cited on page 106.)

[96] E. Jensen. RF Cavity Design. In *CAS - CERN Accelerator School: Advanced Accelerator Physics Course: Trondheim, Norway, August 18-29, 2013*, pages 405–429, 2014. `https://inspirehep.net/record/1416212/files/arXiv:1601.05230.pdf`. (Cited on page 114.)

[97] Harms Barletta, Spentzorius. USPS Notes. In *USPAS - United States Particle Accelerators School*. `http://uspas.fnal.gov/materials/10MIT/Emittance.pdf`. (Cited on page 115.)

[98] A. Hofmann. Characteristic of Synchrotron Radiation. *Proceedings of the CERN accelerator school*, pages 24–36, 1990. (Cited on page 117.)

[99] Z. L. Wang, Y. Liu, and Z. . Zhang. *Handbook of Nanophase and Nanostructured Materials*. Kluwer Academic PublishersPlenum Publishers, 2003, 2002. (Cited on page 125.)